Multidisciplinary Optimization Approach for Design and Operation of Constrained and Complex-shaped Space Systems

by

Dae Young Lee

A dissertation submitted in partial fulfillment
of the requirements for the degree of
Doctor of Philosophy
(Aerospace Engineering)
in The University of Michigan
2016

Doctoral Committee:

Associate Professor James W. Cutler, Chair
Associate Professor Amy M. Cohn
Professor Ilya V. Kolmanovsky
Professor Joaquim R. R. A. Martins

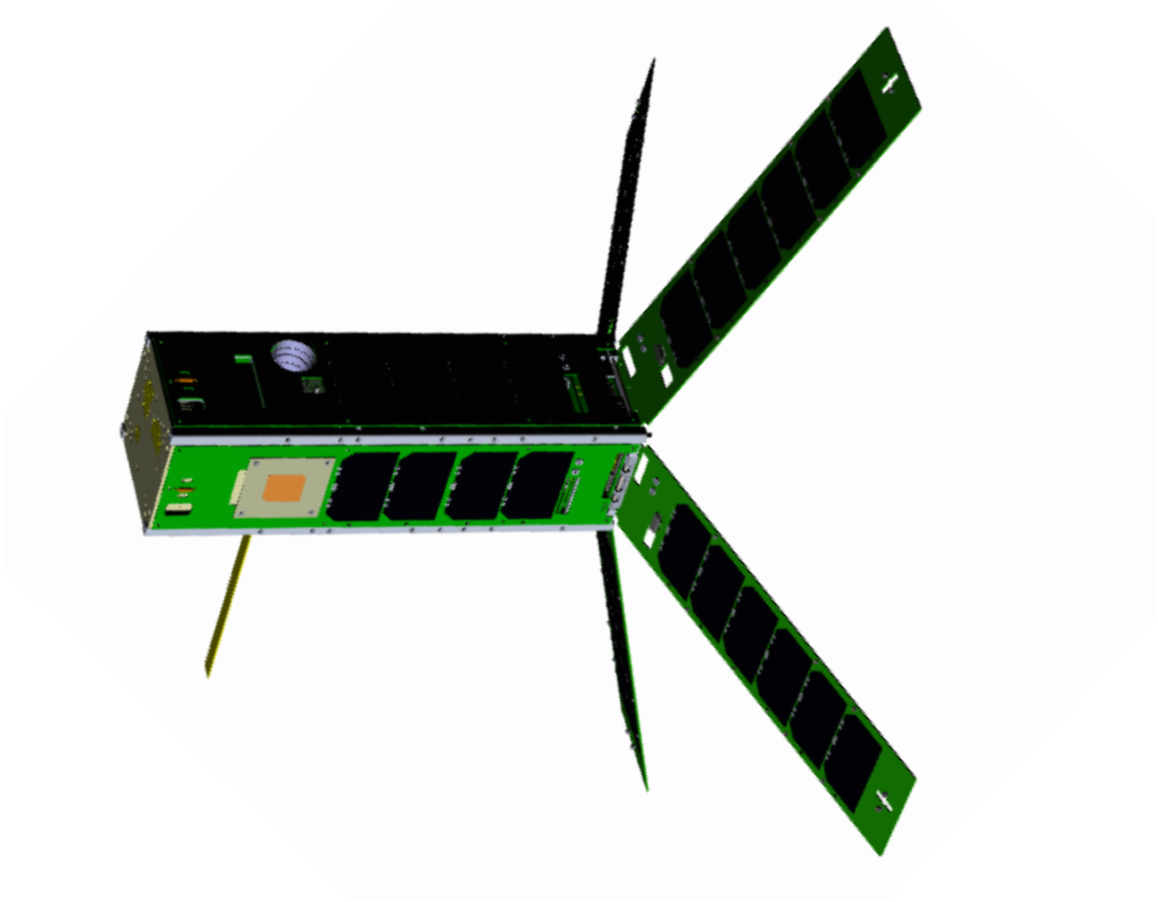

“CADRE” :

The **C**ubeSat investigating **A**tmospheric **D**ensity **R**esponse to **E**xtreme driving

"Give thanks to the LORD, for he is good. His love endures forever.

Give thanks to the God of gods. His love endures forever.

Give thanks to the Lord of lords: His love endures forever.

to him who alone does great wonders, His love endures forever."

(Psalm 136:1-4)

To my God, the Almighty,

and

To my mother.

ACKNOWLEDGEMENTS

I praise God, the almighty, good, and merciful, for allowing me to finish my dissertation. This dissertation can be completed with the help of God and his wonderful people whom I would like to appreciate here.

First, I would like to give my sincere thanks to my adviser, Professor Cutler, for his guidance, mentoring, and inspiration throughout my doctoral study. I also appreciate my committee members, Professor Kolmanovsky, Professor Martins, and Professor Cohn, for their invaluable time, feedback, and encouragement. I would like to thank Professor Jae Won Choi of Pusan National University for encouraging me to continue my graduate studies to the doctorate level.

This dissertation was motivated by and demonstrated through the design and development of small satellite 'CADRE', which has collaborated with many peoples. In particular, I want to appreciate Professor Ridley, for his support and ideas of this satellite. Thanks also to Dr. John T. Hwang, Dr. Rohit Gupta, and Dr. Hyeongjun Park for their contributions to the content of each chapter, which is based on the co-authored papers. I would like to appreciate all my friends and colleagues of Michigan eXploration Laboratory members (Prince, Tyler, So-hee, Kaitlyn, Charlie, Josh, Ari, Bobby, Valerie, Srinagesh, and others) for their support, generosity, and friendship. I am honored to have the opportunity to work in MXL with them and this dissertation would not have been possible without the help of the team. I appreciate Professor Atkins, Professor Girard, and Professor Bernstein for sharing their great knowledge on control theory.

And of course, thanks to my Korean friends for their prayer and love. Finally, I would like to appreciate my mother, Soonja Kwon, and my sister, Seonyoung's family, for their love and faith in me. Their contribution to this dissertation cannot be compared with any others, so this dissertation is gratefully dedicated to them.

TABLE OF CONTENTS

LIST OF FIGURES

Figure

LIST OF TABLES

Table

LIST OF APPENDICES

Appendix

LIST OF ABBREVIATIONS

ADCS Attitude Determination and Control System

ATSV Advanced Trade Space Visualizer

CADRE CubeSat investigating Atmospheric Density Response to Extreme driving

CMG Control Moment Gyroscope

CO Collaborative Optimization

DSS Distributed Satellite Systems

EPS Electric Power System

FEA Finite Element Analysis

FPGA Field-Programmable Gate Array

GA Genetic Algorithm

GEO Generalized Extremal Optimization

GS Ground Station

ISS International Space Station

KS Kreisselmeier-Steinhauser

LEO Low Earth Orbit

LGVI Lie Group Variational Integrator

LOS Line Of Sight

LVLH Local Vertical / Local Horizontal

MAUD Modular Analysis and Unified Derivatives

MDO Multidisciplinary Design Optimization

MIDAS Multidisciplinary Integrated Design Assistant for Spacecraft

MOI Moment Of Inertia

MPC Model Predictive Control

MXL Michigan eXploration Laboratory

NMPC Nonlinear Model Predictive Control

OASIS Optimization ASsIStant

OpenGL Open Graphics Library

PSO Particle Swarm Optimization

QPCA Quasi-Principal Component Analysis

RAAN Right Ascension of the Ascending Node

RAX-2 Radio Aurora eXplorer 2

RWA Reaction Wheel Assembly

SCOUT Spacecraft Concept Optimization and Utility Tool

SDO Single Discipline Optimization

SOC State Of Charge

SPIDR Spacecraft Portal for Integrated Design in Real-time project

SQP Sequential Quadratic Programming

TPF Terrestrial Planet Finder

WINCS Wind Ion Neutral Composition Suite

XDSM eXtended Design Structure Matrix

ABSTRACT

Multidisciplinary Optimization Approach for Design and Operation of Constrained and Complex-shaped Space Systems

by

Dae Young Lee

Chair: James W. Cutler

With the increasing trend of the space community to develop their own space systems, there is a growing interest in small satellite technology. The design of a small satellite is often challenging since they are constrained by mass, volume, and power. To mitigate the effects of these constraints, designers often adopt deployable configurations on the spacecraft that result in an interesting and difficult optimization problem. The resulting optimization problem is challenging due to the computational complexity caused by the large number of design variables and the model complexity created by the deployables. Adding to these complexities, there is a lack of integration of the design optimization systems into operational optimization, and the utility maximization of spacecraft in orbit.

The methodology developed in this research enables satellite Multidisciplinary Design Optimization (MDO) that is extendable to on-orbit operation. Optimization of on-orbit operations is possible with MDO since the model predictive controller developed in this dissertation guarantees the achievement of the on-ground

design behavior in orbit. To enable the design optimization of highly constrained and complex-shaped space systems, the spherical coordinate analysis technique, called the "Attitude Sphere", is extended and merged with an additional engineering tools such as Open Graphics Library (OpenGL). OpenGL's graphic acceleration facilitates the accurate estimation of the shadow-degraded photovoltaic cell area. This technique is applied to the design optimization of the satellite Electric Power System (EPS) and the design result shows that the amount of photovoltaic power generation can be increased more than 9%. Based on this initial methodology, the goal of this effort is extended from Single Discipline Optimization (SDO) to Multidisciplinary Optimization (MDO), which includes the design and also operation of the EPS, Attitude Determination and Control System (ADCS), and communication system. Since this MDO problem involves over ten thousand design variables and one million state variables, the Modular Analysis and Unified Derivatives (MAUD) framework is used to automatically compute the derivatives required for gradient-based optimization.

The geometry optimization satisfies the conditions of the ground development phase; however, the operation optimization may not be as successful as expected in orbit due to disturbances. To address this issue, for the ADCS operations, controllers based on Model Predictive Control (MPC) that are effective for constraint handling were developed and implemented. For the ADCS MPC controller, variational mechanics based on the 3D rotation group, denoted as SO(3), were developed. All the suggested design and operation methodologies are applied to a mission, the CubeSat investigating Atmospheric Density Response to Extreme driving (CADRE), which is space weather mission scheduled for operation in 2016. This application demonstrates the usefulness and capability of the methodology to enhance CADRE's capabilities, and its ability to be applied to a variety of missions.

CHAPTER I

Introduction

1.1 Motivation

There is a growing trend among many scientists, engineers, and entrepreneurs from the space community to develop their own space systems based on small satellite technology. Between 2000 and 2013, the number of small satellite projects increased, and the data in Fig. 1.1 presents this trend clearly. While in 2000, there were only 5 projects but, in 2006, this increased to 20 projects and drastically multiplied to 80 in 2013 [1].

This increase in missions is also accompanied by an increase in the variety of mis-

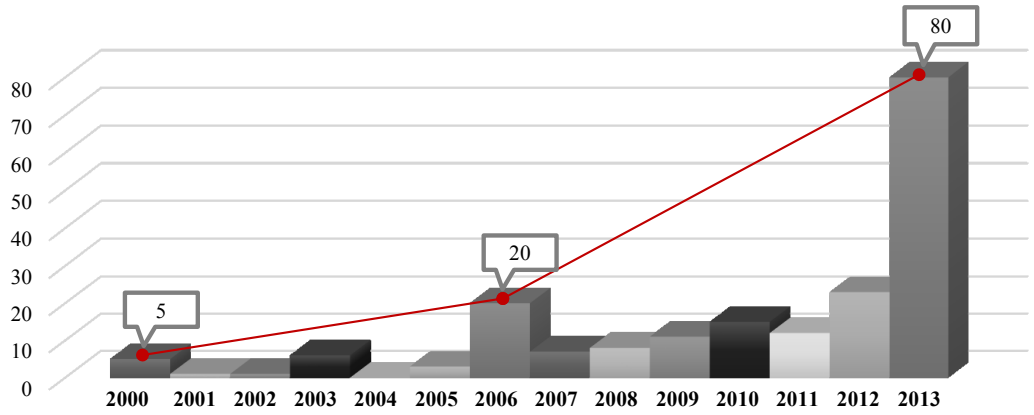

Figure 1.1: CubeSat-class missions launched in each year [1].

sions such as a scientific experiment, a demonstration for advanced technology, and a precursor mission for a future space project. This variety has led to a growing demand for enhanced performance in the areas of pointing accuracy, power generation, and data downloading. Take as an example, the need for increased pointing accuracy; we can compare the pointing requirements between projects in 2010 and 2015 that were completed at the University of Michigan. In 2010, the first NSF-funded satellite, Radio Aurora eXplorer 2 (RAX-2), needed only magnetic north pointing within the Northern Hemisphere, which can easily be satisfied with the installation of a permanent magnet and hysteresis strips for the dissipation of the satellite's angular momentum. However, because of its payload, the recently built CubeSat investigating Atmospheric Density Response to Extreme driving (CADRE) requires 1 degree pointing accuracy with its orbital velocity vector, which can only be achieved with an active Attitude Determination and Control System (ADCS) that was implmented with three axis reaction wheels and magnetorquers.

Another good example of the demand for enhanced performance of recent missions is the extended photovoltaic power generation requirement. We can understand this demand by comparing the same satellite projects. RAX-2 only needed approximately 5W of photovoltaic power, while CADRE requires almost 10W of photovoltaic power. CADRE's large power generation requirement is satisfied by implementing a configuration with 4 deployable panels as presented in Fig. 1.2(b). This example demonstrates that a primary effort of space system engineers involves finding ways to increase the amount of photovoltaic power generation in space and, as a singular method, they implemented a deployable panel configuration such as the International Space Station (ISS), NASA's solar sail project Nanosail-D (Fig. 1.2(c)), and Delfi-N3xt (Fig. 1.2(d)).

The trend indicates that many recent spacecraft projects are adopting deployable

[1]Nanosail-D : `http://phys.org/news/2011-01-first-ever-solar-momentous.html`, Delfi-N3xt : `http://space.skyrocket.de/doc_sdat/delfi-next.htm`

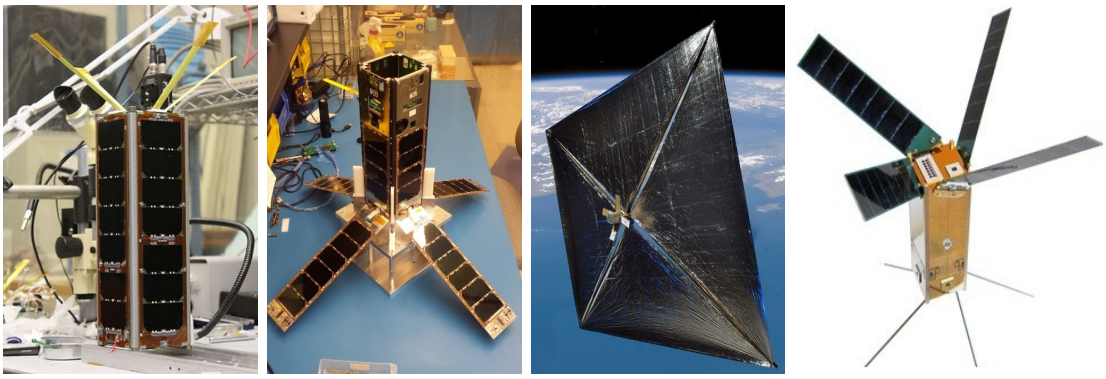

(a) RAX2 (b) CADRE (c) Nanosail-D (d) Delfi-N3xt

Figure 1.2: Various designs of small satellites[1]

panel configurations but, despite their effectiveness, they introduce complexity and constraints into the system. For example, if we want to increase the power generation by installing more deployable photovoltaic panels, we need to analyze the shadow of each panel, which can hinder the power generation of other panels. Without this analysis, we cannot guarantee sufficient power generation with the installed photovoltaic panels [6]. The deployable panels can also cause unexpected dynamics disturbances and degradation of pointing accuracy. Given these challenges of deployable space system design, the design small satellites with this technology is more difficult and poses interesting problems compared to the normal spacecraft design. To resolve these challenges, the following question is addressed in this dissertation:

How can we maximize the capability and performance of a complex-shaped space system with constraints?

This dissertation uses a multidisciplinary approach to answer this question.

1.2 Literature review

As mentioned in the motivation section, in addition to satisfying requirements in performance, space systems certainly benefit from maximizing their resource utility

efficiency and performance. In this section, we review the literature that describes how optimization technology has been applied to the space system design process. The related research can be categorized into two groups. The first group approaches the space system design optimization problem from the perspective of a single discipline, while the second group employs multidisciplinary approaches. The most interesting approaches can be found in the latter, where operation optimization of the space system has been unified with the design optimization process. Based on this initial work, this dissertation focuses on multidisciplinary optimization and the on-orbit controller development. After reviewing two main research groups, the unification of the design and the operation optimization in the space system is investigated.

1.2.1 Single Discipline Optimization

Single Discipline Optimization (SDO) is the analysis and optimization of an engineering system with focus on a single part of the system or in a single discipline [7]. One typical characteristic of SDO is the usage of gradient-free optimization with indifferentiable design variables that originate from detailed modeling. The detailed and complex modeling often includes discrete or indifferentiable variables that cannot be handled with gradient-based optimization. These variables can only be handled with gradient-free optimization such as Genetic Algorithm (GA) or Particle Swarm Optimization (PSO). Hence, many single discipline optimization researches focus on gradient-free optimization.

Another characteristic is that most SDO applications have a small number of design variables because the gradient-free optimizer cannot handle a large number of design variables. Even with the gradient-based optimization, the number of design variables is less than 100 due to the limited characteristic posed by 'single' discipline. The following are representative SDO examples.

Boudjemai et al. [8] designed small satellite structural topologies with minimum

compliance, minimum weight, and optimal compliant mechanisms. They performed geometry modeling with Finite Element Analysis (FEA) and adopted different types of mesh under launch loads environment to determine the maximum stresses acting on the elements of the structure. Then, they solved this optimization problem with an enhanced GA to acquire more efficiency and robustness.

Muraoka et al. [9], in order to minimize heater power consumption and maximize temperature margins, suggested an optimization strategy applicable to the configuration of radiator and solar absorbers in a spacecraft thermal design. As a solver, they implemented a Generalized Extremal Optimization (GEO) algorithm, which has also been applied to the inverse design of a spacecraft thermal control system suggested by Galski et al. [10]. This GEO has only one free parameter to adjust, does not make use of derivatives, and can combine continuous, discrete or integer variables.

Hull et al. [11] defined the spacecraft radiator design problem and solved it with GA. They defined a driving temperature as an input and heat loss as an output and added the appropriate modeling of the space environment to capture its effect on the radiator. After them, in [12], an efficient multi-objective optimization method is proposed by Kim et al. for node-based spacecraft radiator design. The optimization problem is formulated to minimize the number of radiator nodes and temperature margins of unit boxes and is solved with a GA.

Jain et al. [13] optimized the power management of a small satellite which is popular due to the restricted photovoltaic power generation amount of every small spacecraft. Their optimizer used GA but can evaluate the fitness on Field-Programmable Gate Array (FPGA) in real time. Thus, the limited power supply capability of a small satellite was overcome, and its load scheduling was successfully optimized.

Khoddam et al. [14] developed AUTO LISP code for CAD which calculate the optimized layout of different modules. Their small satellite used a gravity gradient passive stabilization system. To dampen transient oscillations, the Moment Of In-

ertia (MOI) calculation was important and their AUTO LISP code automatically calculated MOI and checked the stability.

Richie et al. [15] optimized the size of a miniature control moment gyroscope for a practical space mission. By analyzing attitude and energy storage requirements of a small satellite, their design problem can be converted to a constrained nonlinear programming problem which uses a performance index constructed from subsystem design margins. They solved the problem using a reduced-order, gradient-based solver software code, and it is a rare example of the gradient-based optimizer implementation in SDO problems because most of this SDO application include indifferentiable design variable which is not easy to solve with a gradient-based optimizer.

Zhang et al. [16] optimized the layout of the satellite subsystems with the integrated GA/PSO and Quasi-Principal Component Analysis (QPCA).

The review result confirms that most of SDO literature have implemented GA and other non-gradient based optimization methods, which have small numbers of the design variables. This also indicates that, if we want to include a large number of the design variables in design optimization problem, a novel approach is necessary. However, SDO is still a very effective tool to satellite engineers who focus on the subsystem design with restricted requirements.

1.2.2 Multidisciplinary Optimization

MDO is a rapidly growing field with applications to a variety of aerospace problems. Many aerospace system designers have applied multidisciplinary approaches to their system design projects [17]. However, most MDO efforts have focused on the design of aircraft structures and space launch vehicles, and very little work has considered the MDO application to the space system with complex constraints, such as a small satellite. For the remainder of this section, we cover the application of MDO within the field of space systems design and also check applicability to a highly

constrained system with a complex-shape problem.

The first identified MDO application to space systems was a launch vehicle design done by Olds et al. [18]. Others have applied MDO to launch vehiclea as well [19, 20, 21, 22, 23, 24, 25] where the applicatoin of MDO was extended to space system engineering. Satellite design with MDO was first applied by Matossian to the design of an Earth-observing satellite mission [26]. Spacecraft design-related research was continued by Mosher [27], Riddle [28], and Bearden [29], who focused on the development of space system engineering tools. The first reason why they focused on the system engineering tool development is that the increased complexity of the design problem necessitates an organized and structured solving procedure and the other reason is the engineering tool makes the evaluation of the optimization results easy by including various models and their simulation environments. The developed space system engineering tools for MDO applications are as follows.

George et al. [30] developed the Multidisciplinary Integrated Design Assistant for Spacecraft (MIDAS), which is a graphical programming language specifically for space mission design which allows the satellite engineer graphically to connect the data flow of the system. Disciplines and software modules can be added or removed to support the multidisciplinary design capability. After a system is constructed within MIDAS, operator can evaluate the system's cost and mass and, if the evaluation result is unsatisfactory, the designer can alter the spacecraft modules and evaluate again.

Fukunaga et al.[31] built the Optimization ASsIStant (OASIS), a system tool that can provide the optimized spacecraft with minimal human effort. They also proposed the use of a set of generic, metaheuristic optimization algorithms (e.g., genetic algorithms, simulated annealing), which are configured for a particular optimization problem by an adaptive problem solver based on artificial intelligence and machine learning techniques. These algorithms are interfaced to MIDAS such that they drive desgin variable selection rather than a human-in-the-loop directing the simulator.

OASIS provides the design variable values with which MIDAS then calculates system performance. Several satellites are successfully designed with OASIS by using a brute-force search method over the design space.

Mosher et al. [32, 33] suggested a tool for conceptual spacecraft design, Spacecraft Concept Optimization and Utility Tool (SCOUT), that uses a set of design-estimating and cost-estimating relationships that are coupled with genetic algorithm optimization. Exploring a greater number of feasible options is possible using SCOUT's automated search which also allows the selection of counterintuitive solutions. The solution from SCOUT is compared and verified with the actual design of the Near Earth Asteroid Rendezvous spacecraft.

In [34], Stump et al. developed the Advanced Trade Space Visualizer (ATSV) that facilitates design by using a shopping paradigm to support trade space exploration. ATSV allows a decision-maker to form a preference and use this preference to select a satellite. The test data of ATSV generated using a conceptual model of a Mars space probe, with rules based on Mars Odyssey mission and the final design was presented with 3D modeling.

Ravanbakhsh et al. [35, 36] introduced a structural design-sizing tool containing the primary structures properties and system level variables. The search of the design space is performed with a GA multiobjective optimizer and the Pareto-optimal results could be acquired based on minimum total mass of satellite and maximum mass budget for the payload.

Barnhart et al. [37] implemented a Spacecraft Portal for Integrated Design in Real-time project (SPIDR), a systems-engineering-based framework for satellite design with an artificial-intelligence-based optimization algorithm that incorporates user-defined rules and constraints. SPIDR brings together astronautics experience of building and launching satellites on various missions with techniques from artificial intelligence and software engineering to enable rapid design-to-integration of

space vehicles. SPIDR is intended to broaden the design process, which includes levels of integration, and incorporate a real-world database.

Apart from the above system engineering tool developments, the following researchers have devoted themselves to the development of a novel MDO methodology itself for space systems. For example, in [38], Taylor et al. provided an evaluation of optimization techniques which are applied to increasingly complex spacecraft design problems. They found that traditional optimizers such as dynamic programming can guarantee an optimum, but require enumeration with exponential growth of the variables. So, they had found a commercial optimizer that was insensitive to additional variables and provided high-quality solutions.

Jilla et al. [39] developed the constructing process of multiobjective, multidisciplinary design optimization systems. In this methodology, they formulated and solved distributed satellite system conceptual design problems and applied two new multi-objective variants of the simulated annealing algorithm. It was applied to the Distributed Satellite Systems (DSS) problem and found the architecture for NASA's Terrestrial Planet Finder (TPF) mission that maximizes the total number of images taken by the telescope while minimizing life-cycle cost.

Jafarsalehi et al. [40] focused on the development of an efficient distributed Collaborative Optimization (CO) method for small satellite missions. GA were used at the system level while gradient-based techniques were utilized at the discipline level. The results showed that a distributed CO framework using GA has the same level of accuracy as with the conventional all-at-once approaches, while providing a potential approach for solving complex satellite design problems.

From these MDO literature review, we can see that many researchers started with the development of a system engineering tool that considers multiple disciplines. After the development, they tried to apply the mathematical optimization technique to improve the spacecraft design because they agree on MDO as a potentially powerful

tool for spacecraft design. In addition, we can see that the recent MDO researches are definitely considering small satellite as their application [37, 39, 40].

By adopting MDO, space system design becomes more realistic but more complex with various disciplines. In addition, these review confirm that the operation in orbit is difficult to be considered at the ground development stage. The research number related with a large-scale optimization problem also suggest that this problem is a difficult topic to solve because of computational price.

1.2.3 Operation including Optimization

In reviewing the literature on the space system optimization and especially MDO materials, the approach suggested by Spangelo et al. [41, 42] is particularly interesting. They developed models and algorithms for solving single-satellite, multi-ground station communication scheduling problems, with the objective of maximizing the total amount of data downloaded from space. They assumed a highly constrained space system with limited on-board power generation, attitude and orbit control, energy and data storage, and computational resources. To model the optimization problem, an under-constrained mixed integer program (MIP) is implemented and the constraints of the problem are tightened by an iterative algorithm. The most interesting aspect of their research is that they included the ground station operation over time in the optimization problem, making it more challenging.

Motivated by their idea, in this dissertation, the design and the operation of the satellite is unified in our MDO problem. However, unlike Spangelo's work, the suggested MDO methodology separate the multiple Ground Station (GS) operation from the problem. Instead of the GS operation, the proposed MDO includes the satellite subsystem operations that require the development of operation controllers.

1.3 Approach

Based on the literature review, a multidisciplinary optimization based approach is proposed to explore the question of how to maximize the performance of a constrained and complex-shaped space system. This approach extends the traditional system design by merging geometric design with operation of the spacecraft. As a first step, the space system design with SDO was performed and a result on photovoltaic panel design is obtained. By adopting data and models from the SDO, design optimization and operation optimization can be performed in the MDO. Working jointly with the MDO Laboratory at the University of Michigan, the solution of this MDO problem was developed. The MDO solution then shows that operation optimization in orbit can improve satellite performance drastically. As a result, a constrained control solution is developed to apply the operation optimization results in orbit. Many challenges such as complex shadows of deployables, multiple discipline development, a large number of design variables, computational complexity and on-orbit implementation are resolved by the approach proposed by this dissertation.

1.3.1 Single Discipline Optimization

SDO is performed to build and verify a discipline for photovoltaic power generation. This SDO application itself is helpful for the design of various satellite missions and the developed discipline is also implemented in the following MDO approach. The objective functions of the SDO are related to the amount of photovoltaic power generation, which is essential to the mission capability estimation. This problem is difficult due to the complex shadow casting of the deployable panels and the solution is described with detail in Chapter II.

The main concept of the solution is to map the Sun's movement on a body-fixed frame of the spacecraft, called the attitude sphere, and to search for the shadow database with this spherical coordinate mapping. This attitude sphere, the spacecraft

body-centered spherical coordinate system, is merged with orbit dynamics to map the Sun movement. After that, a spherical shadow database is built with the help of OpenGL, which rapidly calculates the exposure of photovoltaic cells to each position of the Sun. The deployable panel angle is also included as a index of the shadow database and can be determined through search of the Sun mapping database.

1.3.2 Multidisciplinary Optimization

Preliminary tasks such as complex shadow and antenna radiation pattern modeling can be completed by an individual SDO effort. SDO analysis also provides insight for whih variables are more effective as design variables for the optimization. This serves as a foundation for combining related disciplines into a larger, mutlidisciplinary optimization problem. Due to the multidisciplinary characteristic, this optimization includes a tremendous number of design variables resulting in great computation complexity. For example, with the ADCS and Electric Power System (EPS) design, there are more than 20,000 design variables. In collaboration with the MDO Laboratory at the University of Michigan, we found that this problem can be solved with a Modular Analysis and Unified Derivatives (MAUD) method which is based on gradient-based optimization. This work highlighted the additional capabilities of optimization when applied to the operation of the satellite as well. However, additional control capabilities are needed for this to be implemented on-orbit.

1.3.3 Operation optimization

There are two possible methods for application of these optimization to on-orbit operations. One method is to uploaded optimization results from ground-based processing to the satellite in orbit. This requires periodic execution on the ground with open-loop control; the algorithm cannot be adapted in real time to on-orbit disturbances or anomalies. The second metho is to automate operation with a controller

that can satisfy the ground optimization results. In this dissertation, the automated operation with constrained control algorithm is proposed.

Constrained-based control is developed for the attitude determination and control system. Prior MDO results showed that drastic increase of the downloaded data is possible for spacecraft by applying an optimized attitude profile in orbit. To achieve the design goals, a constrained-based controller is required. For example, when the GS is visible to a spacecraft, the spacecraft can be rotated towards the GS to enhance the communication link. Similar logic can be applied to the spacecraft's relative motion to the Sun to maximize power generation. However, if the ground station appears in the Line Of Sight (LOS) of the spacecraft or if the star tracker camera is exposed to the Sun, different attitude operations are required. To satisfy the above constraints with detailed operations, we have developed and implemented a nonlinear model predictive attitude controller, which is capable of various constraints. For this ADCS controller, variational mechanics based on the 3D rotation group, denoted as SO(3), were applied.

Initial MDO results also suggest that power regulator operation is required to maximize the efficiency of the spacecraft EPS. This spacecraft EPS is typically constructed with a combination of photovoltaic arrays and batteries, and Xiong et al. [43] suggest a combination of the buck and bi-direction converter. The EPS they suggest demonstrates good power generating and battery charging performance in the ground application that can be extended by the application of the novel Model Predictive Control (MPC) algorithm to attain peak power tracking for photovoltaic arrays and protection from overcharging the battery at the same time[44]. However, this research is quite a large topic and is left for future research.

1.4 Research Contributions

The main contributions of this dissertation are the development of a systemic multidisciplinary approach for the design and operation optimization of space systems and the specific application of this approach to a novel space mission called CADRE. To achieve the main goal, in each chapter we established the sub-problem, which is essential for the main solution, and the following research contributions are made in each problem.

- To maximize photovoltaic power generation of a complex-shaped spacecraft,
  - A rapid and accurate calculator is developed for determining the self-shadowing area of a complex-shaped spacecraft that is based on OpenGL.
  - A simulator is developed based on this shadow calculator to evaluate various power-related objective functions, which is more precise than other simulators in handling complex shadowing.
  - The process to configure photovoltaic panels of complex-shaped space systems are established, which is applicable to systems such as ISS or a CubeSat with deployable panels.
- To apply MDO to design and operation of a small satellite,
  - A gradient-based multidisciplinary optimization approach is developed.
  - Disciplines including orbit dynamics, attitude dynamics, photovoltaic power, battery, thermal, and communication are modified for the optimization framework.
  - The satellite MDO problem with a large number of design variables is formulated and solved for the CADRE mission.
- To develop a attitude operation controller for a spacecraft with Reaction Wheel Assembly (RWA),

- A Nonlinear Model Predictive Control (NMPC) approach to the constrained attitude control of spacecraft is developed.
- A discrete-time Lie Group Variational Integrator (LGVI) model of spacecraft with the reaction wheel assembly is implemented in the underlying Lie group structure of SO(3) which has consistency in geometric mechanics and control formalism.
- The numerical solution to the NMPC optimization problem was obtained using necessary conditions for optimality and a single shooting method to solve the resulting two point boundary value problem.

By resolving each problem, the multidisciplinary approach for the design and the operation of a complex-shaped space system is completed and applied to CADRE, a satellite funded by the National Science Foundation (NSF) to study space weather.

1.5 Dissertation Outline

The remainder of the dissertation is outlined as follows. Chapter II introduces a photovoltaic power generation discipline and a developed simulation system that uses a spacecraft-body-fixed spherical coordinate system. This chapter also presents example cases with various objective functions and with the complex geometry of a satellite that causes self-induced shadowing. Chapter III implements this photovoltaic power discipline into the gradient-based multidisciplinary optimization (MDO), which also involves five other disciplines. The developed method is applied to CADRE and successful optimization is confirmed with a 40% increase in the download data amount. Motivated by optimally allocated attitude operation effects on the target performance, Chapter IV extends the results from Chapter III to the development of a novel attitude controller, of which the objective is to perform operational decisions of the MDO. Thus, a nonlinear model predictive controller is introduced for constrained attitude

maneuvering of a spacecraft actuated by a reaction wheel assembly in Chapter IV. Finally, the dissertation is summarized and insights for future work are provided in Chapter V.

CHAPTER II

Maximizing Photovoltaic Power Generation of a Space-Dart Configured Satellite

2.1 Introduction

Optimizing power generation on a satellite is an important stage in design. It is, however, difficult due to complex spacecraft geometries, varying operational modes, and orbital parameter variation. For example, complex spacecraft geometries such as deployable panels allow for more photovoltaic arrays on orbit. However, they result in complex shadow-induced power reduction that is difficult to model. Different satellite operational modes such as the downlinking of data or payload operation often require different satellite orientations, which can have a large impact on power generation. Additionally, orbital variations due to perturbation forces create a dynamic illumination cycle that exists on the order of hours to months. As an example, consider power optimization onboard the ISS where multiple photovoltaic panel arrays and complex structures produce dynamic shadows. [1]

Power generation and optimal photovoltaic panel orientations are particularly important for small satellites which have restricted size, mass, and surface area for panel mounting. The majority of small satellites are low Earth orbiting. They are

[1] Topcoder, ISS longeron optimization competition (http://www.topcoder.com/iss/longeron/)

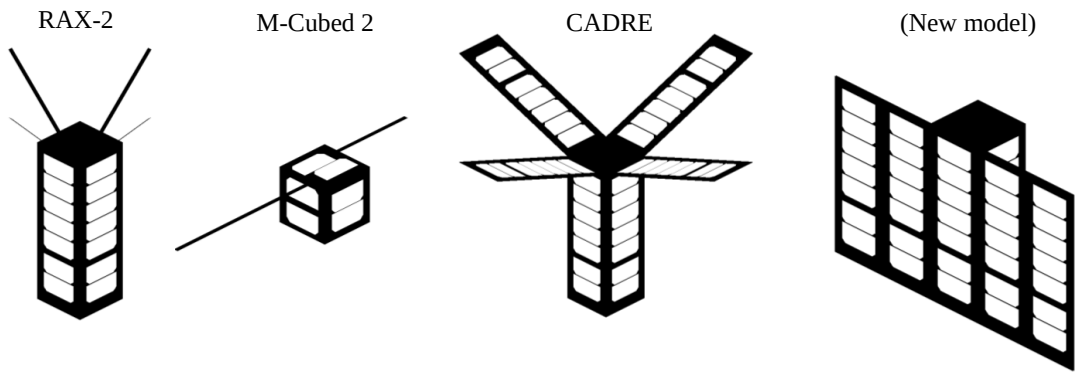

Figure 2.1: Geometry model examples of small satellites.

impacted by frequent encounters with Earth's shadow and a highly dynamic, time-varying direction from the satellite to the Sun. In particular, the growing community of CubeSat builders has operational limitations and constraints by power, and is thus developing novel photovoltaic panel configurations [45, 46, 47]. See Fig. 2.1 for example configurations. However, there are currently no techniques or algorithms for optimizing these panel configurations for particular missions and orbit scenarios.

A prominent CubeSat configuration that could benefit from the optimization of photovoltaic panel orientations is the space-dart [45, 48], a 3U with four deployable photovoltaic panels (see Fig. 2.2). The four extendable panels are typically covered with photovoltaic cells and deployed at a fixed angle throughout the mission. The attitude of this configuration is defined with respect to the Local Vertical / Local Horizontal (LVLH) frame where the $(-)z$ axis of the satellite is aligned with the velocity vector. In this space-dart configuration, self shadowing is prevalent from a variety of viewing angles. Shadow-based power reduction is, thus, a complex function of the panel angle and the direction to the Sun in the satellite body fixed frame, which is also a function of the orbit parameters and the attitude.

There is currently no known formulation or modeling framework found in the literature to solve the power generation estimation problem of the complex-shaped

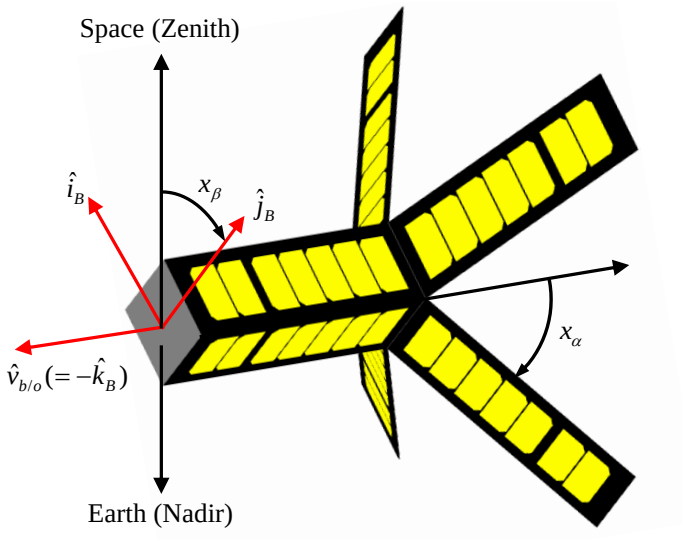

Figure 2.2: Configuration of the geometry, frame, and design variables of CADRE.

spacecraft. Some next-generation missions have additional, complex panels without a rigorous methodology for optimization [47]. Anigstein et al. [49] proposed an analytical decision method for panel angle which assumes that a satellite body does not generate a shadow impacting the panels. This assumption may be valid for larger satellites that can sufficiently deploy and separate the panels from the spacecraft body. However, this method is typically not applicable to small satellites due to mass and volume constraints. In other work, Gaddy [50] developed a computation method for the projected area of photovoltaic panels, which takes into account the spacecraft body shadow. It, however, does not include self-induced shadowing by other panels. Therefore, a key element of this work is the inclusion of shadow management for complex satellite configurations.

In this chapter, we develop an algorithm to find the optimal panel angles that maximize power generation. Specific contributions include the following:

- Development of an extendable methodology that search for the maximum power generation geometry of satellites.
- Development of a technique for assessing shadow-induced power reduction for

complex satellite geometries.

- Application and assessment of power optimization to the space-dart configuration.

In Section 2.2, the power generation of a space-dart configured satellite is defined as an optimization problem. In Section 2.3, an analytic approach and simulation architecture for solving these problems are presented. In Section 2.4, various simulation results for an example mission are given to prove the effectiveness of the described methodology. The example mission, CADRE, is a 3U CubeSat designed to explore Earth's thermosphere. CADRE has the shape similar to the space-dart configuration.[2] Optimal angles to maximize power generation of a space-dart configured satellite are also presented and discussed in Section 2.4.

2.2 Problem Definition

In this section, the notation and details of the optimization problem are introduced. The design variable $\mathbf{x}$ is a vector that contains a subset of the variables that a designer selects to control power system performance. The objective function is defined as $\mathcal{J}$. Three unique, potentially interesting objective functions are defined. The parameters $\mathbf{p}$ are additional values used in determining the objective function $\mathcal{J}$. Throughout the rest of the chapter, the space-dart configured satellite, as shown in Fig. 2.2, is used as a motivating example while describing $\mathbf{x}$, $\mathcal{J}$, and $\mathbf{p}$ in detail.

2.2.1 Design Variables

Design variables are spacecraft features that engineers select for a particular mission. There are many design variables that impact the spacecraft power generation.

[2]Note that while the space-dart configuration provides potential drag-based stabilization, CADRE contains reactions wheels and magnetorquers to provide attitude control.

Example variables include the number of photovoltaic cells, their location, photovoltaic cell type, battery size, photovoltaic panel deployment angles, and satellite orientation.

This work focuses on the optimization of power generation. Hence several simplifying assumptions are made. First, energy storage constraints are not considered. It is assumed there is sufficient battery capacity available to store any surplus energy collected. Second, while photovoltaic cell efficiency is directly proportional to power generation, it equally impacts all configurations. It is thus not considered as a design variable. Third, temperature effects on cell efficiency are ignored. Adequate thermal management is assumed so that desired average temperature is maintained. Future extensions will include advanced thermal modeling as it directly impacts cell efficiency. Fourth, the entire surface area is covered with photovoltaic cells. This maximizes power generation; however, it does not convey mission specifics such as antenna placement or requirements of other external sensors. In later sections, it is shown how cell position can be evaluated for individual power generation and which cells are primary power contributors.

With these assumptions and the space-dart configuration, two primary design variables are used as shown in Fig. 2.2. The first variable x_α is the deployment angle of the four photovoltaic panels, or specifically the angle between the deployed photovoltaic panel and the long z axis of the satellite. The second variable x_β is the roll angle of the satellite, or specifically the angle between the y axis of the satellite and the zenith. Nadir and zenith locations are shown in Fig. 2.2. The unit vectors, $\hat{i}_B$, $\hat{j}_B$ and $\hat{k}_B$, correspond to the body-fixed frame's x, y, and z axes, respectively.

The space-dart is typically flown with the $-z$ axis pointing in the ram direction, that is, the direction of the velocity vector $\vec{v}_{b/o}$ of the satellite. We assume the four deployable panels have the same deployment angle of x_α, which remains constant after launch and deployment. The design variable vector is given in Eq. (2.1) with

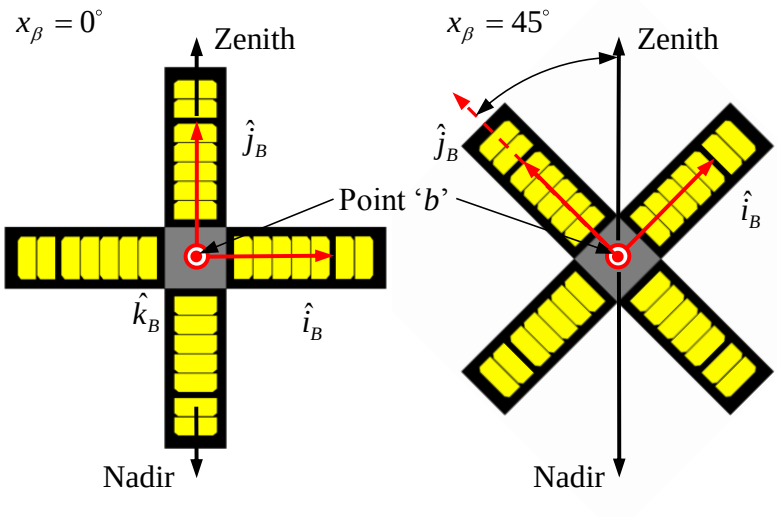

Figure 2.3: Two cases of the design variable x_β.

constrained values. The two options for x_β are presented in Fig. 2.3, where the satellite is flying in either a horizontal or a rolled configuration. Only these two configurations are considered since they easily support two simplified patch antenna placement configurations; at a 0° roll angle, a patch antenna placed on the nadir face will point nadir and provide higher gain to stations below the satellite. A 45° roll angle supports two patch antennas placed on the nadir decks which provides greater antenna coverage. [3] The design variables are summarized as

$$\mathbf{x} = \{(x_\alpha, x_\beta) \,|\, x_\alpha \in [0, 90]\,,\ x_\beta \in \{0, 45\}\}\,. \tag{2.1}$$

2.2.2 Parameters

Parameters are quantities that affect the objective function $\mathcal{J}$, but are not under adjustable in the designs. They are thus not variable in the optimization. In this

[3] Antenna placement and orientation are other interesting design variables to optimize but are beyond the scope of this chapter.

problem, the parameter vector $\mathbf{p}$ involves both spacecraft and orbit related elements,

$$\mathbf{p} = [\mathbf{p}_{SC} \ , \ \mathbf{p}_{orbit}] \, .$$

There are many parameters that govern power generation of a satellite such as the location d_{cell}, the total number N_{cell}, and the efficiency ε_{cell} of the photovoltaic cells.

$$\mathbf{p}_{SC} = [d_{cell}, \ N_{cell}, \ \varepsilon_{cell}, \ N_{reg}, \ C_{batt}, \ N_{batt}, \ \dots \ ] \, .$$

Location specific parameters are encapsulated in our assumption that CADRE is a space-dart with cells deployed on every possible surface. Additional parameters describe the conversion of photovoltaic power to stored energy and the distribution of power to the satellite. These parameters are simplified by assuming that the battery system is capable of storing all generated power and that the efficiencies of various components are independent. Hence $\mathbf{p}_{SC}$ can be combined into a single system efficiency ε_{cell}. Parameters are extracted from the orbital environment of the satellite since the orbit of the satellite strongly influences the incidence angle of the Sun on the photovoltaic panels. For example, consider two different configurations of sun-synchronous orbits such as dawn-dusk and noon-midnight orbits; the first orbit is illuminated continuously while the second sees an eclipse every orbit.

An orbit can be defined using the six classical Keplerian orbital elements: semi-major axis a, eccentricity e, Right Ascension of the Ascending Node (RAAN) (or Ω), inclination i, argument of perigee ω, and true anomaly ν. In a later section, it is shown that many of the elements, which vary over time due to orbital perturbations, do not need to be explicity parameterized as their effects average out over long simulations. The primary parameters are the right ascension of the ascending node and inclination,

$$\mathbf{p}_{orbit} = [e, \ a, \ i, \ \Omega, \ \omega, \ \upsilon] \Rightarrow [i, \ \Omega] \, .$$

In later sections, the sensitivity of the design variables to these orbital parameters is assessed.

2.2.3 Objective Functions

The goal of optimization is to maximize the objective function,

$$\max_{\mathbf{x}} \ \mathcal{J}\left(\mathbf{x},\ \mathbf{p}\right). \tag{2.2}$$

In this work, several objective functions are identified to highlight different aspects of the time-varying nature of power generation.

The first objective function is the total energy gathered during the mission, where the goal is to maximize total energy collected. Let $\mathcal{J}$ be the total energy collected by the spacecraft over a particular time interval T,

$$\mathcal{J}\left(\mathbf{x},\mathbf{p}\right) = \int_0^T P_{solar}\left(\mathbf{x},\mathbf{p},t\right)dt, \tag{2.3}$$

where $P_{solar}\left(\mathbf{x},\mathbf{p},t\right)$ is the power generation of the spacecraft at a particular instant in time t, for given values of $\mathbf{x}$ with parameters $\mathbf{p}$.

A second objective function is the minimum average power per orbit, where the goal is to maximize the minimum power generated per orbit over a given time period. This enables designers to guarantee a minimum average power generation over the time period of interest. The objective function is given in Eq. (2.4),

$$\begin{gathered}\mathcal{J}\left(\mathbf{x},\mathbf{p}\right) = \min\left[\frac{1}{T_o}\int_{(n-1)\cdot T_o}^{n\cdot T_o} P_{solar}\left(\mathbf{x},\mathbf{p},t\right)dt\right], \\ n = 1,\ 2,\cdots,n_{max} \in \mathcal{I},\end{gathered} \tag{2.4}$$

where n is the orbit number, T_o is the orbit period, and n_{max} is the total number of

orbits, respectively. As an example, a 500 km orbit simulated for one year has a T_o of 5,668 seconds and n_{max} is approximately 5,563. Designers can use this average power to baseline power budgets and operational modes.

A third objective function is the variance of average power during an orbit. Let the objective of the variance be defined as

$$\mathcal{J}(\mathbf{x}, \mathbf{p}) = \sum_{n=1}^{n_{\max}} \left(P_{batt} - \frac{1}{T_o} \int_{(n-1)\cdot T_o}^{n \cdot T_o} P_{solar}(\mathbf{x}, \mathbf{p}, t) dt \right)^2, \tag{2.5}$$

where P_{batt} is the power supplied by the battery when generated power is less than the power required by the satellite. This is useful for limiting the discharge cycles on battery systems, which extends their operational lifetime.

In the rest of this chapter, the total generated energy, Eq. (2.3), is used as the objective function, and others are saved for future work.

2.3 Methodology and Simulator

Due to the complexity and time-varying nature of photovoltaic panel illumination, a simulation system was developed that models a spacecraft and assesses power generation through a variety of user-defined parameters. The goal of this simulation system is to determine optimal design variables, x_α and x_β, given a particular objective function and set of parameters. The simulation system and methodology can be extended to include other arbitrary satellite configurations and orbits. Future work may extend the system to real-time variable selection to enable active optimization of movable photovoltaic panel orientations.

The architecture of the simulator is shown in Fig. 2.4. First, a model of the satellite is created with the space-dart configurations. Second, orbital parameters are used to calculate the spacecraft position and attitude in an inertial reference

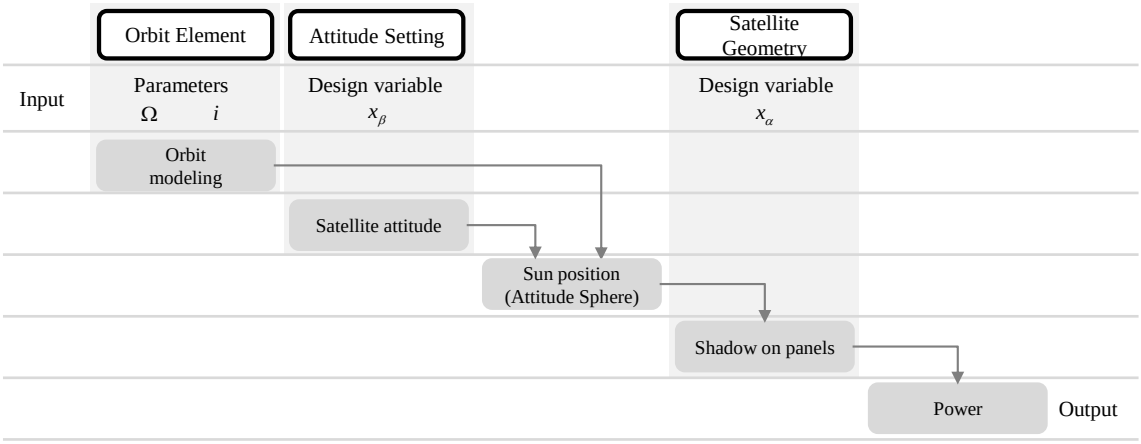

Figure 2.4: Input/output relationships between subsystems of the simulation.

frame over a particular time frame. A vector from the spacecraft to the Sun is then calculated over the time frame and converted to a local, body-fixed reference frame attached to the spacecraft and represented in spherical coordinates. In this body-fixed frame, the Sun appears to rotate around the spacecraft, which simplifies shadow and power calculations. Next, this Sun position vector is used to determine illuminated and shadowed regions of the spacecraft body, and this is represented in a satellite body-fixed spherical frame (denoted as S) called the 'attitude sphere' [51]. Finally, power and energy are calculated and an objective function is evaluated over the given time frame. Details of the simulator and methodology are given below.

2.3.1 Modeling Photovoltaic Array Configuration

First, a three dimensional model of the photovoltaic panels is created. The space-dart configuration of the photovoltaic arrays (also called strings) and their placement on panels is shown in Fig. 2.5. There are twelve strings on eight panels. Four strings are located on body-mounted panels and labeled according to the axis that is normal to the panel plane. The $+x$ and $-x$ panels are along the x axis, the $+y$ and $-y$ panels are along the y axis, and there are no photovoltaic panels on the $+z$ and $-z$

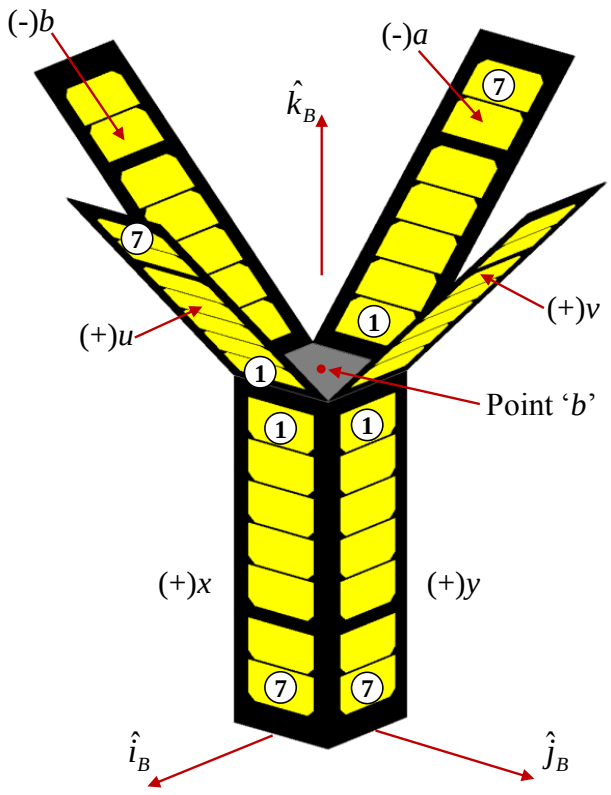

Figure 2.5: Name of each panel and identification index of cells.

panels along the z axis. The four deployable panels are labeled a, b, u, v, and each have two strings, one on each side of the panel. A negative sign indicates the array is on the inside which faces the z axis. A positive sign indicates the array is on the outside which faces away from the z axis. Each array has seven photovoltaic cells which are numbered ① to ⑦. This model enables individual cells on specific panels to be addressed and specifically modeled during illumination calculations, as will be shown later.

2.3.2 Calculation of Sun Position

Given the photovoltaic array model, the next step is to calculate the sun position vector over time and express it in the local vehicle frame. This enables calculation of array illumination and power generation over time.

Let the vector from the Earth to the Sun be denoted as $\vec{r}_{s/o}$. This vector can

be resolved in different frames, where the notation $\vec{x}|_I$ is the vector resolved in the Earth-centered inertial frame (I), and $\vec{x}|_B$ is the vector resolved in the satellite body-fixed Cartesian frame (B). Similarly, the vector from the Earth to the Sun resolved in I frame can be denoted as $\vec{r}_{s/o}\big|_I$. With the same notation, the Sun position vector resolved in the B frame is expressed with the notation $\vec{r}_{s/o}\big|_B$.

Given the orbit parameters, an orbit propagator (based on Newtonian dynamics with Earth oblateness effects) is used to calculate the satellite position vector, $\vec{r}_{b/o}\big|_I$. Eq. (2.6) below is used to calculate the position vector from the satellite to the Sun($\vec{r}_{s/b}$) in the I frame.

$$\vec{r}_{s/o}\big|_I(t) - \vec{r}_{b/o}\big|_I(t) = \vec{r}_{s/b}\big|_I(t). \tag{2.6}$$

Here, point o is the origin of I frame and is located at the Earth's center, while point b is the origin of B frame and is located at the center of the $+z$ face of the satellite.

In order to facilitate shadow and eclipse calculations, the Sun vector from the satellite body center $\vec{r}_{s/b}$ is expressed in the B frame using the orientation matrix $O_{B/I}$, as given in Eq. (2.7).

$$\vec{r}_{s/b}\big|_B(t) = O_{B/I}(t)\,\vec{r}_{s/b}\big|_I(t). \tag{2.7}$$

$O_{B/I}$ is the orientation of the frame B relative to the frame I. It is a function of time as the spacecraft's orientation relative to the inertial frame will change during the course of an orbit.

$O_{B/I}$ is calculated with

$$O_{B/I}(x_\beta\ , t) = O_{B/O}(x_\beta)O_{O/I}(t), \tag{2.8}$$

where,

$$O_{B/O}(x_\beta) = \begin{bmatrix} \cos(x_\beta) & \sin(x_\beta) & 0 \\ -\sin(x_\beta) & \cos(x_\beta) & 0 \\ 0 & 0 & 1 \end{bmatrix}, \tag{2.9}$$

$$O_{O/I}(t) = \begin{bmatrix} \hat{i}_o\Big|_I(t) & \hat{j}_o\Big|_I(t) & \hat{k}_o\Big|_I(t) \end{bmatrix}^T. \tag{2.10}$$

The vectors $\hat{i}_o$, $\hat{j}_o$, $\hat{k}_o$ are the basis vectors of the LVLH frame and are defined by the unit position vector ($\hat{r}_{b/o}$) and velocity vector ($\hat{v}_{b/o}$) of the satellite as follows,

$$\hat{k}_o = -\hat{v}_{b/o},\ \hat{j}_o = \hat{r}_{b/o} \times \hat{k}_o,\ \hat{i}_o = \hat{j}_o \times \hat{k}_o. \tag{2.11}$$

Next, the following process is used to transform the sun vector in the body frame, $\vec{r}_{s/b}\big|_B$, to a spherical, unit-vector representation, $\hat{r}_{s/b}\big|_S$. This body-fixed spherical frame, S, is called the attitude sphere, and it has been used to optimize directional sensors on a satellite [51]. The attitude sphere is adopted here to optimize the fixed angle of the photovoltaic panels and is shown in Fig. 2.6.

In S, the inclination angle from the z-axis is θ, while the azimuth angle around the z-axis as measured from the x-axis is φ. The mapping from Cartesian to spherical coordinates of the Sun vector ($\vec{r}_{s/b}\big|_B$) is defined as follows,

$$\vec{r}_{s/b}\big|_B(t) \mapsto \vec{r}_{s/b}\big|_S(t), \tag{2.12}$$

$$\vec{r}_{s/b}\big|_B(t) = [x(t),\ y(t),\ z(t)],$$

$$\vec{r}_{s/b}\big|_S(t) = [\theta(t),\ \varphi(t),\ \rho(t)],$$

$$x(t) = \rho(t)\sin\theta(t)\cos\varphi(t),$$

$$y(t) = \rho(t)\sin\theta(t)\sin\varphi(t),$$

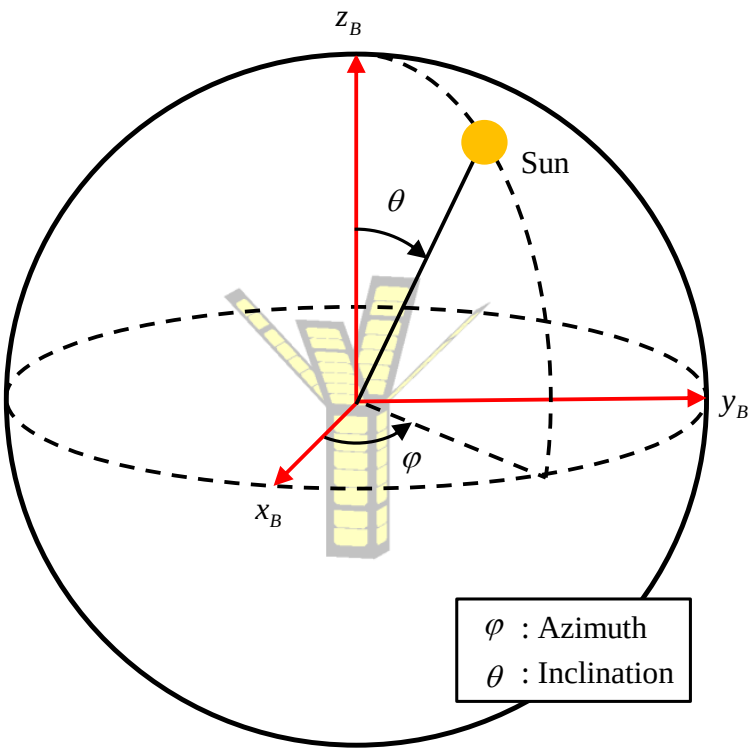

Figure 2.6: The Sun position in the body-fixed spherical frame S.

$$z(t) = \rho(t)\cos\theta(t),$$

$$\rho(t) = \sqrt{x(t)^2 + y(t)^2 + z(t)^2}.$$

Next, $\vec{r}_{s/b}\big|_S$ is converted to a unit vector, $\hat{r}_{s/b}\big|_S$ since only the direction is considered at this time, [4]

$$\hat{r}_{s/b}\big|_S = \{(\theta, \varphi, 1)\,|\theta \in [0°, 180°]\,, \varphi \in [0°, 360°)\}\,.$$

Fig. 2.7 plots the example motion of the Sun in the S frame for a year time horizon. The left portion of the figure is the attitude sphere where color intensity is proportional to the total time in the Sun at the given angle. On the right, the sphere is mapped to two dimensions, inclination and azimuth, again with color proportional to

[4]We assume solar illumination is constant over the given time interval.

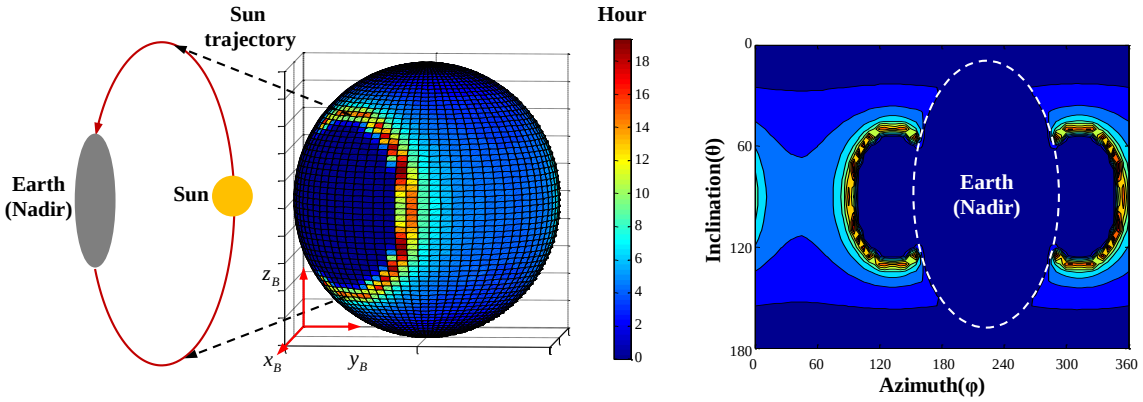

Figure 2.7: Sun angle mapping onto the attitude sphere (Left) and the azimuth-inclination plane (Right) for an example orbit : $i = 60°$, $\Omega = 90°$ over a one year simulation.

total time in the sun during the simulation. There are distinct regions of greater sun exposure, and there are also regions which experience no exposure to the sun (such as the nadir-pointing face). These plots provide insight into where photovoltaic panels would be most and least effective.

2.3.3 Calculation of Photovoltaic Array Illumination, Power, and Energy

Given a distribution of Sun position over the attitude sphere of a satellite, a technique is now needed to assess the photovoltaic array illumination for each point of the sphere. This will enable power and energy generation to be calculated. This is particularly difficult due to the complex geometries of the space-dart, and an analytic solution was not found. Thus, a numeric technique and tool were developed that use the graphic capabilities of the OpenGL, an API for rendering 2D and 3D graphics [52].

A tool was developed that creates a rendered scene in OpenGL using a CAD model of the spacecraft. The CAD model captures the spacecraft geometry as well as the deployable panel angle, x_α. In the scene, each cell is modeled and colored white while the background and everything else that is not a cell are colored black.

An orthographic camera is placed facing the spacecraft along the vector to the Sun, $\hat{r}_{s/b}\big|_S$, which represents a particular location on the attitude sphere. The cells visible to the camera are the ones that are illuminated when the Sun is in this position. The orthographic nature of the camera produces a 2D rendering of the 3D CAD model. This effectively implements the dot product between the Sun vector and the photovoltaic face needed for power calculation. Fidelity of the rendering and illumination calculation is increased by increasing the number of pixels in the scene. Pixels are converted to area depending on pixel density and CAD dimensions.

The camera position, which represents the Sun angle, is then moved through 4π steradians to calculate illumination for each possible Sun position, that is, the angles θ and φ are varied throughout their range in the attitude sphere. Step size can be varied to meet geometric complexity and fidelity requirements. For each cell on each panel, the illumination value is calculated for each Sun position. A graphical representation of this calculation is shown in Fig. 2.8. The color bar maps the ratio of increased illumination area which varies from 0.0 to 1.0 (blue to red, respectively). This ratio includes shadow effects of other panels and the cosine area decrease due to non-orthogonal illumination angles. Fig. 2.8(a) provides an example of these shadow effects as the deployed panels shade a particular cell at certain angles.

The effective area of illumination for each cell is then combined into a total area value of photovoltaic illumination for each Sun position. The total illumination area A_{total} is calculated as follows,

$$A_{total}\left(x_\alpha,\ \varphi(t), \theta(t)\right) = \sum_{i=1}^{84} A_i\left(x_\alpha,\ \varphi(t), \theta(t)\right). \tag{2.13}$$

where i is the photovoltaic cell number. The A_{total} calculations for several example configurations are presented in Fig. 2.9.

With this illumination area A_{total}, it is possible to calculate instantaneous power

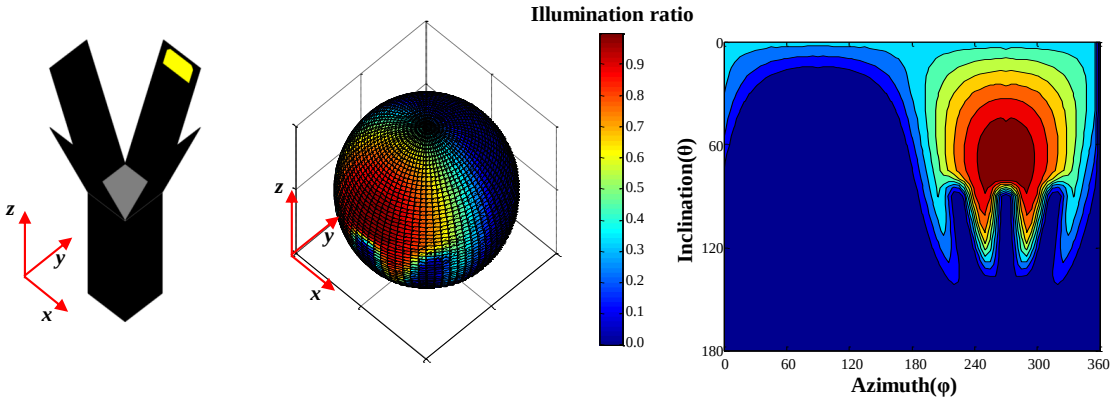

(a) Shadowing/Illumination ratio analysis of '$+b$' panel '7th' cell at $x_\alpha = 20°$.

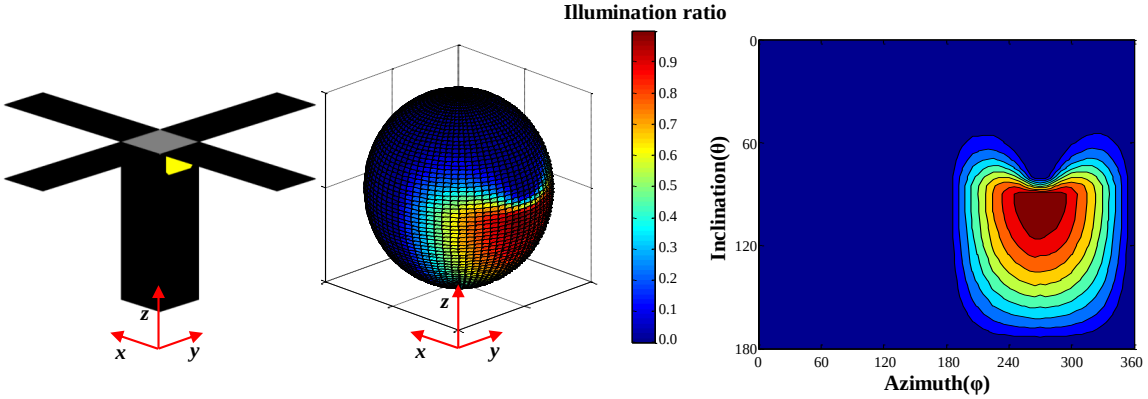

(b) Shadowing/Illumination ratio analysis of '$-y$' panel '1st' cell at $x_\alpha = 90°$.

Figure 2.8: Shadowing/Illumination ratio analysis of photovoltaic cells.

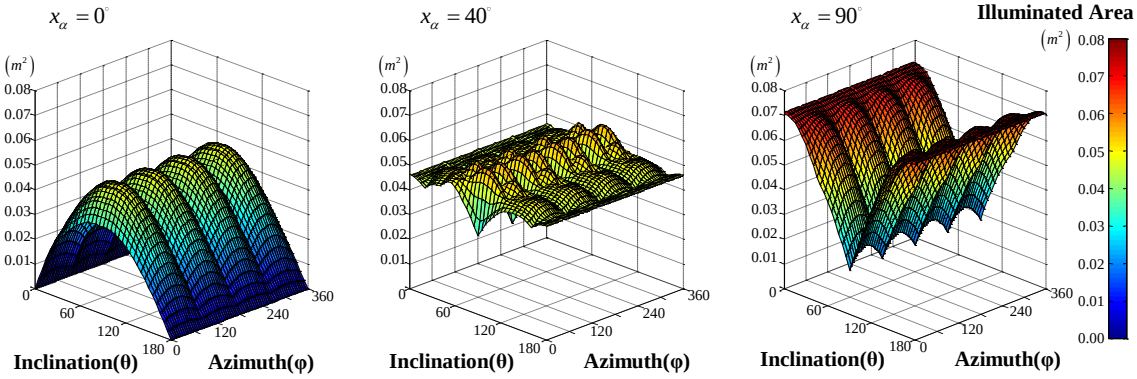

Figure 2.9: The total illuminated area of the photovoltaic cells as a function of Sun position in the body-fixed, spherical coordinate system.

generation P_{solar} and total energy collection $\mathcal{J}$, both of which are needed for assessing the objective function.

$$\begin{aligned} P_{solar}\left(\mathbf{x},\mathbf{p},t\right) &= S_0\varepsilon_{cell}A_{total}\left(\mathbf{x},\mathbf{p}_{orbit},t\right) \\ &= S_0\varepsilon_{cell}A_{total}\left(x_\alpha,\ \varphi(t),\theta(t)\right). \end{aligned} \tag{2.14}$$

S_0 is the solar constant. Via the method above, the A_{total} calculations were reduced to be a time-varying function of the design variables.

Energy $\mathcal{J}$ is calculated from the integration of P_{solar} over a given time horizon T,

$$\begin{aligned} \mathcal{J}\left(\mathbf{x},\mathbf{p}\right) &= \int_0^T P_{solar}\left(\mathbf{x},\mathbf{p},t\right)dt \\ &= \int_0^T S_0\varepsilon_{cell}A_{total}\left(\mathbf{x},\mathbf{p}_{SC},t\right)dt \\ &= \int_0^T S_0\varepsilon_{cell}A_{total}\left(\left[x_\alpha,\ x_\beta\right],\mathbf{p}_{SC},t\right)dt \\ &= \int_0^T S_0\varepsilon_{cell}A_{total}\left(x_\alpha,\ \varphi(t),\theta(t)\right)dt. \end{aligned} \tag{2.15}$$

2.3.4 Simulator Overview

The simulator consists of two main modules, and is built in a MATLAB/Simulink ™ framework. The first module generates and calculates the Sun-exposed area of each angle with respect to incident Sun angle. A simplified CAD model of the satellite is loaded into MATLAB for processing. The OpenGL module in MATLAB is used to calculate the sun exposed area for each Sun angle. Data is stored for use by the second module.

The second module simulates power generation with Simulink. The module models the orbit and attitude dynamics, the frame conversion and the power generation. To

accelerate simulation speed, C++ auto coding function is used. The simulation can be adapted for different missions by changing the input photovoltaic panel CAD file and panel configuration.

2.4 Simulations

With this methodology, simulations were performed to select optimal design variable values in relation to various parameters for the CADRE mission. A simulation period of one year was used as it is a typical mission life time for small, Low Earth Orbit (LEO) satellites and because it provides full coverage of seasonal effects. For future simulations of shorter term missions launched into lower altitudes, a shorter simulation time period is recommended. Starting the simulation at different times can account for launches during different seasons. Design variables were restricted to the following cases to simplify assessment while providing meaningful, practical data.

$$(x_\alpha,\ x_\beta) \in \{(0^\circ,\ 0^\circ),\ (90^\circ,\ 0^\circ),\ (0^\circ,\ 45^\circ),\ (90^\circ,\ 45^\circ)\}.$$

Orbital parameters were also simplified, and this process is described below in Section 2.4.1. Simulation outputs included the orbital average, maximum, and minimum power plots over the full time horizon as well as short-term, six hour simulations to provide insight into smaller scale power generation features. Given the simplification of the design variable options, a brute force simulation was employed to simulate all possible configurations in the design space of x_α and x_β [5]. Each of the simulation scenarios and resulting data are described below with a deeper discussion of results in Section 2.5.2.

[5]Each case of simulations took 3 to 5 minutes for one year simulations with MATLAB on Windows 7 3.40GHz PC.

2.4.1 Simplification of Orbital Parameters

The impact of orbital parameters on Sun angles and power generation is complex. The satellite orientation and the orbital parameters define the geometric relationship between the Sun and the satellite, which is the angle between the vector to the Sun and the photovoltaic panels. Complexity is compounded in that most small satellites are launched as secondary payloads which eliminates the mission's ability to pick an optimal orbit. Thus, since an optimal orbit cannot typically be selected, a technique for design optimization given a particular orbital scenario is useful.

While the model and simulator support an exhaustive and potentially time intensive search of various orbital parameters, some simplifications are possible for typical LEO small satellites. This is relevant to our example mission, CADRE, which seeks a high inclination (greater than 60°) and altitude less than 700 km. First, a circular orbit is assumed. In a review of recent LEO launches [6] [7], it was found that more than 81% of the satellites had an eccentricity less than 0.01. This simplifies analysis by enabling removal of the argument of perigee (ω) since circular orbits do not have a defined perigee.

Inclination (i) and the right ascension of the ascending of the node (Ω) determine the orientation of the orbital plane relative to an inertial reference frame, and thus are important in determining angles from the satellite to the Sun. Inclination is included and varied throughout the simulations. Ω is somewhat difficult to consider as it couples with i to produce sun-synchronous orbits. The year long simulations average out the time-varying effects of Ω and sun-synchronous orbits are treated as special, specific examples. The semi major axis (a) determines time in eclipse, and must be considered directly as a simulator parameter.

The impact of Ω and i for lower inclination orbits on power generation is shown

[6] Michael's List of Cubesat Satellite Missions, http://mtech.dk/thomsen/space/cubesat.php
[7] Radio Amateur Satellite Corporation, http://www.amsat.org/amsat/ftp/keps/current/amsat.all

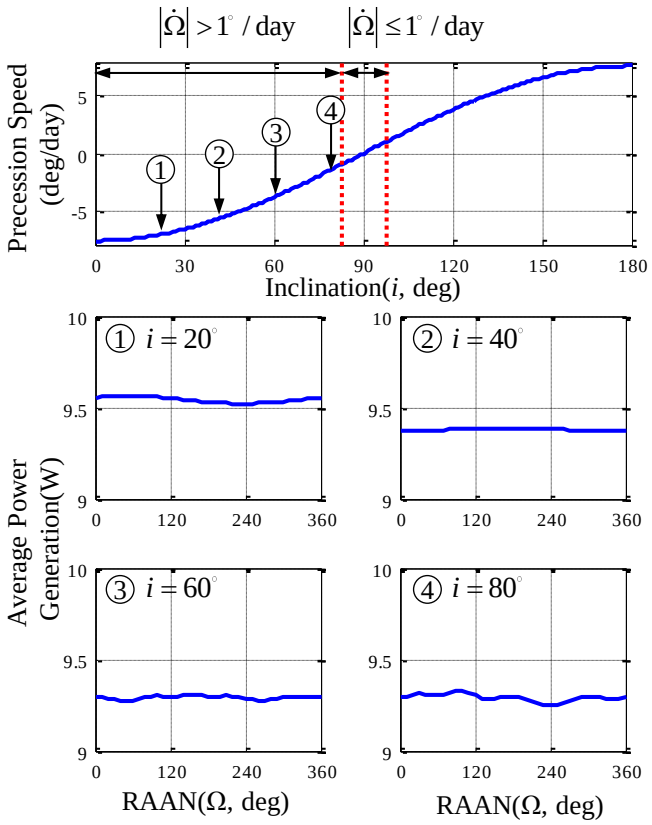

Figure 2.10: The precession rate, $\dot{\Omega}$, at different inclinations, and the average power generation in these differing orbits.

in Fig. 2.10. The top portion of the figure plots the orbital precession speed as a function of i. For inclinations less than 81° at this altitude, RAAN will vary over 360° during a one year simulation period. The impact of this precession on power generation is shown in the lower four plots of Fig. 2.10. A specific simulation was run on CADRE with the panel angle at (90°) and the roll angle at (45°). Four plots of data are shown with i fixed at 20°, 40°, 60° and 80° and RAAN varied over 360°.

In contrast, the precession rate for high inclination orbits is relatively slow, which dramatically impacts photovoltaic power generation. In this work, we model these high inclination orbits as sun-synchronous, and various sun-synchronous orbits with different RAAN values are evaluated.

During the following simulations, S_0, the photovoltaic power flux density, is as-

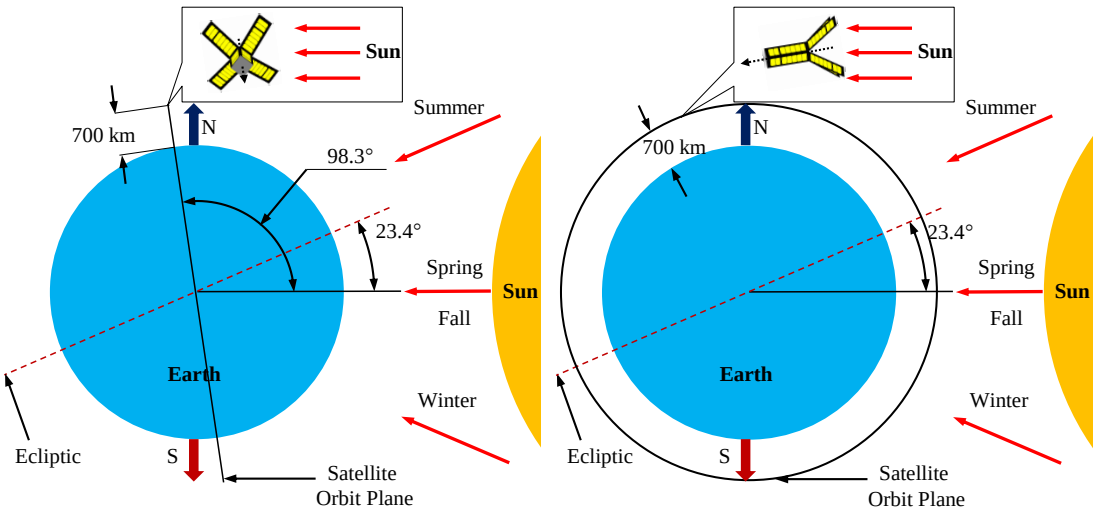

(a) Dawn-Dusk orbit.

(b) Noon-Midnight orbit.

Figure 2.11: Overview of different sun-synchronous orbits.

sumed to be 1367 W/m^2 [53], and constant during the simulations. It does vary approximately $\pm 3.5\%$ depending on season [54]. However the simulations are over a year, therefore a yearly average is used. If the mission life time is targeting specific period shorter than 3 month, a more accurate model of S_0 can be used. Photovoltaic cells are assumed to have an efficiency of 28%.

2.4.2 Sun-synchronous Orbits

The first set of simulations considers circular, sun-synchronous orbits at an altitude of 700 km and an inclination of 98.33°. Fig. 2.11 provides an overview of a sun-synchronous orbit (not to scale). This orbit precesses at the same rate that the Earth rotates around the Sun. Thus, the orbital plane maintains near constant β angle (the angle of the orbital plane with respect to the Sun [55]) throughout the year and, even with the effect of the obliquity (23.4°), the yearly variation is relatively small compared to other orbits. In the simulations, RAAN was varied to produce noon-midnight and the dawn-dusk orbits. These are good examples with which to begin because the geometry is simplified, the angle from the Sun to the orbital plane

is nearly constant, and it is easier to intuitively understand the results.

2.4.2.1 Noon-Midnight Orbit Case

The simulation results of the noon-midnight orbit with variations in the design variables are presented in Fig. 2.12. The four plots of the figure have constant roll angle along a row and constant panel deployment angle along a column. The first observation is that the average and maximum power values throughout the orbit have variations (0.1-10%) over the year. These are due to seasonal effects imparted by the Earth's obliquity. Second, a 90° panel deployment angle produces more power, approximately twice as much, than a 0° panel deployment angle. With a 90° panel deployment angle, four faces of the panels are simultaneously illuminated, see ④ of Fig. 2.12(b) while in the 0° angle case, at most only two full panels are exposed.

For the roll angle, x_β, an angle of 45° produces greater power than 0°. At 45°, there is an approximately 1.4 times $(2 \cdot \cos 45°)$ increase in photovoltaic panel area along the z-axis of the satellite, which results in increased power generation. The impact of this increase is greater for a panel angle of 0° since the cells are oriented along the z axis. For the 90° panel deployment angle, the majority of the surface area from the deployed panels is in the x-y plane, thus, in this case, the roll angle does not contribute significantly to the orbit average.

In summary, for the noon-midnight sun-synchronous orbit, maximum power generation occurs when $x_\alpha = 90°$ and $x_\beta = 45°$.

2.4.2.2 'Dawn-Dusk' Orbit Case

The simulation results of the 'Dawn-Dusk' Orbit are presented in Fig. 2.13. Note that with the selected orbit altitude of 700 km, seasonal periods of eclipse occur due to the Earth's obliquity. Altitudes greater than approximately 1000 km will see continuous illumination throughout the year.

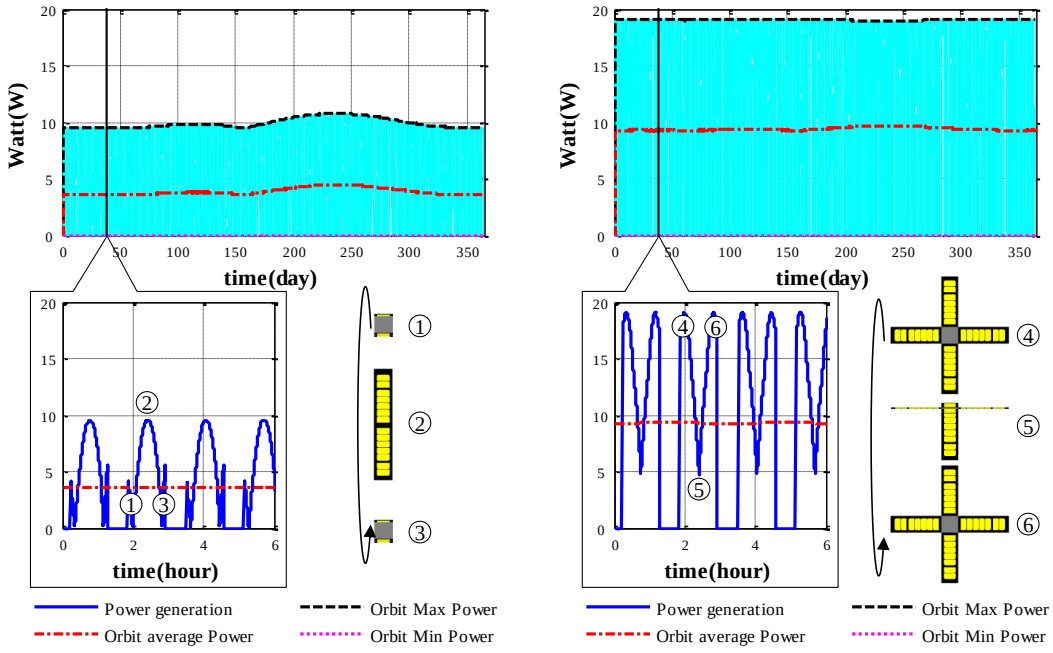

(a) $x_\alpha = 0°$, $x_\beta = 0°$.

(b) $x_\alpha = 90°$, $x_\beta = 0°$.

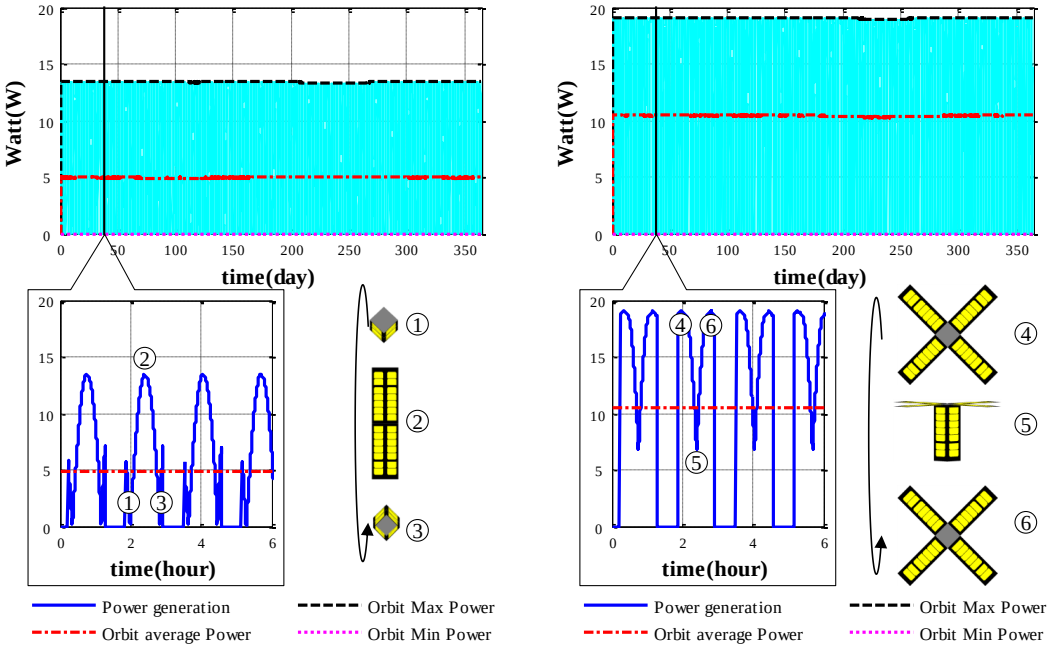

(c) $x_\alpha = 0°$, $x_\beta = 45°$.

(d) $x_\alpha = 90°$, $x_\beta = 45°$.

Figure 2.12: One year simulation of Noon-Midnight orbit and 6 hour simulation of the 40th day with a diagram of CADRE attitude to the Sun.

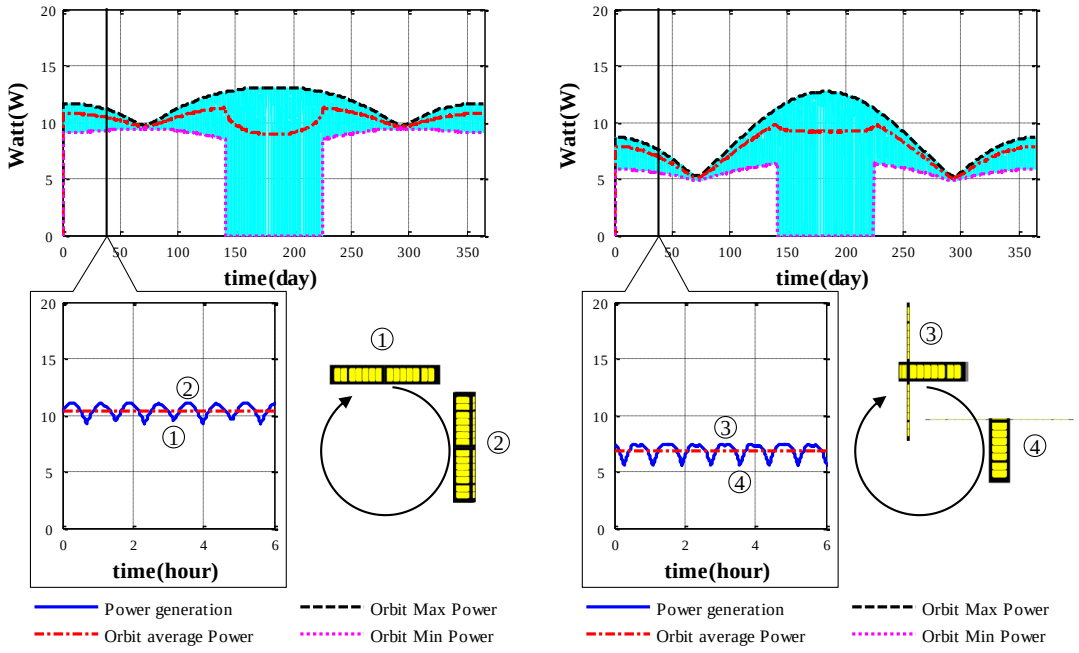

(a) $x_\alpha = 0°$, $x_\beta = 0°$.

(b) $x_\alpha = 90°$, $x_\beta = 0°$.

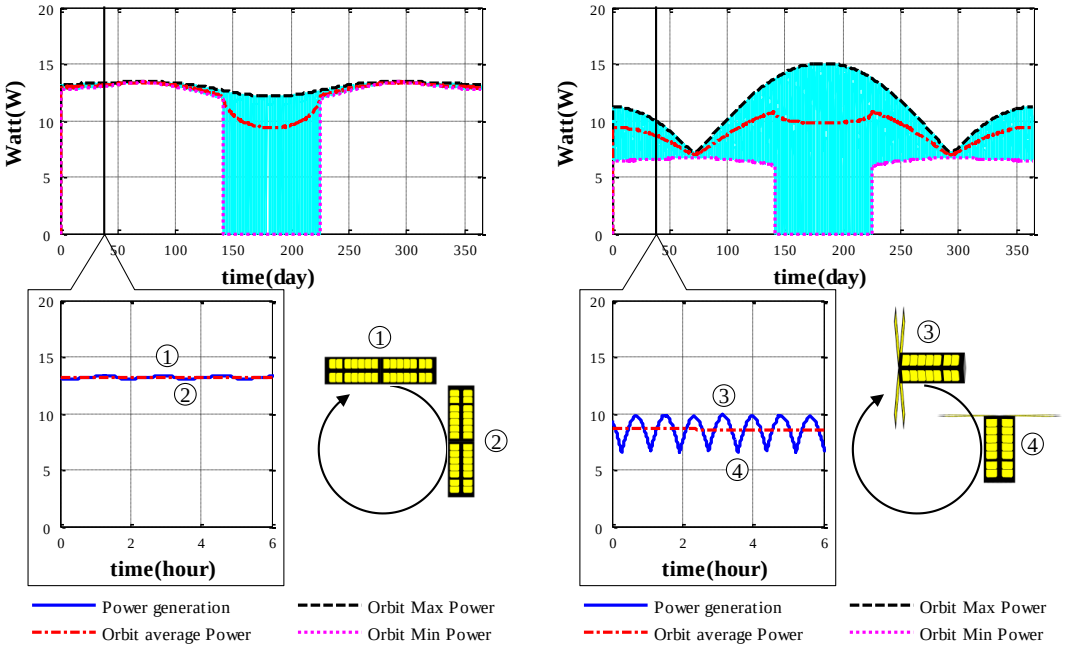

(c) $x_\alpha = 0°$, $x_\beta = 45°$.

(d) $x_\alpha = 90°$, $x_\beta = 45°$.

Figure 2.13: One year simulation of 'Dawn-Dusk' orbit and 6 hour simulation of the 40th day with a diagram of CADRE attitude to the Sun.

Roll angle results are similar to the noon-midnight orbit simulations. With a 45° roll angle, there is an increase in photovoltaic cell surface area along the z-axis of the satellite, and the increase is relatively greater when the panel deployment angle is at 0°. For this panel deployment angle, results are the opposite with respect to the noon-midnight case since the Sun never illuminates along the z-axis, only perpendicular to the z-axis. Panels deployed at 90° are only ever slightly illuminated since sun-synchronous orbits never have a β angle equal to 90°. Variations in the dawn-dusk simulations are seasonal and primarily generated by β angle variation.

In summary, for the 'Dawn-Dusk' sun-synchronous orbit, maximum power generation occurs when $x_\alpha = 0°$ and $x_\beta = 45°$.

2.4.3 Non-Sun-Synchronous Orbits

Another class of orbits potentially applicable to CADRE are high inclination, but non-sun-synchronous orbits. An altitude of 500 km is selected and inclinations of 67° and 82° are simulated. The simulations are over a one year time horizon and minimum, maximum, and average power numbers are summarized below in Fig. 2.14 and Fig. 2.15.

2.4.3.1 Case 1 : Inclination 67° Orbit

Strong seasonal effects in power generation are evident in this orbit, as shown in Fig. 2.14. There are distinct variations in average, maximum, and minimum power generation values for all configurations of the design variables. As the orbit precesses at a rate not synchronized with the Earth's rotation around the Sun, these variations occur.

For the perpendicular panel deployment angle, $x_\alpha = 90°$, there are strong variations in maximum power generation where some periods produce twice as much power as others. Interestingly, periods of full illumination produce less average power due to

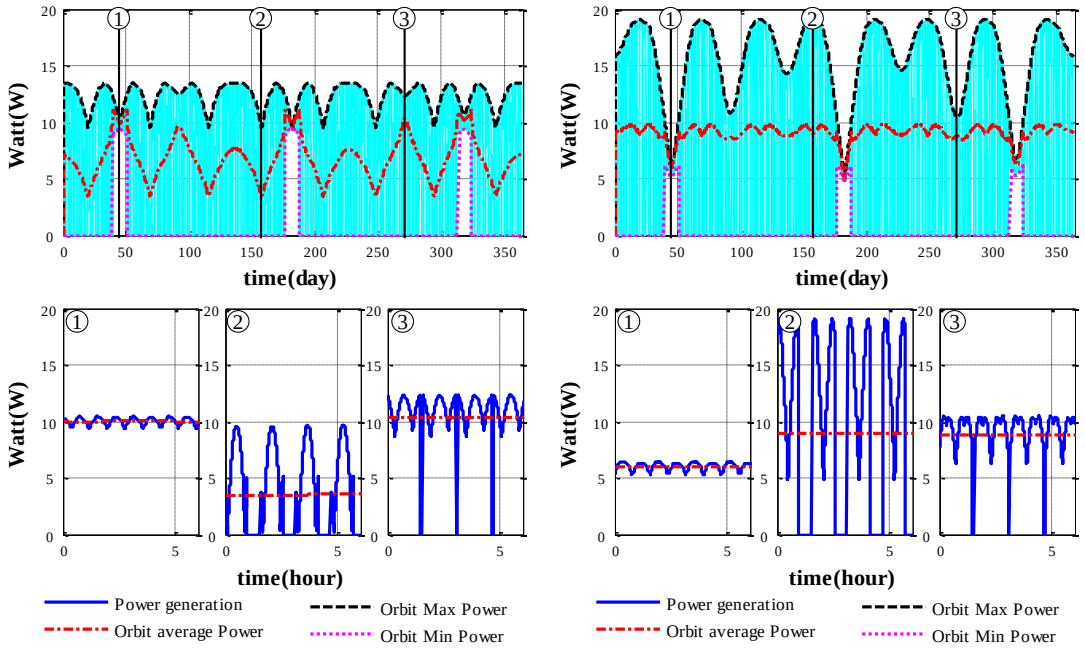

(a) $x_\alpha = 0°$, $x_\beta = 0°$.

(b) $x_\alpha = 90°$, $x_\beta = 0°$.

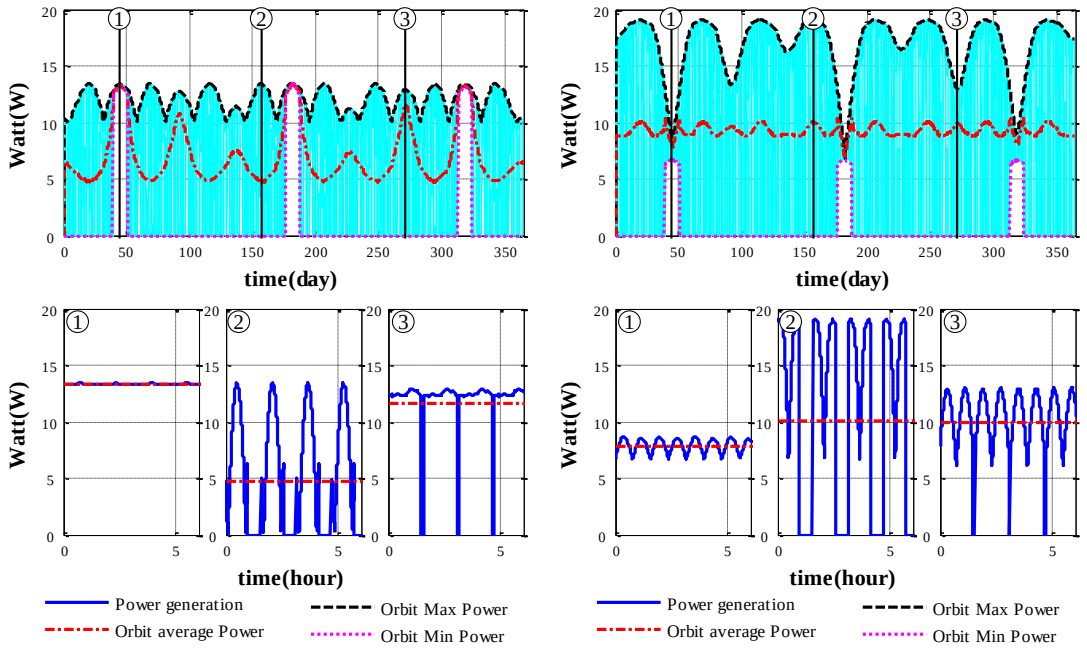

(c) $x_\alpha = 0°$, $x_\beta = 45°$.

(d) $x_\alpha = 90°$, $x_\beta = 45°$.

Figure 2.14: One year simulation of 67° inclination orbit and 6 hour simulation of sample days with different design variable values.

the deployed photovoltaic panels seeing less direct sunlight. Roll angle, x_β, impacts power generation 18 - 26%.

For the parallel panel deployment angle, $x_\alpha = 0°$, again there are strong variations in maximum and minimum power, and the average power can vary by over 50%. Maximum peak and average power occurs during the periods of full illumination. Roll angle, x_β, impacts power generation 7 - 25%.

2.4.3.2 Case 2 : Inclination 82° Orbit

In the 82° inclination orbit simulation, seasonal variations occur similar to the 67° case, but the variations are slower due to the slower variation in β angle. For example, three full illumination time periods, shown by the white colored gaps between 80-100 days, 170-190 days, and 250-270 days occur at similar times for both the 82° and 67° inclination orbits, but have a longer duration in the 82° inclination orbit. The trends in power generation are similar to the previous orbit example.

2.5 Discussion - Optimal Angles

With an extension to the simulations and initial results from above, optimal angles for the CADRE mission are determined below for potential orbit candidates. Given that CADRE, as a CubeSat, will fly as a secondary payload, orbital parameters are not firmly established, and thus a range of angles for a variety of orbits are useful to the design engineers. The final angles will be set and implemented once the orbit is known.

Optimal angles for several orbits using the first objective function, maximum energy (or maximum average power), are determined below. This objective function is used since we expect CADRE to be power limited due to payload and communication power requirements. Two roll angles are used, $x_\beta \in (0°,\ 45°)$, and the deployment panel angle, x_α, is varied from 0° to 90°. The results are plotted in 3D figures and

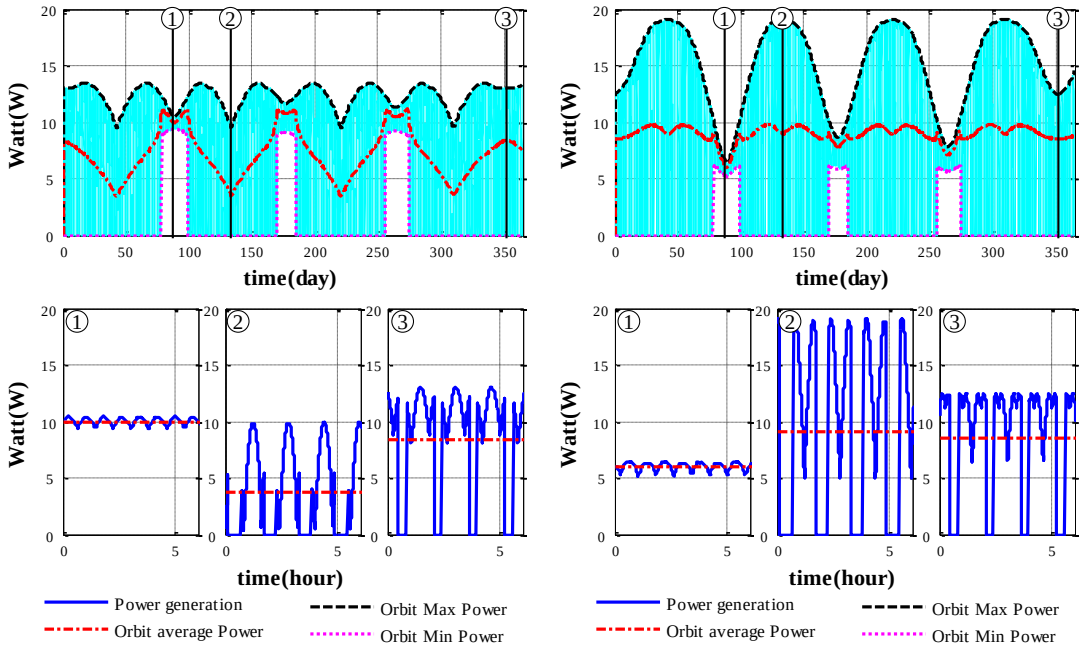

(a) $x_\alpha = 0°$, $x_\beta = 0°$.

(b) $x_\alpha = 90°$, $x_\beta = 0°$.

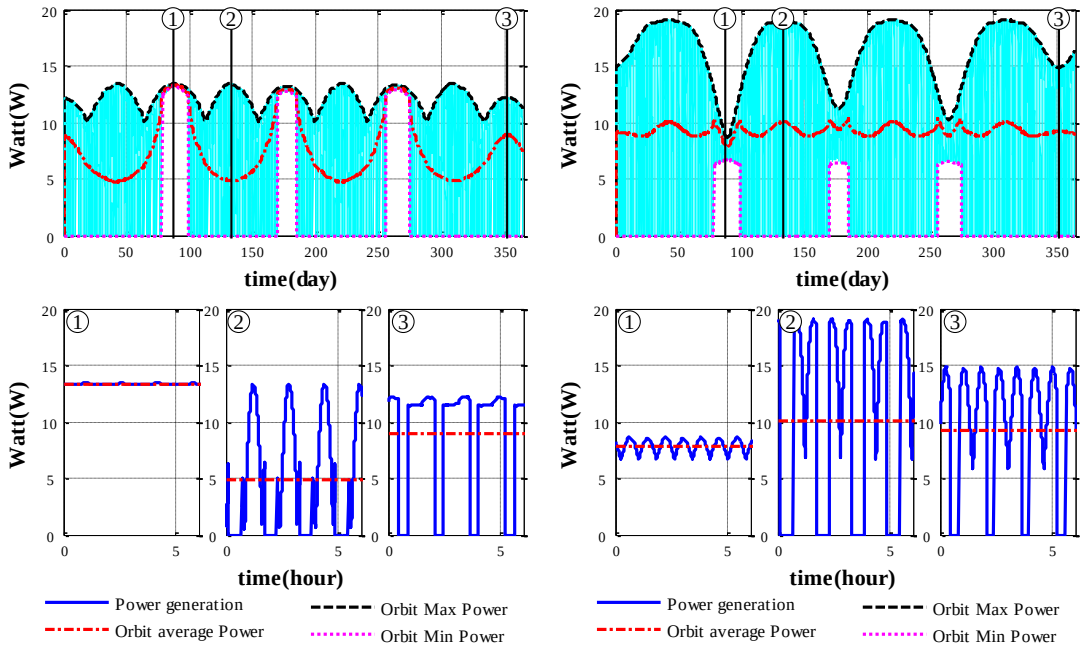

(c) $x_\alpha = 0°$, $x_\beta = 45°$.

(d) $x_\alpha = 90°$, $x_\beta = 45°$.

Figure 2.15: One year simulation of 82° inclination orbit and 6 hour simulation of sample days with different design variable values.

a projection to 2D contour lines in Fig. 2.16 and 2.17 for sun-synchronous and non-synchronous orbits, respectively.

2.5.1 Sun-synchronous Orbits

Multiple year-long simulations were run with varying panel deployment angles, roll angles, and RAANs while the orbital altitude was fixed at 700 km. The simulated launch date was 20 March 2014, which is a spring equinox. In sun-synchronous orbits, RAAN varies by approximately 1° and thus determines the β angle. β is constant as the varying RAAN rate matches the orbital period of the Earth around the Sun. Thus, for a given orbit determined by the RAAN, Fig. 2.16 plots the average power for varying deployment and roll angles at a constant β angle. Note that average power numbers are given in the plot and text below since power is more typically used by our design teams. The average power multiplied by one year will provide total energy generated.

Peak power production occurs in the dawn-dusk orbits, as expected since they contain the largest illumination time periods. The peak points are denoted by red triangles in Fig. 2.16. For a roll angle of 0°, peak power is 11.98 W at $x_\alpha = 27°$. At a roll angle of 45°, peak power is 13.86 W at $x_\alpha = 21°$. Also, the interesting example of noon-midnight orbits are marked with blue squares. The deep valley and peaks of the plots are expected due to the constant β angle. The lack of variability in β limits the coverage of illumination of the satellite; only a limited range of the attitude sphere receives light. Thus, only a limited number of angles see maximum illumination.

Roll angle has an impact on energy generation, up to 15.6% for the dawn-dusk orbits and 9.6% for the noon-midnight orbits. This is primarily due to the increased illumination of the body-mounted panels.

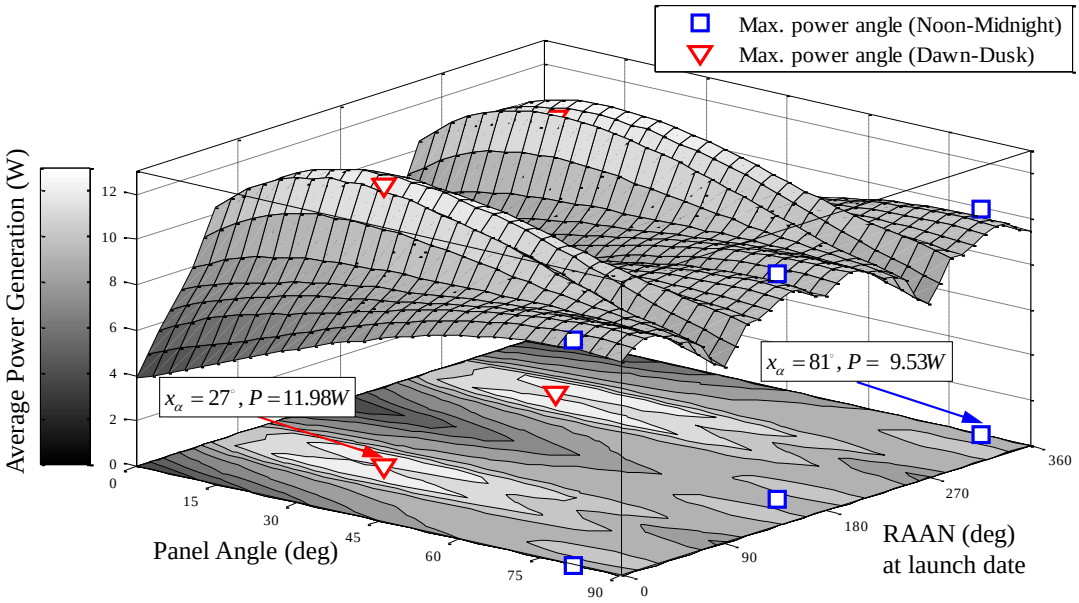

(a) $x_\beta = 0°$.

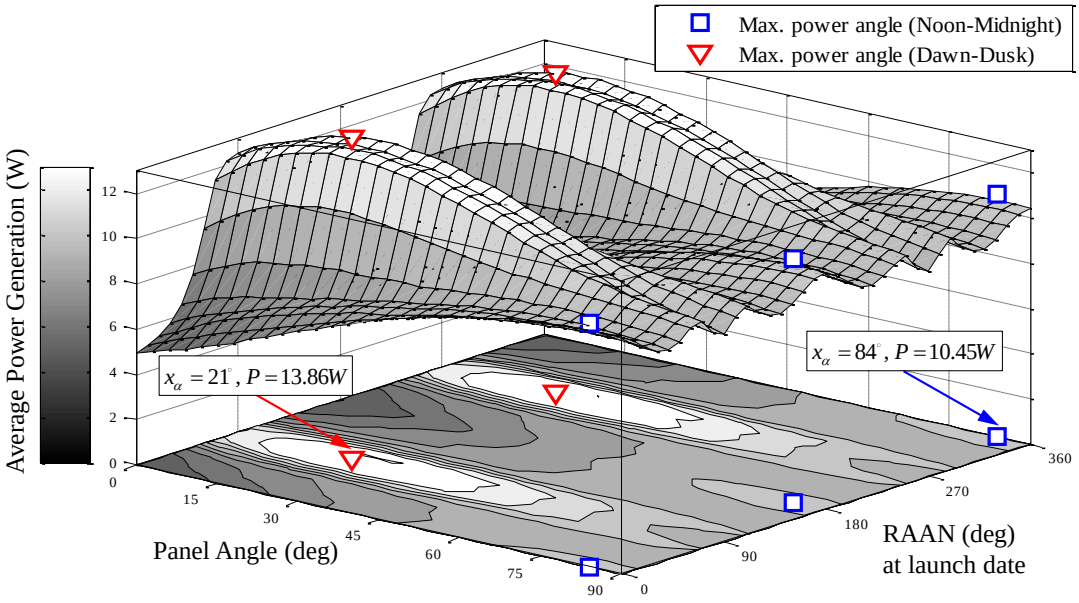

(b) $x_\beta = 45°$.

Figure 2.16: Average power generation of sun-synchronous orbits with varying RAANs and photovoltaic panel angle.

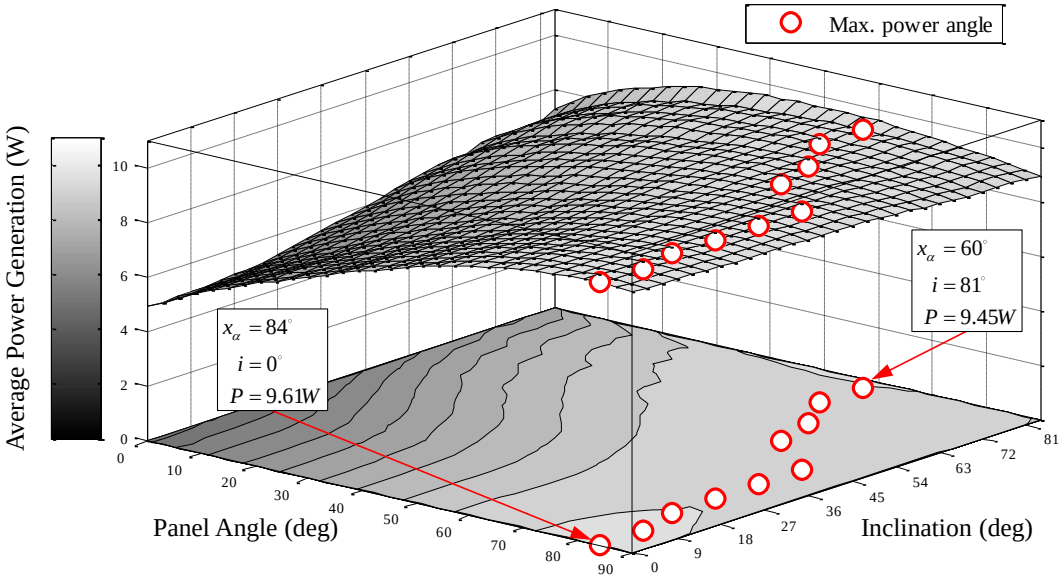

(a) $x_\beta = 0°$.

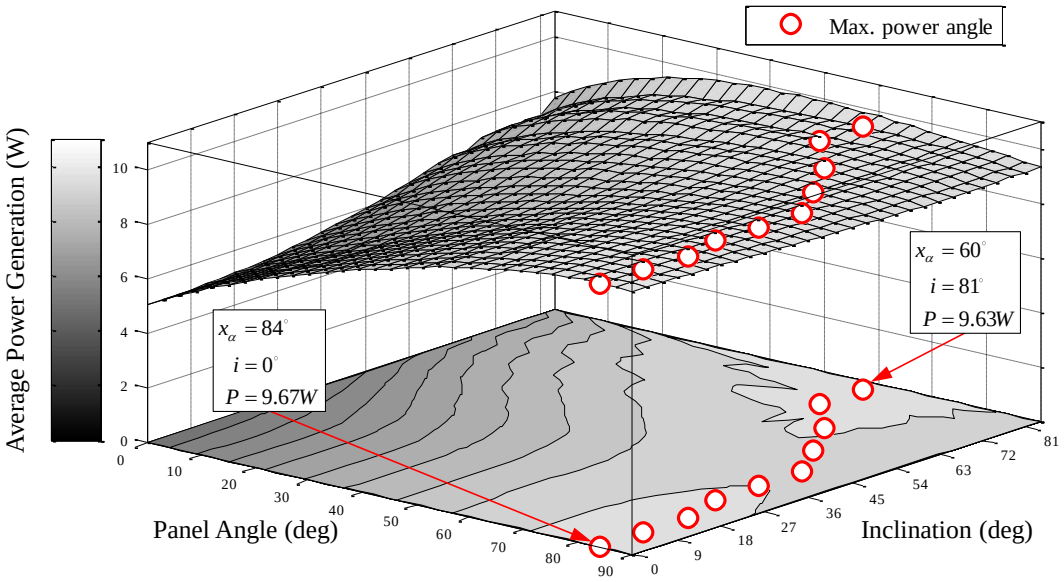

(b) $x_\beta = 45°$.

Figure 2.17: Average power generation of non-sun-synchronous orbits with varying inclinations and photovoltaic panel angles.

2.5.2 Non-Synchronous Orbits

Similar exhaustive simulations were run for non-synchronous orbits with varying panel deployment and roll angles. However, the orbit inclination was changed rather than RAAN. RAAN is time-varying (the orbit is precessing) at a rate that alters the β angle throughout the year-long simulations. Thus, the RAAN impact is averaged out. The orbital altitude is fixed at 700 km and the inclination is varied from 0° to 90°. Results of the simulations are plotted in Fig. 2.17. These plots are distinctly different in that they lack the strong peaks of Fig. 2.16.

The general trend is that higher panel deployment angles produce more power for these lower inclination orbits. As the orbit precesses in a non-sun-synchronous manner, the β angle changes and the satellite is illuminated from additional angles; there is increased coverage of the attitude sphere. Higher panel deployment angles create diversity and higher illumination area, see Fig. 9. Peak power points for each inclination are identified by circles in Fig. 2.17. The effect of the roll angle on the power generation is smaller than in sun-synchronous orbit cases, and a 45° roll has better power generation.

2.6 Conclusion

We have developed a methodology and simulation environment for calculating power generation on satellites with complex photovoltaic panel geometries and for optimizing design variables that impact the power system. Several objective functions for optimizing power systems are identified: maximizing total energy, maximizing the minimum average power per orbit, and minimizing the variance in power generation. The developed simulation system is capable of identifying panel deployment and satellite roll angles to maximize total energy collected.

There are two key features of the system: the ability to quickly assess self-induced

shadowing and the ability to calculate sun angles in a body-fixed frame local to the satellite. Self-induced shadow is calculated using a CAD model of the system and OpenGL, a framework for advanced computer graphics. For a given sun angle, the illumination of photovoltaic cells is calculated and mapped to a body-fixed frame called the attitude sphere. Thus, for each potential direction to the Sun, a map of all photovoltaic cells that are illuminated is known. Orbital and attitude dynamics simulators are then used to calculate angles between the satellite and the Sun. These again are mapped to the attitude sphere and weighted according to occurrence during the simulation time period. These two outputs, shadow mapping and sun angle directions, provide fast calculations of power and energy generation capabilties of the satellite.

This system was applied to determine optimal design parameters for a common small satellite configuration, the space-dart. The space-dart is a 3U CubeSat with deployed photovoltaic panels, and resembles a dart or a shuttlecock. In particular, we used a space weather science mission referred to as CADRE that is in development at the University of Michigan. CADRE is power limited and its deployed photovoltaic panels create complex shadow geometries. Multiple simulations were performed for various roll angles of the satellite, panel deployment angles, and orbit scenarios. Close attention was given to sun-synchronous effects. The results show that power generation of a space-dart configuration can vary more than 40 percentage due to orbit geometries and the photovoltaic panel angle configurations. For a sun-synchronous, dawn-dusk orbit at 700 km, we estimated a peak average power generation of 13.86 W. For a non-synchronous orbit, the estimated peak average power was 9.6 W. These techniques can be applied to a variety of photovoltaic panel design problems where the sun angle to the panels and the panel orientation are dynamic.

An additional lesson learned in this effort is the strong coupling between satellite attitude and power generation. While this conclusion is somewhat obvious, the model

and solution together with simulation complexity demonstrates the need for a framework that captures the multiple dimensions of the full space system. As shown in the next chapter, additional disciplines such as thermal and communication are primary drivers in the highly coupled, small satellite systems. Thus, in the next chapter, we develop the capability to handle multdisciplinary optimization capable of using fast and accurate gradient-based optimizers.

CHAPTER III

Multidisciplinary Design and Operation Optimization of Small Satellite

3.1 Introduction

The complexity of power and attitude control optimization is evident in the advanced science mission, CADRE, which is in development at the Michigan eXploration Laboratory (MXL). CADRE's primary mission is to fly the Wind Ion Neutral Composition Suite (WINCS) payload, an instrument for measuring the composition and energy of neutral winds and inos in the thermosphere [48]. WINCS requires a considerable amount of power and data download capability while remaining in a specific attitude orientation for science operation. The simultaneous maximization of the power generation and data transmission under this attitude requirement must be considered in the system design process.

Motivated by this problem and the results of Spangel et al.[41], a novel approach to multidisciplinary design and operation optimization of a small satellite is developed. The problem of this section considers the satellite's operations regarding attitude rotation, communication, power, and photovoltaic array regulation, while the problem in [41] only considers GS operations, scheduling and the power of a satellite. The operation of the satellite during its mission period increases the total number of the

design variables to thousands. In addition, these operation variables are coupled with each other and also coupled with the geometry design variables such as the deployable photovoltaic panel angle and the antenna direction.

A large-scale MDO methodology which unifies the design and operation optimization of a spacecraft is adopted to the proposed problem [2]. The large number of disciplines and variables of the suggested problem are handled with gradient-based optimization, which performs better than gradient-free methods in large-scale optimization problems [56]. Sequential Quadratic Programming (SQP) and sparse linear algebra routines are also implemented to reduce the memory usage and computation time caused by the large number of variables. The gradient-based solver can find a solution faster if analytic derivatives are provided, so, to compute the analytic derivatives at a cost nearly independent of the number of design variables, the adjoint method developed by Martins [57] has been also implemented.

The structure of this chapter is as follows. First, the CADRE MDO problem is defined and constructed. Second, all disciplines used in the MDO problem are explained in detail. After that, the optimization results are presented and followed by a detailed analysis in the discussion section. As a conclusion, the method to apply the optimization results in orbit is summarized.

3.2 MDO Problem Definition

In this section, an objective function, design variables, and constraints of the MDO problem for our space system are introduced.

The objective function of our MDO problem is the total amount of downloaded data. This objective function is selected for its relevance to recent missions for which a method to maximize this quantity was highly desirable [58, 41].

The space system MDO problem includes many design variables such as deployable panel angle, installation of the photovoltaic or radiator cell, electric power distribu-

tion, antenna install angle and etc., which are closely coupled. For example, CADRE has four deployable panels and their angle needs to be decided upon. The amount of photovoltaic power generation depends on this panel angle setting which affects the mutual shadow casting between the body panels and the deployable panels. The complex shadows make specific photovoltaic cell positions less effective in power generation, so, a radiator cell can be installed instead of installing a photovoltaic cell, which is also a design variable that needs to be decided on. The installation of the radiator cell can reduce the temperature of the satellite body and deployable panel, which affects the efficiency of photovoltaic power generation and battery charging. The amount of data the communication system can send to the ground station is dependent on the amount of power this system has available to use. In general, the more power provided by the photovoltaic array and battery, the more data can be transmitted. Furthermore, if the ground station antenna is aligned with the satellite antenna, more data can be transferred with less power. However, to align satellite antenna, attitude operation is required and, sometimes, the actuator power spent in aligning the antenna is more than the power used by communicating without the alignment. To decide the value of various design variables suggested here, many

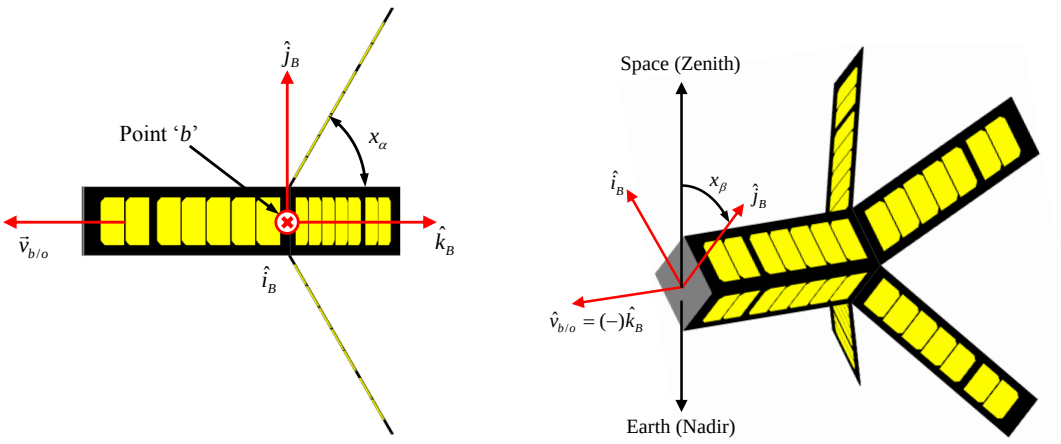

(a) CADRE panel angle.

(b) CADRE rotation angle.

Figure 3.1: Angle definitions of CADRE.

disciplines and their coupling need to be considered.

In addition, the operation profile can also be an important design variable in the space system MDO problem. So, CADRE's attitude operation profile over time is included in the MDO problem because attitude operation can help increase power generation and cool down the panel temperature when necessary. It may also help increase the antenna transmission gain by pointing the antenna to the ground station. The attitude operation and the geometric design must be optimized simultaneously since different operations require different geometry configurations. If the panel angles are optimized without the attitude operation in orbit, then the panel angles may not be optimal with the attitude operation in orbit. Another operation profile included in this MDO problem is the operation of the electric power system. CADRE requires optimal distribution of the power to the communication system and ADCS, so we make the optimizer decide the distribution of the power and also decide the optimal regulation operation of the photovoltaic array. The operation of the power system makes the number of resulting design variables reach tens of thousands, and also makes the MDO problem almost impossible to solve.

The space system MDO problem also includes many constraints such as the required attitude, battery depth-of-discharge (DOD) and others. For example, the attitude of WINCS, as introduced in the previous section, also requires the $-z$ axis to be parallel with the orbit velocity vector, which only allows the satellite rotate around the roll axis (see Fig. 3.1). Along with the attitude constraints, battery constraints such as charge/discharge rate and the depth-of-discharge limit are also important. If the depth-of-discharge limit is violated often, we can lose mission lifetime due to the battery lifetime loss.

To design such a complex space system with constraints, the relation between the disciplines need to be defined with the stated variables as shown in Fig. 3.2.

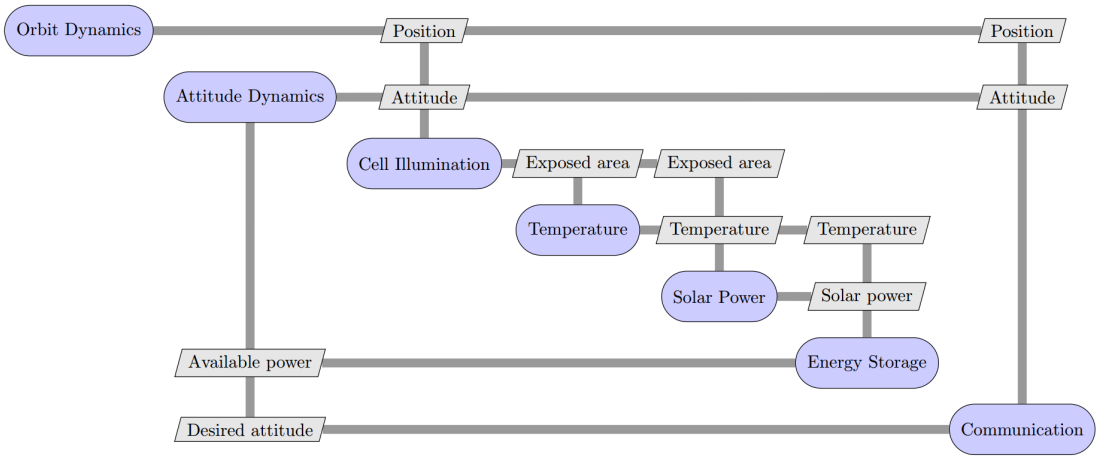

Figure 3.2: XDSM diagram for CADRE optimization [2].

3.3 Discipline Models

CADRE design problem includes orbit dynamics, attitude dynamics, photovoltaic power system, battery, thermal, and communication disciplines and each discipline is explained with the detailed description in the following section. Model parameters and numerical values that are implemented in this section are summarized in Table 3.1.

3.3.1 Orbit Dynamics

The equation of motion representing orbit dynamics can be divided into the calculation of the satellite position and the Sun position.

3.3.1.1 Satellite Position

The satellite position vector from Earth is computed in the Earth-centered inertial frame. The two body orbit motion with the Earth oblateness effect are assumed and the Earth oblateness effect can be expressed by including the J_2, J_3, and J_4 coefficients in the Eq. (3.1).

$$\begin{aligned}\ddot{\vec{r}} = -\frac{\mu}{r^3}\vec{r} &- \frac{3\mu J_2 R_e^2}{2r^5}\left[\left(1-\tfrac{5r_z^2}{r^2}\right)\vec{r}+2r_z\hat{z}\right] \\ &- \frac{5\mu J_3 R_e^3}{2r^7}\left[\left(3r_z-\tfrac{7r_z^3}{r^2}\right)\vec{r}+\left(3r_z-\tfrac{3r^2}{5r_z}\right)r_z\hat{z}\right] \\ &- \frac{15\mu J_4 R_e^4}{8r^7}\left[\left(1-\tfrac{14r_z^2}{r^2}+\tfrac{21r_z^4}{r^4}\right)\vec{r}+\left(4-\tfrac{28r_z^2}{3r^2}\right)r_z\hat{z}\right],\end{aligned} \tag{3.1}$$

where $\vec{r} = \vec{r}_{b/e}\big|_I = [r_x \ r_y \ r_z]^T$ and $r = \sqrt{r_x^2 + r_y^2 + r_z^2}$. The lower-case subscripts such as b, e represent the specific point which denote the satellite body and the Earth center respectively. $\vec{r}_{b/e}$ implies the vector pointing from the Earths origin to the satellites origin. The upper-case subscripts with the right bar indicate the reference frames of the vector and $\vec{r}|_I$ means the vector $\vec{r}$ resolved in the Earth-centered inertial frame. These J_2, J_3, and J_4 terms affect the orbit plane rotation (precession) and the deployable panel angle design with precession is more complex than the design without precession because the Sun incident angle to orbit plane(β angle) varies depending on the orbit inclination.

3.3.1.2 Sun Position

1. Sun

   To be able to estimate the Sun vector, the relationship between the Earth and the Sun has to be identified. It is well-known that the Earth revolves around the Sun but it is more convenient to describe the relationship from the Earth's point of view, as illustrated in the Fig. 3.3. The elevation, ε_S of the Sun from the Earths equator varies by $\pm 23°$. Kristiansen [3] proposed the following relationship to calculate the solar elevation:

$$\varepsilon_s = \frac{23\pi}{180}\sin\left(\frac{2\pi}{365}t_s\right), \tag{3.2}$$

   where t_s is the time elapsed since the first day of spring. It is assumed that orbit time is 365 days (a year) and that the Earth's orbit is circular because

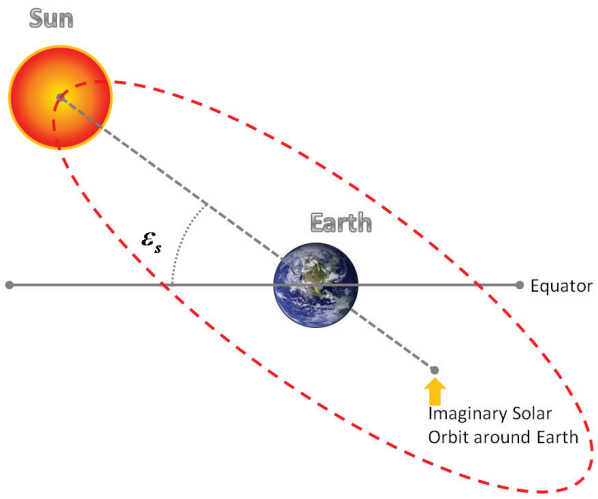

Figure 3.3: Sun elevation in an imaginary orbit around the earth [3].

this error has little affect on a constant parameter of solar pressure estimation. The Sun's position, λ_S, in this imaginary orbit around the Sun, is given by :

$$\lambda_s = \frac{2\pi}{365} t_s. \tag{3.3}$$

Knowing the elevation, ε_S, and the Sun's position in relation to the Earth, it is possible to calculate a vector pointing to the Sun. The calculation, starts with

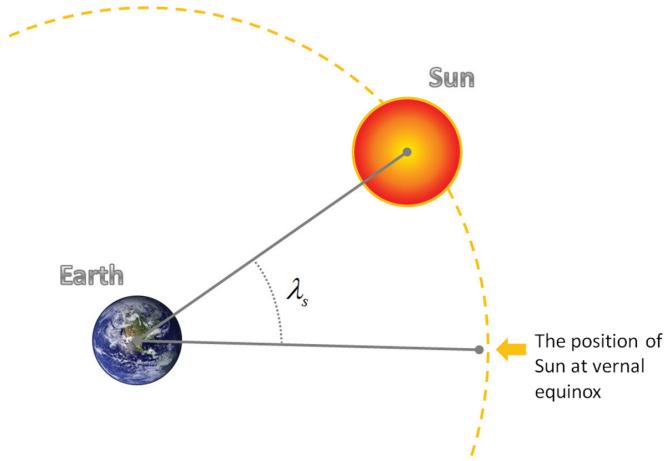

Figure 3.4: Sun position in imaginary orbit around Earth [3].

the initial position given on the first day of spring (vernal equinox),

$$\hat{r}^0_{s/e}\big|_I = \begin{bmatrix} 1 & 0 & 0 \end{bmatrix}^T. \tag{3.4}$$

Here, the lowercase subscript s/e implies the direction from the Earth to the Sun. Both the Sun's elevation and position describe its imaginary rotation around the Earth. The position vector can be calculated as rotations:

$$\hat{r}_{s/e}\big|_I = \begin{bmatrix} \cos(\varepsilon_s)\cos(\lambda_s) \\ \sin(\lambda_s) \\ \sin(\varepsilon_s)\cos(\lambda_s) \end{bmatrix}. \tag{3.5}$$

Here, $\hat{r}$ means the normalized unit vector. Using the inertial to body rotation matrix, the Sun's position in the body frame is computed, which is then converted into spherical coordinate values, azimuth and elevation, shown in Fig. 2.6. The equations for this conversion to spherical coordinates are introduced in the section 2.3.2.

2. Eclipse [2, 59]

   The eclipse of the Sun can be calculated by computing, d, between the position vectors from the Earth center to satellite and the unit position vector from the Earth center to the Sun in the ECI frame, i.e.,

$$d = \vec{r}_{b/e} \cdot \hat{r}_{s/e}. \tag{3.6}$$

   If this value is positive, the satellite is located between the Sun and the Earth, so the satellite is not in the eclipse. However, if the value is negative, we need to check if the satellite is located in the cylindrical shadow of the Earth as in the Fig. 3.5. To check this relation, the norm of the cross product, c, between

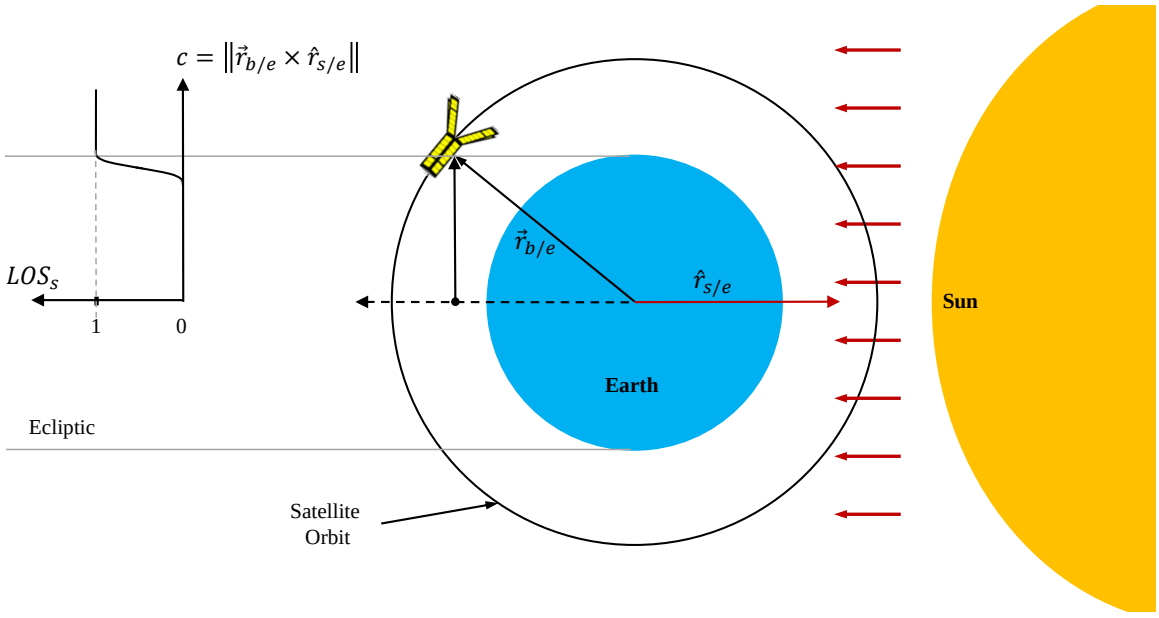

Figure 3.5: The relation between the Sun line-of-sight variable and orbital configuration.

the same vectors is required,

$$c = \left\|\vec{r}_{b/e} \times \hat{r}_{s/e}\right\|_2. \tag{3.7}$$

If $d < 0$, and c is greater than the Earth's radius, R_e, we can assume that the satellite is receiving sunlight. The line-of-sight to the Sun, LOS_s, is 0 if the satellite is in the eclipse and 1 otherwise. To convert this binary function to a continuous one, the penumbra area which smoothly transitions to zero is assumed. The penumbra area is very small in the Lower Earth Orbit (LEO), but it is exaggerated to avoid numerical difficulties in solving the optimization problem. A cubic function is constructed between $c = \alpha R_e$ and $c = R_e$ and the value of α represents how smooth our transition function is. For this analysis, the value of α is set to 0.9. The entire procedure used to compute LOS_s is

illustrated in Fig. 3.5 and the equations are as follows.

$$\eta = \frac{c - \alpha R_e}{R_e - \alpha R_e}, \tag{3.8}$$

$$LOS_s = \left\{ \begin{array}{c} 1, d > 0 \\ 1, c > R_e \\ 3\eta^2 - 2\eta^3, \alpha R_e < c < R_e \\ 0, c < \alpha R_e \end{array} \right\}. \tag{3.9}$$

The proposed technique make LOS_s variable continuous and differentiable and this model can be justified by physical characteristics of a light such as diffraction and refraction. As we can experience from the sunset on the beach, the satellite also enters the eclipse region with some transition.

3.3.2 Attitude Dynamics

Based on the payload requirements and its mounting direction we can define intermediate frame that we will refer to here as the rolled body-fixed frame, denoted by R. The axes of the rolled body-fixed frame are denoted $\hat{i}_R$, $\hat{j}_R$, and $\hat{k}_R$. Orientation matrices are represented with the letter O, and $O_{R/I}$ represents the rotation from the Earth-centered inertial frame to the rolled body-fixed frame,

$$\hat{k}_R = -\hat{v}_{b/e}, \ \hat{j}_R = \hat{r}_{b/e}, \text{ and } \ \hat{i}_R = \hat{j}_R \times \hat{k}_R, \tag{3.10}$$

$$O_{R/I} = \left[\begin{array}{ccc} \hat{i}_R & \hat{j}_R & \hat{k}_R \end{array} \right]^T. \tag{3.11}$$

Here, note that the direction of the vector $\hat{j}_R$ is defined to be parallel to the Earth-to-body vector. This intermediate frame is the one that results from rotating the inertial frame to ensure that the $-\hat{k}_B$direction is parallel to CADRE's velocity vector, and a second rotation implements the roll design variable γ. The rotation matrix for the

rolled frame to body-fixed frame is defined as

$$O_{B/R} = \begin{bmatrix} \cos\gamma & \sin\gamma & 0 \\ -\sin\gamma & \cos\gamma & 0 \\ 0 & 0 & 1 \end{bmatrix}. \tag{3.12}$$

Using these matrices, we can calculate $O_{B/I}$ and, the angular velocity,

$$-\vec{\omega}_B^{\times} = \dot{O}_{B/I} {O_{B/I}}^T, \tag{3.13}$$

where $\dot{O}_{B/I}$ is computed using the center difference formula. Then we can calculate the total angular momentum as

$$\vec{L} = J_B\vec{\omega}_B + J_{RW}\vec{\omega}_{RW},$$

where the subscript RW means the value is related to the reaction wheel. By applying derivatives, the following relation is obtained,

$$\dot{\vec{L}} = J_B\dot{\vec{\omega}}_B + \vec{\omega}_B \times J_B\vec{\omega}_B + J_{RW}\dot{\vec{\omega}}_{RW} + \vec{\omega}_B \times J_{RW}\vec{\omega}_{RW} = 0. \tag{3.14}$$

From Eq. (3.14), the Euler's equations can be derived in terms of the reaction wheel's angular velocity and torque, i.e.,

$$\begin{aligned} \vec{\tau}_{RW} &= J_B\dot{\vec{\omega}}_B + \vec{\omega}_B \times J_B\vec{\omega}_B, \\ \dot{\vec{\omega}}_{RW} &= -{J_{RW}}^{-1}\left[\vec{\tau}_{RW} + \vec{\omega}_B \times J_{RW}\vec{\omega}_{RW}\right], \\ \vec{\tau}_m &= -\vec{\tau}_{RW} - \vec{\omega}_B \times J_{RW}\vec{\omega}_{RW}. \end{aligned} \tag{3.15}$$

From Eq. (3.15), by selecting the design variable γ, we can calculate the required torques and the rotating speed of the reaction wheel assembly. Here, the mass moment

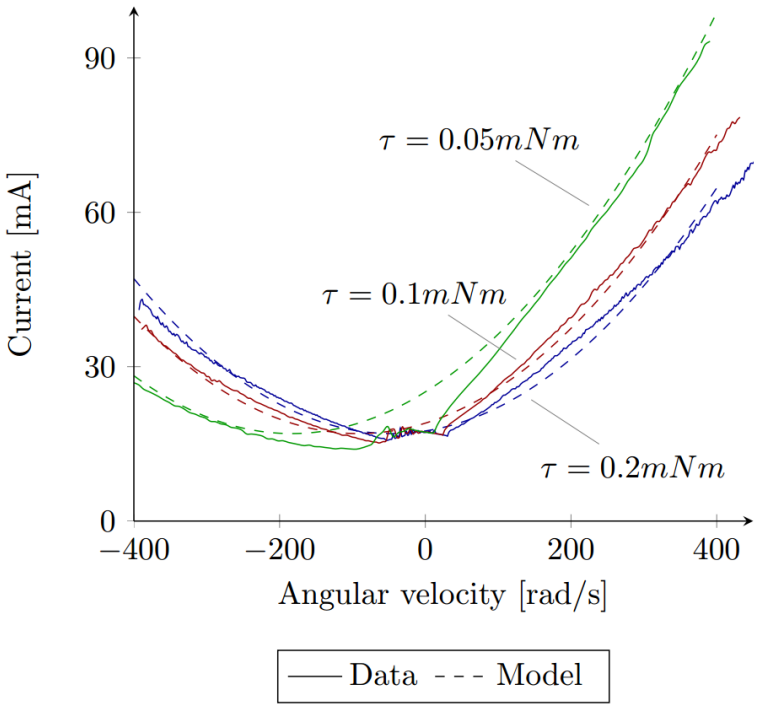

Figure 3.6: Reaction-wheel model compared with manufacturer-provided data for three torques [4].

of inertia matrices for the satellite and reaction wheels are given respectively,

$$J_B = \text{diag}\begin{bmatrix} 0.018 & 0.018 & 0.006 \end{bmatrix} \text{kgm}^2,$$

$$J_{RW} = \text{diag}\begin{bmatrix} 28 & 28 & 28 \end{bmatrix} \times 10^{-6} \text{kgm}^2.$$

An equation for the reaction wheel's current draw is constructed in terms of its angular velocity and required torque as in

$$I = (a\omega + b\tau)^2 + I_0, \tag{3.16}$$

where the values of a, b, and I_0 are presented in Table 3.1. The related parameters are estimated based on the manufacturer's data, which are presented in Fig. 3.6. For the power calculation, the 4V constant voltage is assumed for the reaction wheel

motor.

3.3.3 Photovoltaic Power System

3.3.3.1 Photovoltaic cell illumination

CADRE is assumed to have 12 photovoltaic arrays with 7 cells in each array. For the detailed panel and cell configuration, see Fig. 2.5 and Fig. 3.1. The photovoltaic cell illumination is based on the model explained in Chapter II and computed using OpenGL and a CAD model of the geometry. However, this model is discontinuous and difficult to incorporate into the framework developed by Hwang et al. [2]. Thus, data is processed with the B-spline multi-dimensional interpolant to approximate the illuminated areas in terms of the three parameters such as the azimuth, the elevation of the Sun, and the deployable panel angle. The cell illumination information is used to simulate the photovoltaic power generation and the thermal status of the deployable and the body panels of the satellite.

3.3.3.2 Photovoltaic cell power generation

One photovoltaic array is assumed to be constructed with the 7 cells which are connected in series, so their output voltages are added to compute the total voltage from the array. Each cell has a unique I-V curve which depends on its exposed area and temperature. The I-V curve model includes the cell illumination and the temperature as parameter and their relation in given by [60],

$$\begin{aligned} I &= I_{sc} - I_{sat}\left[\exp\left\{\frac{V+R_sI}{V_T}\right\}-1\right] - \frac{V+R_sI}{R_{sh}}, \\ I_{sc} &= LOS_s\frac{A_{exp}}{A_T}I_{sc_0}, \\ V_T &= \frac{nkT}{q}. \end{aligned} \tag{3.17}$$

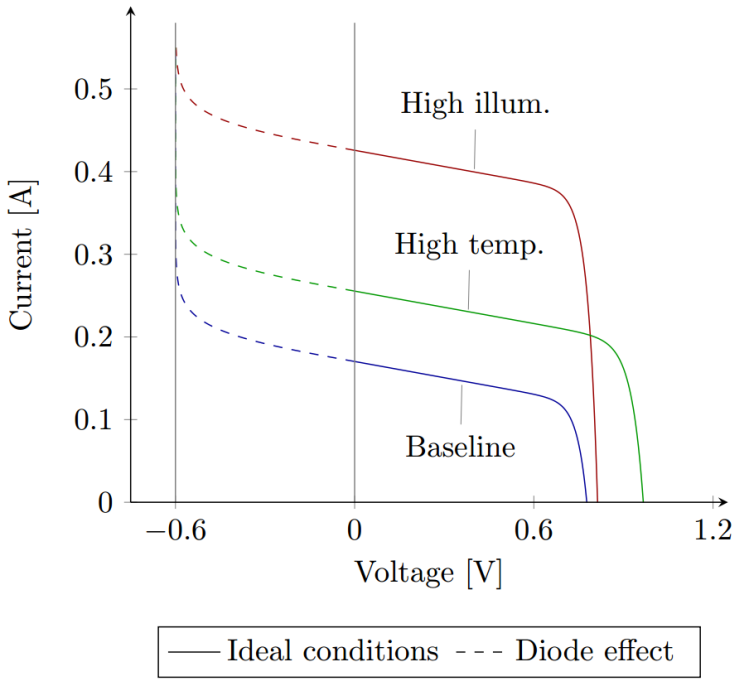

Figure 3.7: I-V curve of the photovoltaic cell with bypass diode assumption [4].

Here I_{sc_0} is the short-circuit current assuming full exposure of the cell, n is the ideality factor, k is the Boltzmann constant, q is the charge of an electron, I_{sat} is the saturation current, R_s is the series resistance, R_{sh} is the shunt resistance, A_T is the total area of cell, and A_{exp} is the exposed area to the Sun. R_s is assumed to be small and neglected and the bypass diode is assumed to be installed on each cell. Then we can derive piece-wise function for voltage versus current relation,

$$\begin{aligned} I_{sc} - I_{sat}\left[\exp\left(\frac{V}{V_T}\right) - 1\right] - \frac{V}{R_{sh}} - I = 0, I \leqslant I_{sc}, \\ V(I) = V_0 \tanh\left[\frac{-V_T R_{sh}}{V_0\left(I_{sat}R_{sh} + V_T\right)}\left(I - I_{sc}\right)\right], I > I_{sc}. \end{aligned} \tag{3.18}$$

The bypass diode affects when the array has partial shadow and, by adding the voltage output of the each model, we can imitate the partial shadow effects on the array.

3.3.4 Battery

This discipline estimates the State Of Charge (SOC) of the battery, which can be computed by integrating the following equation.

$$\dot{SOC} = \frac{P_{bat}}{V_{bat}Q},$$

where Q is the nominal discharge capacity of the battery, P_{bat} is the input power at any given time instant to the battery, and V_{bat} is the voltage output of the battery. We can compute the power at any given time instant as,

$$P_{bat} = P_{sol} - P_{RW} - P_{comm} - P_0. \tag{3.19}$$

Here, the battery power is assumed to be the sum of all loads. P_{sol} is the generated power by photovoltaic cell arrays, P_{RW} is the consumed power that is used by the reaction wheel assembly, P_{comm} is the consumed power that is used by communication subsystem, and P_0 is a 2-W constant power that is used by the scientific instruments and actuator to counteract the disturbance torques. The SOC of the battery increases as power is sent to the battery from the photovoltaic arrays and decreases as power is extracted from the battery. The battery voltage output based on SOC is modeled as,

$$V_{bat}\left(SOC\right) = \left(3 + \frac{e^{SOC} - 1}{e - 1}\right)\left(2 - e^{\lambda\frac{T - T_0}{T_0}}\right). \tag{3.20}$$

This equation differs from the data provided by the manufacturer as shown in Fig. 3.8. However, the major difference is restricted to the low SOC range of the battery that can be avoided by the optimizer by imposing appropriate constraints thereby maintaining the solution within the model validity range.

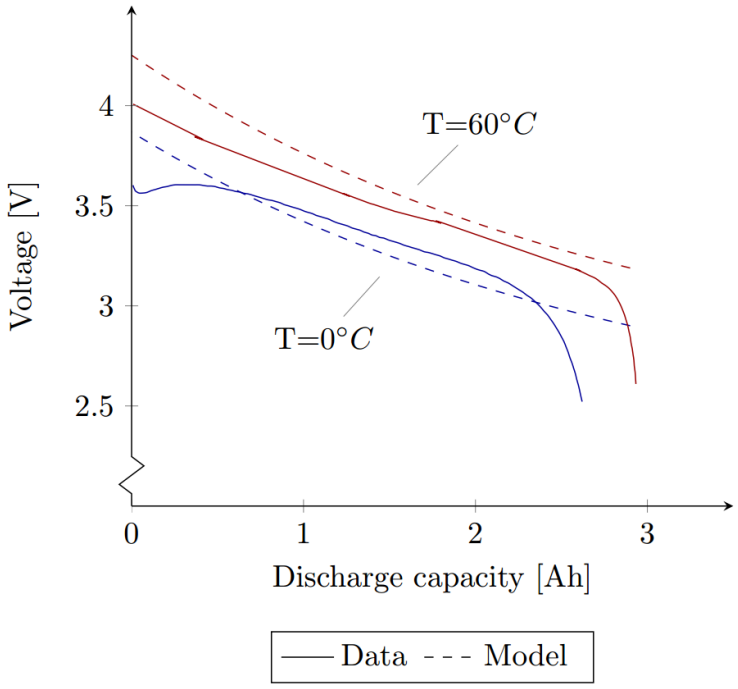

Figure 3.8: Battery-discharge curve model compared with manufacturers data at two temperatures [4].

3.3.5 Thermal

Thermal modeling is coupled with the efficiency of the photovoltaic power system, the battery output voltage, and even with the satellite attitude operation. By rotating the satellite relative to the Sun, the illuminated cell area is changed and the total energy influx is also affected. If the satellite temperature can be manipulated with the roll angle operation, the photovoltaic array can generate more power without excessive heating. The temperature within four deployable panels or the body block is assumed to be uniform. To calculate the thermal flux of each block, both heating and radiation from each of the 84 cells are considered and the Stefan-Boltzmann law

is applied. The nonlinear ODE of thermal model is as followings,

$$\begin{aligned}
\dot{T} &= \frac{\dot{Q}_{in} - \dot{Q}_{out} + \dot{Q}_{comm}}{m \cdot c_v}, \\
\dot{Q}_{in} &= \alpha q_{sol} A_{\exp} LOS_s, \\
\dot{Q}_{out} &= \varepsilon \left(\frac{2\pi^5 k^4}{15 c^2 h^3} \right) T^4 A_T, \\
\dot{Q}_{comm} &= (1 - \eta_p) P_{comm},
\end{aligned} \tag{3.21}$$

where m is the mass of the cell, c_v is the specific heat capacity, α is the absorptivity, ε is the emissivity of the cell, k is the Boltzmann constant, h is Planck's constant, c is the speed of light, A_T is the total area of the cell, and A_{exp} is the exposed area for the cell. During the communication process, we assumed that power amplifies data transmission with an efficiency but remaining power is dissipated as heat. Based on this assumption, η_p is assumed as 20% and $\dot{Q}_{comm}$ is calculated.

In some cases, installing a radiator can generate more power than installing the cells, due to the temperature characteristic of the photovoltaic array.

To add this to the optimization problem without adding a discrete variable, we linearly interpolate the cell and radiator properties and allow the optimizer the choose any $\xi \in [0,\ 1]$ where $\xi = 0$ is a radiator, $\xi = 1$ is a cell, and intermediate values represent some weighted average of the two.

3.3.6 Communication

To estimate the downloaded data amount, the data bit rate and the connection time need to be calculated. If the data bit rate is getting larger, we can download more data but, to increase this rate, more power or more antenna gain or less distance to the ground station is required. We can also achieve the larger data bit rate by decreasing signal-to-noise ratio (SNR) of the system but this change may make the radio connection to the ground station unstable. Thus, SNR is fixed to a minimum

acceptable value to maintain a secure connection and we use other variables as our design parameters. The power can be a design variable and the roll angle operation can also be a design variable because rotating the satellite to the ground station (GS) direction can increase the antenna gain. Here is the equation for the data bit rate,

$$B_r = \frac{c^2 G_r L_l}{16\pi^2 f^2 k T_s \left(SNR\right)} \frac{\eta_p P_{comm} G_t}{S^2} LOS_c.$$

Here, c is the speed of light, G_r is a constant representing receiver gain, L_l is a system line loss factor, f is the frequency, k is the Boltzmann constant, T_s is the system noise temperature, P_{comm} is the power used to amplify the signal, G_t is the satellite antenna transmitter gain, and S is the distance between the ground station and the satellite, respectively. The same η_p value used in the thermal discipline is also implemented here. The LOS_c variable is computed based on the dot product between the normalized Earth-to-ground station vector and the Earth-to-body vector in the inertial frame. The discontinuous function is smoothed, in this case by assuming that the line-of-sight (LOS) variable gradually increases as the satellite comes over the horizon. This is illustrated in Fig. 3.9.

To deploy a more realistic G_t, the antenna gain pattern analysis needs to be done with Ansys-HFSS$^{\text{TM}}$. This tool supports antenna design with 3D far field gain plot as in Fig. 3.10.

3.4 Optimization

3.4.1 Approach to MDO Problem

To solve the CADRE MDO problem, we need to consider many technical challenges. In this dissertation, to solve each of the technical challenges of the large-scale MDO problem, we have adopted the following approach developed by Hwang et al. [2, 4]. First, to handle the large number of design variables, gradient-based optimiza-

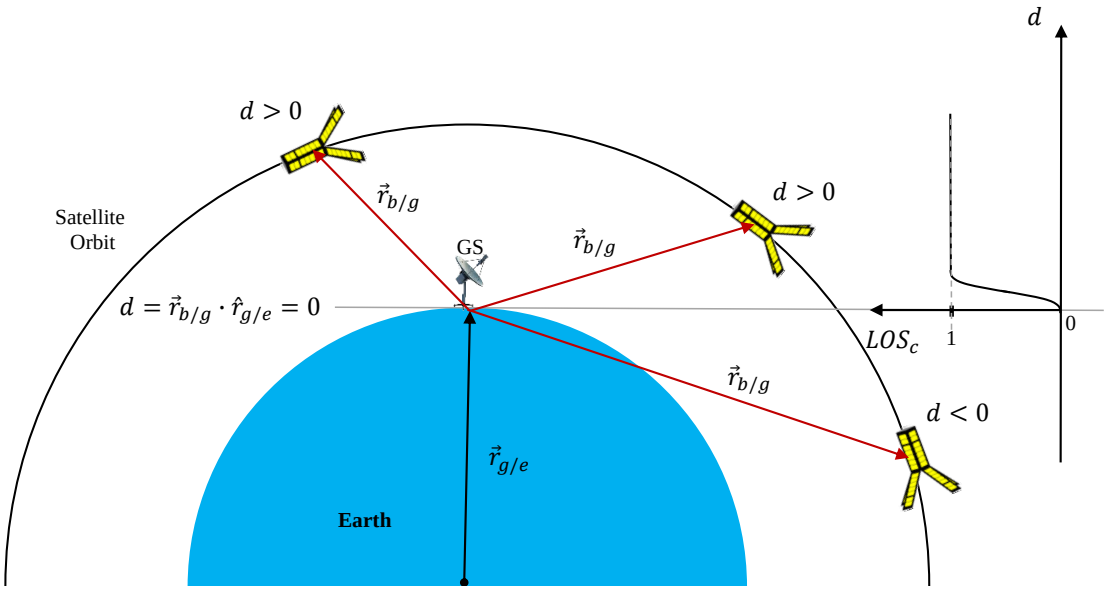

Figure 3.9: Illustration of the communication line-of-sight variable.

tion is adopted, because the gradient-free optimizers such as GA and PSO cannot find the solution of the problems with hundreds or thousands of design variables [61]. By applying an adjoint method for computing derivatives, the gradient-based optimization can search the solution to the large-scale MDO problem at a cost that is almost independent of the number of design variables [57]. As a solver, SNOPT [62] with the pyOpt interface [61] is implemented due to the efficiency of SNOPT for large-scale, sparse nonlinear constrained problems.

Since our optimization has a large number of design variables, the adjoint derivative calculation method must be used, but it requires a linear solution for each constraint [2]. Moreover, the battery discipline requires four inequality constraints at each time instance maximum charge rate, maximum discharge rate, minimum state of charge, and maximum state of charge-resulting in tens of thousands of constraints [4]. To reduce the number of constraints, the Kreisselmeier-Steinhauser (KS) function [63] aggregates the constraints over all the time instances into a single criterion. Constraint aggregation with KS functions has been shown to work well in combination

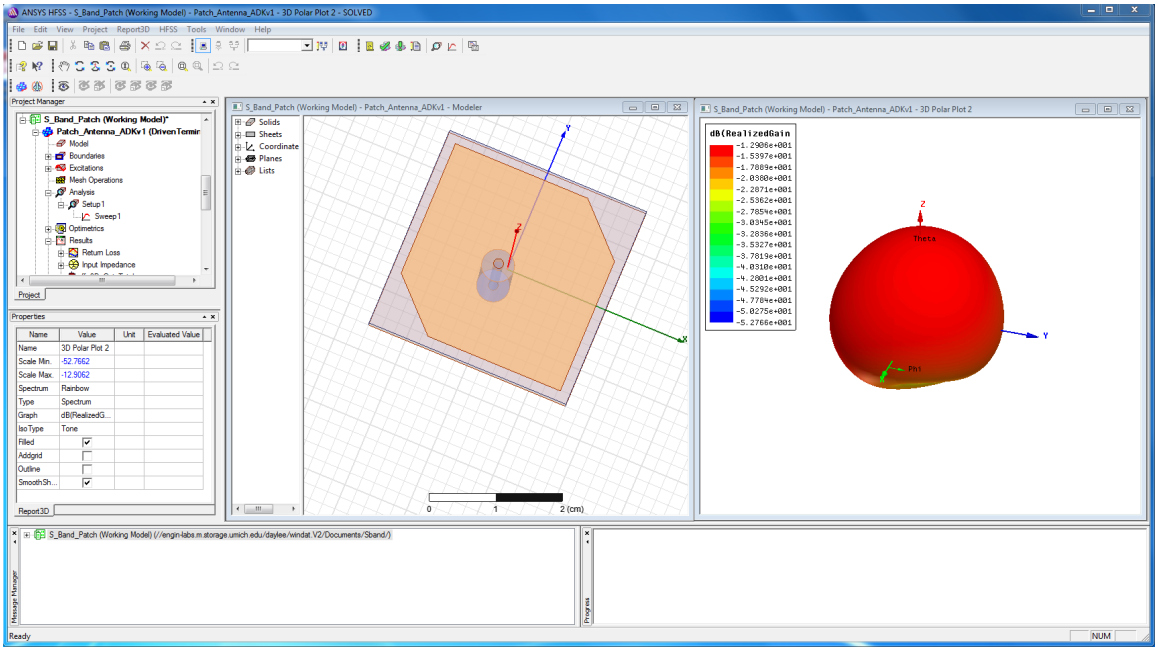

Figure 3.10: The antenna design and gain pattern acquired with Ansys-HFSS^{TM}.

with the adjoint method in optimization problems [64, 65, 66]. The KS function is given by

$$KS\left(x\right) = f_{i_{\max}}\left(x\right) + \frac{1}{\rho}\ln\sum_{i} e^{\rho\left(f_i(x) - f_{i_{\max}}(x)\right)}, \tag{3.22}$$

where f_i is the ith function in the vector of functions we wish to aggregate, i_{max} is the index of the function with the largest value at x, and ρ is a parameter that is problem-dependent. The optimization problems solved in this chapter use $\rho = 50$, a value that was found through numerical tests.

Another difficulty that the CADRE MDO problem includes is that each discipline has a different time scale. For example, CADRE's power and communication system simulation requires a time-resolution of a minute over at least 12 hours of the satellite's operation. However, orbit simulations require a one year simulation to model the orbit perturbation and the Sun elevation. To capture the characteristics of all disciplines, we need to run a long simulation with a short time-resolution which also increases the operation variables. Thus, the simulation time resolution is set to six 12-hour blocks

and distributed uniformly over the year. The orbit and communication characteristics are captured within the 12-hour blocks, and the orbit characteristics are captured by simulating half a day every two months.

3.4.2 Optimization Problems

As introduced in the previous section, to include the characteristics of a whole year, 6 days are selected bimonthly and a 12-hour simulation is performed on each day. Thus, constraints such as the battery charge rate, discharge rate, and minimum and maximum SOC are separately applied for each of the 6 days and the equality of the SOC is applied at the beginning and end of each 12-hour simulation. Various types of the variables are included in the problem. For example, deployable panel angle and antenna angle can be handled with scalar variables, installation of a cell or a radiator can be handled with 84 binary variables, and the roll angle variations, photovoltaic regulator setpoint current, and communication power can be treated as profile variables over time. Each profile variable is discretized with the number of points used in the time integration (1500 points), which are represented using fourth-order B-splines with 300 control points. The optimization problem is summarized in Table 3.1 and solved with SNOPT [62].

3.4.3 Optimization Results

To evaluate the effectiveness of the optimization, three different optimization problems are solved. The first is a baseline optimization that is the same as the original optimization problem in Table 3.1 except the deployable angle, antenna angle, and attitude roll profile. The second optimization includes the deployable panel and antenna angles which affect the satellite geometry. The third optimization adds both the geometric design and attitude operation variables to the baseline optimization of Table 3.1.

Table 3.1: Discipline model parameters [4].

Orbit Dynamics		
Gravitational parameter	μ	398600.44 km^3s^{-2}
Earth's radius	R_e	6378.137 km
Orbit perturbation coefficients	J_2	1.08264×10^{-3}
	J_3	-2.51×10^{-6}
	J_4	-1.60×10^{-6}
Attitude Dynamics		
Model coefficients	a	4.9×10^{-4} $\text{A}^{1/2}\text{s/rad}$
	b	4.5×10^2 $\text{A}^{1/2}/(\text{Nm})$
	I_0	0.017 A
Temperature		
Mass	m	0.4 (fin), 2.0 (body) kg
Specific heat capacity	c_v	0.6 (fin), 2.0 (body) kJ/kg K
Absorptivity	α	0.9 (cell), 0.2 (radiator)
Emissivity	ε	0.87 (cell), 0.88 (radiator)
Boltzmann constant	k	$1.3806488 \times 10^{-23}$ $\text{m}^2\text{kg}/(\text{s}^2\text{K})$
Speed of light	c	2.99792458×10^8 m/s
Plancks constant	h	$6.62606957 \times 10^{34}$ $\text{m}^2\text{kg/s}$
Total cell area	A_T	2.66×10^{-3} m^2
Solar constant	q_{sol}	1.36×10^3 W/m^2
Communication efficiency	η_P	0.2
photovoltaic Power		
Diode voltage	V_0	-0.6 V
Max. short-circuit current	I_{sc_0}	0.453 A
Saturation current	I_{sat}	2.809×10^{-12} A
Diode factor	n	1.35 V
Charge of an electron	q	$1.60217657 \times 10^{19}$ C
Shunt resistance	R_{sh}	40 Ω
Energy Storage		
Nominal capacity	Q	2900 mAh
Temperature decay coeff.	λ	$\ln(1/(1.1)^5)$
Reference temperature	T_0	293 K
Max. discharge rate	I_{min}	-10 A
Max. charge rate	I_{max}	5 A
Communication		
Receiver gain	G_r	12.9 dB
Line loss factor	L_l	-2.0 dB
Transmission frequency	f	437 MHz
System noise temperature	T_s	500 K
Minimum acceptable SNR	SNR	5.0 dB

Table 3.2: Optimization problem configuration [4].

	Variable/function	Description	Quantity
maximize	$\sum_{i=1}^{6} D_i$	Data downloaded	
with respect to	$0 \leq I_{setpt} \leq 0.4$	photovoltaic panel current	$300 \times 12 \times 6$
	$0 \leq \gamma \leq \pi/2$	Roll-angle profile	300×6
	$0 \leq P_{comm} \leq 25$	Communication power	300×6
	$0 \leq \text{cellInstd} \leq 1$	Cell vs. radiator	84
	$0 \leq \text{panelAngle} \leq \pi/2$	Panel angle	1
	$0 \leq \text{antAngle} \leq \pi$	Antenna angle	1
	$0.2 \leq SOC_i \leq 1$	Initial state of charge	6
		Total design variables number	25292
subject to Ib	$I_{bat} - 5 \leq 0$	Battery charge	6
	$-10 - I_{bat} \leq 0$	Battery discharge	6
	$0.2 - SOC \leq 0$	Battery capacity	6
	$SOC - 1 \leq 0$	Battery capacity	6
	$SOC_f - SOC_i = 0$	SOC periodicity	6
		Total constraints number	30

Table 3.3: Optimal design result for three problems [4].

	Panel angle	Antenna angle	Data download
Baseline optimization	45°	0°	2122 Gb/yr
Geometry optimization	63.8°	−45°	2991 Gb/yr
Geometry with attitude optimization	64.4°	−45°	3758 Gb/yr

The results in Table 3.3 suggest that the geometric design optimization can increase the data download amount by around 40%. In addition, they also suggest that including attitude operation in the optimization problem can yield an additional 40% by the data download increase. For all the problems, the optimizer chooses to install the solar cell instead of the radiator for all 84 cells.

Fig. 3.11 shows how the developed MDO affects the downloaded data increase and their distribution every 2 months. Fig. 3.12 and 3.13 shows the overall optimization results with the comparison of the three optimization problems. The following analysis is based on the first and the second row of Fig. 3.12. All months show that the geometry optimization with attitude operation provide more downloaded data than

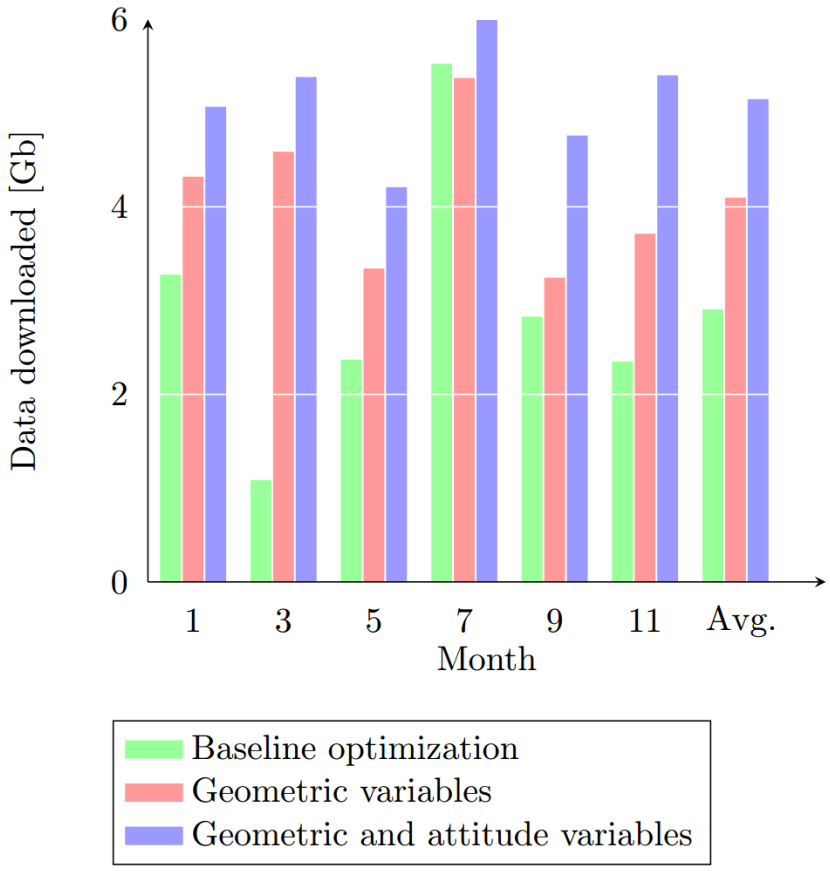

Figure 3.11: Division of total data downloaded over the six simulations for the three optimization problems [4].

the baseline optimization. However, the baseline optimization sometimes has a larger downloaded data than the geometry optimization without attitude operation and it can be shown in month 7. This indicate that the fixed roll angle optimization cannot always guarantee the maximization of the download data due to the long mission lifetime and its orbit variation. The month 3, 9 and 11 plots show, with attitude operation, the satellite can be connected with the ground station even at a pass that cannot be connected when we do not use the attitude operation. We can see the baseline optimization has no connection with GS at the first GS *LOS*, but other optimization cases have connected with GS (note the green color line). The month 9 plots shows the attitude operation could be very effective if the specific orbital condi-

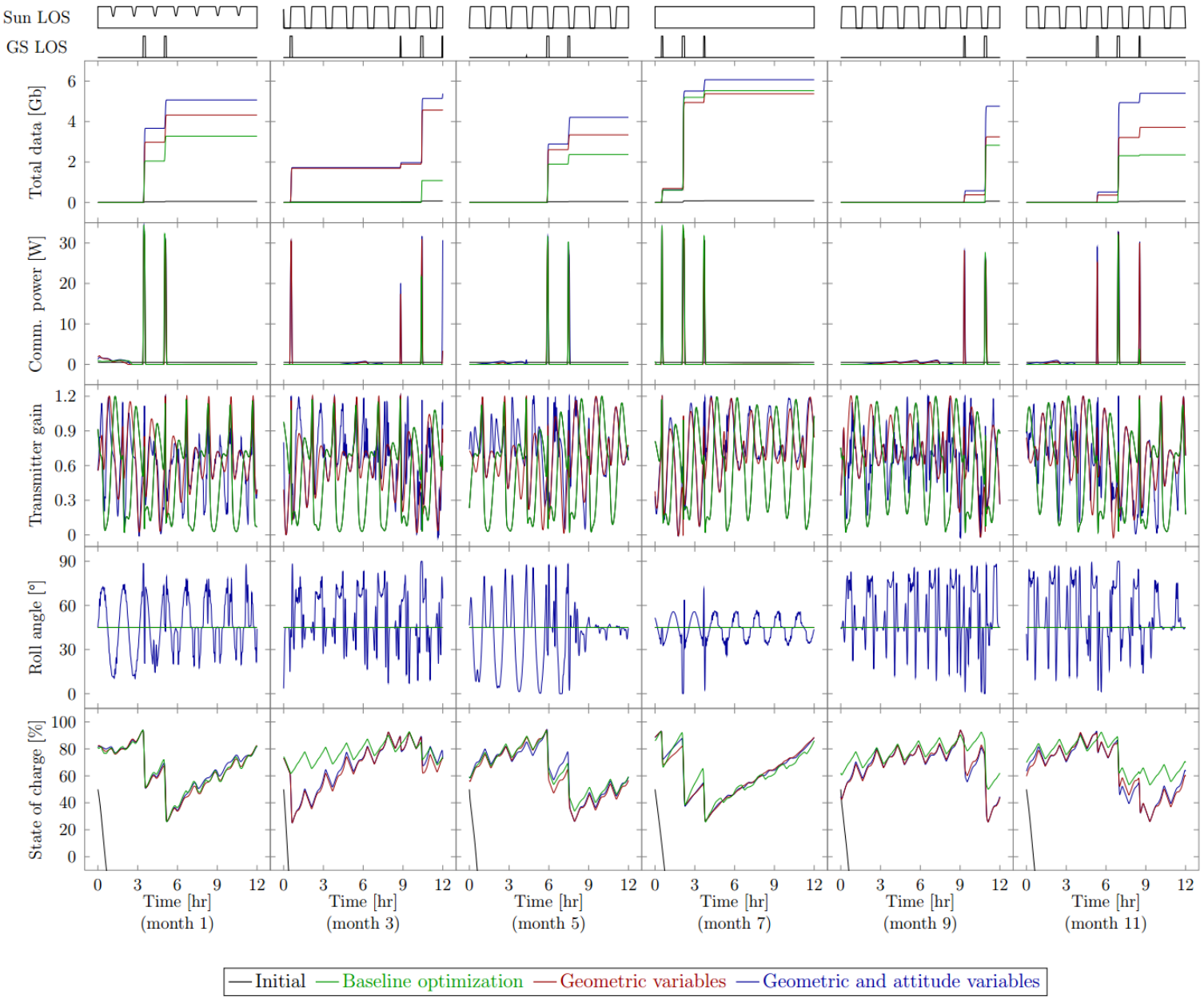

Figure 3.12: Initial and optimized profiles of the three optimization problems #1 [4].

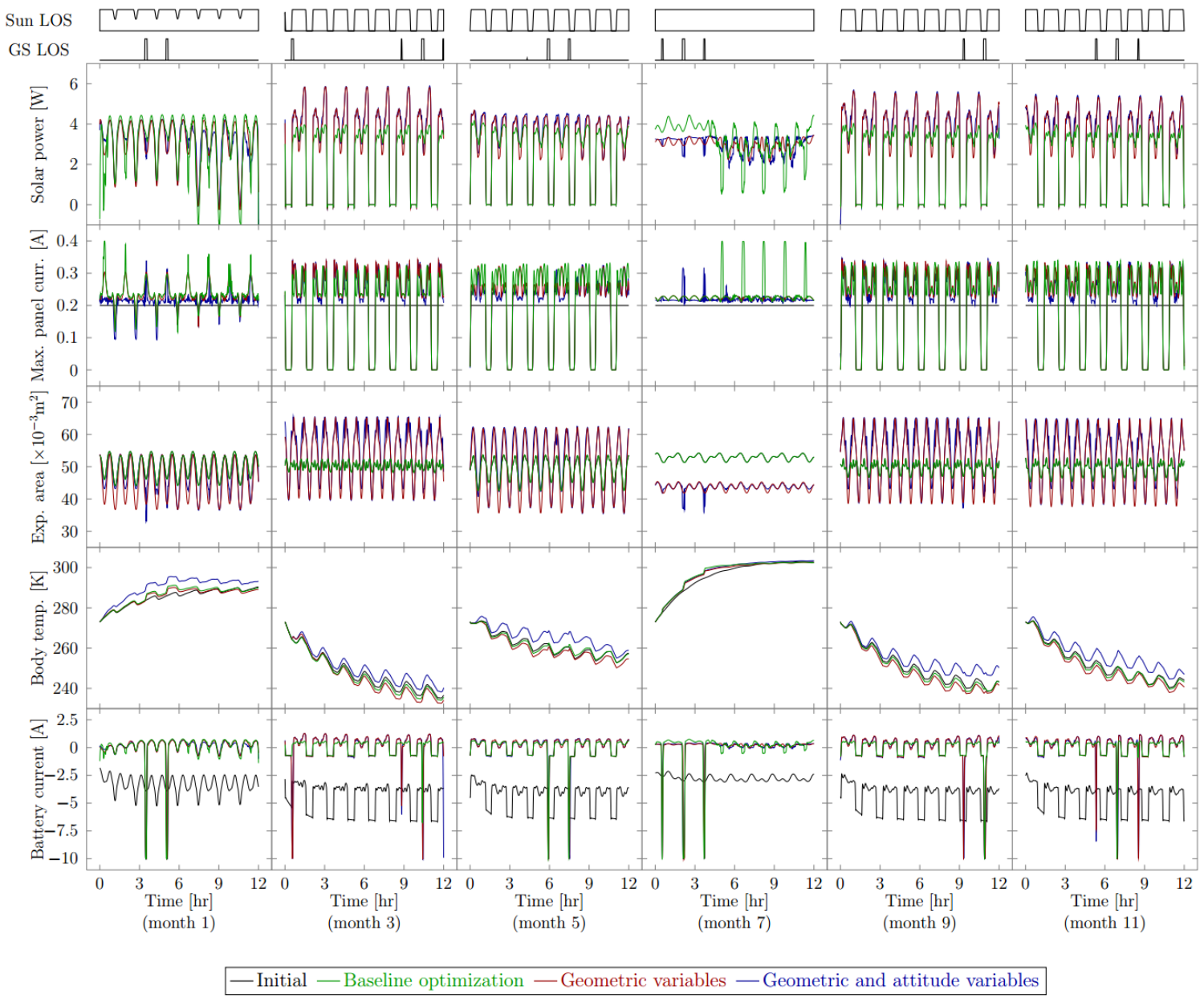

Figure 3.13: Initial and optimized profiles of the three optimization problems #2 [4].

tion is satisfied. See the download difference between the geometry only optimization and geometry and attitude operation optimization.

The communication power plots show that the optimizer allocates power to the transmitter only during the ground-station passes, as expected, but the peaks of the spikes are limited by the available SOC and the discharge constraint. The SOC plots show that the additional power generated by the optimization is used for a gradual build-up of energy between data transmissions, enabling short and rapid power discharges for high-bit-rate data transmissions.

In Fig. 3.13, from the total power graph of the first row, we can see the larger increase from the baseline optimization to the geometry optimization but a rather smaller increase from the geometry optimization to the geometry and attitude operation optimization. The second row of Fig. 3.13 shows that the geometry and attitude operation optimization has a smaller variation in the generated current plot (especially on month 7) than the baseline optimization. This information indicates that the deployable angle has a suppressing effect on the variation and gives the satellite good exposure to the Sun, which can be also seen in the third row of graphs. However, on the attitude operation side, the optimizer is more focused on chasing the ground station instead of generating more power by chasing the Sun. The exposed area graph of month 7 clearly presents this interest of the optimizer.

In the fourth row, the body temperature looks weakly dependent on the attitude operation and it also has a small effect on the photovoltaic power generation.

The battery-current plots show that the communication power is limited by the battery-discharge constraint for many of the ground-station passes, while the remainder are energy-limited.

3.4.4 Discussion

The MDO results show that the optimized operations of the attitude and photovoltaic power system can improve the satellite performance. To apply the acquired optimization results in orbit, the data transfer from the ground to orbit must be performed with the radio communication. The proposed MDO results of the previous section only cover about 3 days (6×12 hours) of operation information for the spacecraft in orbit. Thus, the same size MDO problem must be solved and the solution uploaded to the satellite every 3 days. However, the data uploading can be hindered by the ground station's or satellite's status and the satellite memory storage often malfunctions due to the harsh space environment. To address these case, an operation controller, which executes the ground optimization results in orbit, is required. For the development of the operation controller, the MDO operation results must be analyzed and adopted in the controller. In this section, the attitude operation and the photovoltaic array setpoint operation are analyzed based on the optimization results of Fig. 3.12 and 3.13 and the development process for the operation controllers is proposed.

3.4.4.1 The characteristics of the attitude operation optimization results

Fig. 3.14 shows how the optimizer selects the operation variables when the ground station or the Sun appears in the satellite's LOS. As presented in the roll angle graph of Fig. 3.14, for the movement of the Sun, the satellite roll draws a sinusoidal curve. This sinusoidal motion indicates that the satellite tracks the Sun's movement with a specific angle. Similarly, if the ground station appears in the satellite's LOS, the optimizer stops tracking the Sun and makes the satellite antenna track the GS. These roll operation responses can be analyzed based on the relation with the objective function. Because the objective of the optimization is dominated by the downloaded data amount, the roll motion at the ① and ② of Fig. 3.14 shows the change of a

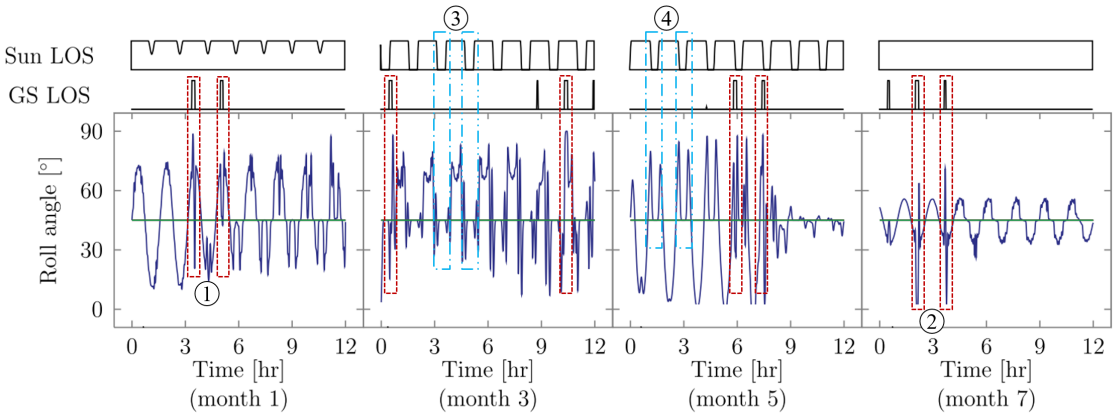

Figure 3.14: The attitude operation optimization effects on the communication [4].

tracking target.

The interesting point is, if the satellite goes into the eclipse, the optimizer rotates the satellite back to 0° roll angle, which is shown in the ③ and the ④ in Fig 3.14. This reaction looks related to the power consumption of the reaction wheel. By returning back to the original roll attitude, the angular momentum of RWA, which is elevated for the attitude change, is restored to its original angular momentum. The level of the angular momentum of RWA is connected to the required electric power of RWA and, by restoring the angular momentum, the power consumption is reduced.

Based on the analysis, several characteristics of the attitude operation optimization can be discovered. First, the satellite needs to roll to track the GS or the Sun. If both targets appear within the satellite's LOS, the GS tracking is prioritized. Second, if the GS and the Sun are located out of sight, the satellite needs to roll back to the parking attitude to reduce the angular momentum of RWA, which is related to the electric power consumption. By applying these rules to the attitude operation controller, we can make the satellite perform better in the orbit.

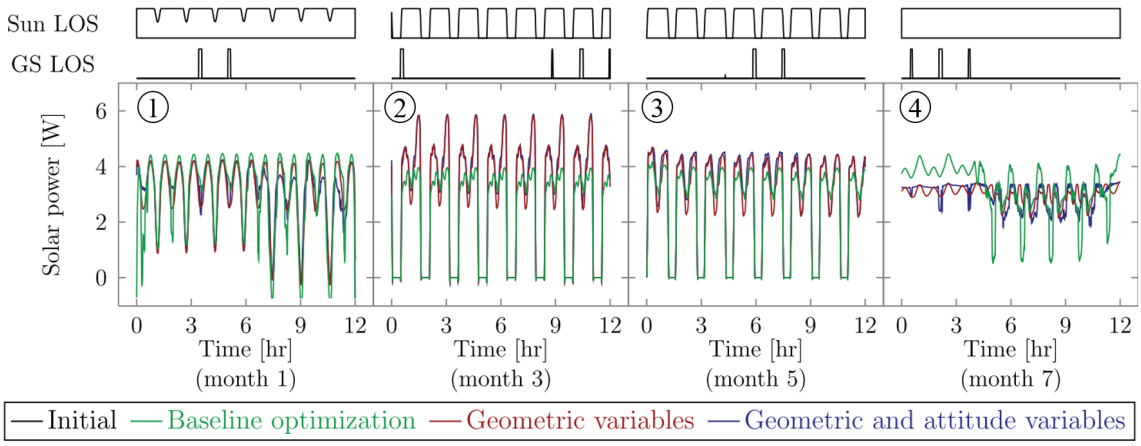

(a) With the setpoint operation optimization [4].

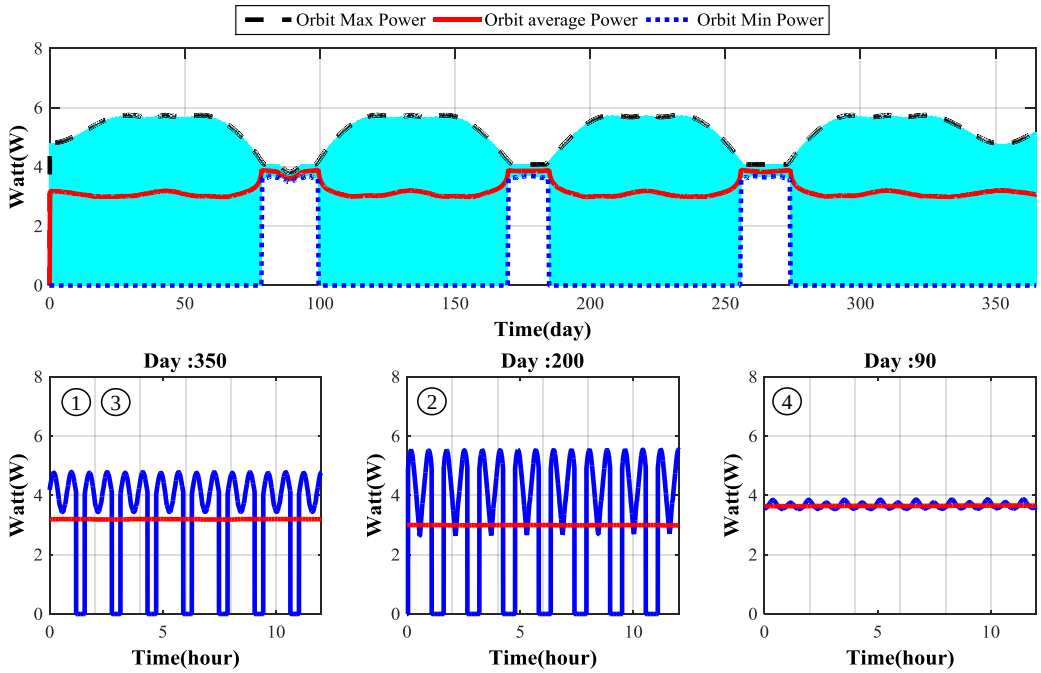

(b) With the peak power tracker assumption.

Figure 3.15: photovoltaic power generation plots.

3.4.4.2 The effectiveness of the photovoltaic array operation optimization

The power amount acquired from the photovoltaic array can be manipulated with the power regulator current setpoint. If the regulator draws too much current from the photovoltaic array with a higher current setpoint than required, the voltage drop-down happens on the photovoltaic array, which reduces the power generation amount of the photovoltaic array. Many peak power tracker algorithms that are used in the photovoltaic power regulator maximize the power generation amount by searching for proper current setpoint. In our MDO problem, we make the optimizer choose the current setpoint of each photovoltaic array regulator and the results are presented in Fig. 3.15(a). This optimization result can be compared with the peak power tracker results that are presented in Fig. 3.15(b). By comparing both graphs, we can see the optimized power generation is quite similar with the power generation with a peak power tracker. In particular, the power generation trend between the same circled numbers in Fig. 3.15 are very close with each other. For instance, the graphs with ① and ③ in Figs. 3.15(a) and 3.15(b) are almost identical. However, the ② and ④ in Figs. 3.15(a) and 3.15(b) are slightly different. The differences in the power operation optimization (Fig. 3.15(a)) are mostly caused by the additional disciplines of the MDO problem. For example, the ④ of Fig. 3.15(a) is different from the ④ of Fig. 3.15(b). The overall trend of the the ④ of Fig. 3.15(b) is quite flat but the trend of ④ of Fig. 3.15(a) is rather dynamic because the latter considers the battery discipline and power generation is limited when the battery is fully charged. When the power is exhausted by the communication with GS, more power is generated, which can confirm this trend in the first part of the ④ of Fig. 3.15(a). However, if the power is enough, the optimizer does not maximize the power generation and it can be seen in the latter half of the ④. The difference between the both ② of Fig. 3.15(a) and Fig. 3.15(b) might be related to the thermal discipline. If the photovoltaic array's temperature is lowered by passing the eclipse, the efficiency of

the array is also lowered and the power generation amount can be reduced. However, more exact analysis is left for future work.

From the comparison, we can assume that the photovoltaic array setpoint operation optimization is close with a peak power tracker operation. Thus, the MDO result can be guaranteed to work in orbit by installing the peak power tracker algorithm on each photovoltaic array regulator.

3.4.5 Convexity analysis on the attitude sphere

When the gradient-based optimization method is implemented, the convexity of the objective function needs to be considered to verify the locality of the optimization solution. In the proposed problem, the convexity of the objective function is not guaranteed due to following reasons.

- Some disciplines such as photovoltaic power generation and thermal (Eq. (3.17) and (3.21)) have high non-linearity.
- The photovoltaic cell illumination output based on the roll angle variation (Fig. 2.9) shows the existence of multiple local minima in the discipline.
- LOS time from the Ann Arbor ground station to the satellite for 1 year is mapped on the attitude sphere and presented in Fig. 3.16. The LOS time of Fig.3.16(a) is directly related with the objective function (the amount of the download data). The satellite roll angle parameters are the design variables of the problem and coupled with the azimuth value the graph. As we can see, local minima exist in 3.16 and the objective function is non-convex.

Thus, the global optimum is also not guaranteed but the local optimum is enough for the system design.

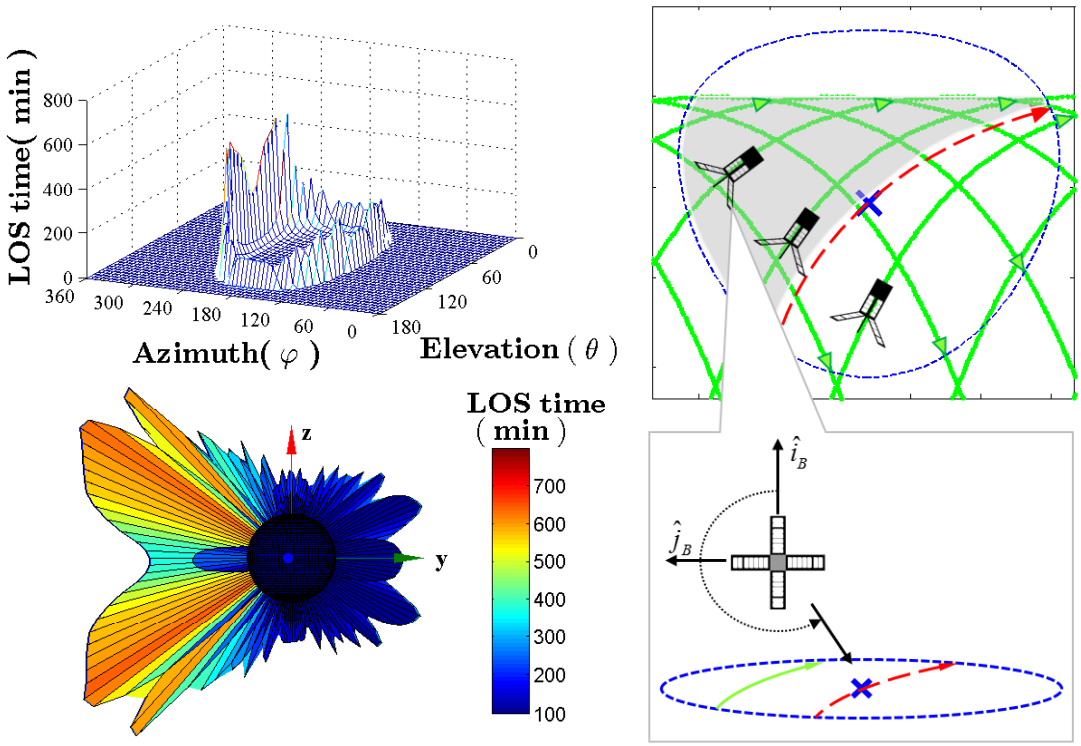

(a) LOS time mapping.

(b) Analysis Diagram.

Figure 3.16: GS LOS time mapping on the attitude sphere and Analysis Diagram (Ann Arbor, 1 year).

3.5 Conclusion

This chapter formulated and solved a large-scale MDO problem for the CADRE small satellite mission, which inclued the geometric design and the attitude and power operation of the mission. The problem was constructed with six disciplines, more than 35,000 design variables that represent 12 hours of the satellite's operation at six uniformly selected days over the year. To solve the problem, the MAUD framework[2, 4], which implements gradient-based optimization, was implemented and extended. During the effort, it was also found that changing the launch parameters changed the values of the objective function and the design variables, suggesting that this tool could be used to evaluate launch options and to optimize the design to a particular launch opportunity. We have demonstrated that considering all the major disciplines,

time scales, and design variables simultaneously for the small-satellite problem is feasible through a rigorous multidisciplinary approach. This approach provides a system-level perspective of the problem with sufficient depth to capture high-level trade-offs and reveal insights that are perhaps not obvious at the discipline level. The solution is divisible into a geometric solution that is useful for the ground development of the satellite and an operational solution to be implemented on-orbit.

While the ground-based design work is part of typical design efforts, the on-orbit constrained operation requires further research and development. The following chapter presents our work in this effort to provide a constraint-based controller for satellite operations.

CHAPTER IV

Computational Nonlinear Model Predictive Control on SO(3) for Spacecraft with Reaction Wheel Assembly

4.1 Introduction

In recent years, increasing demand for downsized and more agile spacecraft has led to a need for control techniques that ensure safe and reliable spacecraft operation at the limits of performance. These techniques must take system constraints into account while maximizing performance. One such technique is MPC [67], which solves a constrained optimization problem in order to obtain a stabilizing, constraint-admissible control law. When MPC is based on linear models, the optimization problem becomes a constrained quadratic programming problem, which can be solved quickly using processing power that is available on-board; for this reason, MPC based on linear models is often used when fast computations are desired. For examples of such an approach to spacecraft attitude control, see [68, 69, 70, 71, 72]. MPC based on nonlinear models is called NMPC. If the constrained system is nonlinear, then the use the nonlinear model in the NMPC scheme leads to more realistic predictions and, therefore, to potentially better performance over linear MPC. Since the NMPC optimization cannot be expressed as a quadratic programming problem, other methods

are needed in order to quickly solve for the NMPC control. In this work, we present an NMPC algorithm for use in constrained spacecraft attitude control.

Constrained spacecraft attitude control refers to the control of spacecraft attitude in the presence of state and control constraints, which include constraints on the actuation mechanisms, the spacecraft orientation, its angular velocity, etc. For instance, reaction wheels used as attitude control actuators in many spacecraft can generate limited torque and have maximum angular speed limits and the violation of actuator constraints can cause instability or the loss of pointing accuracy. Star trackers used for on-board attitude determination induce exclusion-zone constraints since star trackers cannot measure the spacecraft attitude when the Sun or the Earth is within the camera angle, and since long exposure to the Sun can damage the camera sensor. Various approaches to handle actuator constraints have been proposed in [73, 74, 75, 76], while exclusion-zone constraints have been treated in [77, 78, 79, 80, 81, 82]. For example, attitude control problems with exclusion-zone constraints were addressed in the framework of the open-loop attitude planning and commanding in [80, 82] and exploiting feedback control in [77, 81].

As stated previously, in this chapter we use an NMPC approach to enforce the above constraints. The NMPC scheme has previously been developed in [83] for spacecraft attitude, whose dynamics evolve on SO(3), and whose control inputs are external torques. The NMPC scheme from [83] is different from other NMPC approaches because the prediction model is obtained through the LGVI, an integration scheme that, unlike standard integration schemes such as Runge-Kutta, preserves conserved quantities of motion and therefore leads to a more accurate prediction model. The dynamics obtained via the LGVI evolve on Lie groups, of which SO(3) is an example. The NMPC approach of [83] uses the LGVI spacecraft attitude prediction model in order to enforce system constraints. Note that the work in [83] has been generalized to systems whose dynamics evolve on general matrix Lie groups. In [84], the authors

have developed a numerical solver for the NMPC problem of [83]. The solver is based on [85] and uses exterior penalty function for constraint handling. This paper is an extension of the approach in [84, 83] to the case of spacecraft with RWA.

With terminal set constraints, global closed-loop stability results have been obtained. The extension to spacecraft with RWA is significant as the ordinary RWA-free case is complicated by the need to consider reaction wheel speeds and the angular momentum exchange between the wheels and the spacecraft bus in the dynamic model of the spacecraft, and in formulating and solving NMPC problem numerically. Moreover, from a practical standpoint, the case of spacecraft with reaction wheels is important. Reaction wheels are used in many spacecraft and, unlike thrusters, reaction wheels can be used for precise pointing and attitude tracking while not consuming any fuel. The use of NMPC based on an LGVI model is pursued since, despite a potentially higher computational cost, it exploits a more realistic model model of the spacecraft dynamics which can provide an increased constrained domain of attraction. As in [84], the indirect single shooting method is applied to the nonlinear root finding problem resulting from the necessary conditions for optimality, which is warm-started from the solution at the previous time instant. Our implementation also exploits sensitivity derivative expressions obtained from the necessary conditions for optimality, derived using variational calculus techniques on Lie groups. The constraints are handled using an exterior penalty function based approach; such an implementation is advantageous to handle state-constraint infeasibility that may occur during real operation due to disturbances or model mismatch, and does not introduce extra variables that an implementation with slack variables may entail. While these approaches are similar to [84], modifications had to be made in the reaction wheel case to treat extra states due to reaction wheels. This chapter is organized as follows. In Section 4.2, discrete dynamics on SO(3) are introduced for the spacecraft. In Section 4.3, a nonlinear model predictive control problem is defined and converted to an optimal

control problem over a prediction horizon. The constraints are augmented to the cost using exterior penalty functions. In Section 4.4, we present our computational solver. To demonstrate the effectiveness of the proposed algorithm, simulation results are presented in Section 4.5. Our submitted conference paper [86] includes preliminary results. As compared to [86], this effort contains details and derivations not presented in [86], including the treatment of a practical spacecraft configuration with four reaction wheels. We also present the comparison of the MPC problem formulations and numerical solution procedure in the case of the spacecraft with RWA and spacecraft with external moments.

4.2 Discrete Dynamics of a Spacecraft on SO(3)

In this section, we present the discrete-time rigid body equations of motion for a satellite with and without a reaction wheel assembly. In both cases, the dynamics have been obtained by using the LGVI. The equations of motion for a spacecraft with external control moments, derived in [87], are given by,

$$R_{k+1} = R_k F_k, \tag{4.1a}$$

$$\Pi_{k+1} = F_k^T \Pi_k + h M_k + h u_k, \tag{4.1b}$$

$$h\Pi_k^{\times} = F_k J_d - J_d F_k. \tag{4.1c}$$

In the above, h is the sampling time; the matrices R_k and F_k are rotation matrices and elements of SO(3), where R_k is the spacecraft orientation and $F_k = R_{k+1}R_k^T$ is the difference in orientation between samples; $\Pi_k \in \mathbb{R}^3$ is the spacecraft total angular momentum and $M_k \in \mathbb{R}^3$ is the vector of external disturbances which result from gravity gradients, aerodynamic drag, solar pressure, etc.; $u_k \in \mathbb{R}^3$ is the control torque, which is used to stabilize the spacecraft attitude; the positive definite matrix J_d is the nonstandard moment of inertia matrix and is related to the standard inertia

matrix J by the equation,

$$J_d = \frac{1}{2}\,\mathrm{tr}(J) I_3 - J. \tag{4.2}$$

Next, we consider a spacecraft with RWA but without external control torques. A spacecraft with RWA controls its attitude by adjusting the angular velocity of its reaction wheels in order to induce a counter-rotation of the spacecraft. Accordingly, the LGVI equations of motion for a spacecraft with RWA differ from (4.1) because the actuation mechanisms apply a torque about the reaction wheels instead of applying a torque directly to the spacecraft. Following the derivations in [88], we obtain the following equations of motion,

$$R_{k+1} = R_k F_k, \tag{4.3a}$$

$$\Pi_{k+1} = F_k^T \Pi_k + h M_k, \tag{4.3b}$$

$$h\Pi_k^\times = F_k A_k - A_k^T F_k, \tag{4.3c}$$

which are similar to those in (4.1), along with equations of motion relating to the reaction wheel assembly,

$$A_k = J_d + \frac{1}{2}\sum_{i=1}^{n} (J_i \Delta\theta_{i,k} s_i)^\times, \tag{4.4a}$$

$$\pi_{i,k+1} = \pi_{i,k} + h\tau_{i,k}, \tag{4.4b}$$

$$h\pi_{i,k} = J_i \left(\Delta\theta_{i,k} - \frac{1}{2}\,\mathrm{tr}(F_k s_i^\times) \right). \tag{4.4c}$$

In the above, n is the number of reaction wheels in the spacecraft with i ranging from 1 to n. The scalar $\pi_{i,k}$ is the angular momentum of the i-th wheel about the s_i axis, where s_i is a unit vector with origin at the spacecraft center of mass; $\Delta\theta_{i,k}$ is the difference in rotation wheel position between samples; $\tau_{i,k}$ is the control torque applied to the i-th wheel; the parameter $J_i > 0$ is the moment of inertia of the i-th

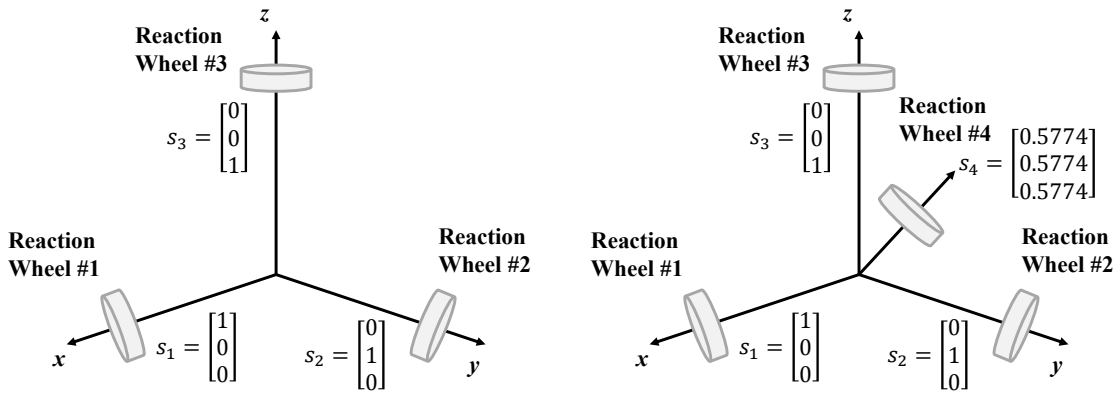

(a) RWA with 3 wheels

(b) RWA with 4 wheels

Figure 4.1: Two different RWA configurations and their spin axes

wheel's about its spin axis. For illustration, in Fig. 4.1(b) we provide two examples of RWAs with 3 and 4 reaction wheels.

4.3 Nonlinear Model Predictive Control Problem Formulation for a Spacecraft on SO(3)

In this section, we present an NPMC scheme for constrained control of the spacecraft dynamics, subject to the equations of motion in (4.1) or (4.3)-(4.4), which have been introduced in the previous section. The NMPC scheme is based on the NMPC framework introduced in [83, 89] and uses the computationally fast solver which is similar to the one presented in [84] for determining the control input.

For a spacecraft with external control torque, whose dynamics are given in (4.1), the controller determines the control input by solving the following optimization prob-

lem,

$$\min_{\{u_{j|k}\}_{j=0}^{N-1}} \mathcal{J}_d^1 = K_d^1(R_{N|k}, \Pi_{N|k}) + \sum_{k=0}^{N-1} C_d^1(R_{j|k}, \Pi_{j|k}, u_{j|k}), \tag{4.5a}$$

$$\text{subject to } h\Pi_{j|k}^{\times} = F_{j|k}J_d - J_d F_{j|k}^T, \tag{4.5b}$$

$$R_{j+1|k} = R_{j|k}F_{j|k}, \tag{4.5c}$$

$$\Pi_{j+1|k} = F_{j|k}^T \Pi_{j|k} + hM_{j|k} + hu_{j|k}, \tag{4.5d}$$

$$H_\ell^1(R_{j|k}, \Pi_{j|k}, u_{j|k}) \leq 0,\ \ell = 1, \ldots, m. \tag{4.5e}$$

In the above, the dynamics in (4.1) have been included as equality constraints. Other, inequality constraints have been introduced in (4.5e). These inequality constraints can include pointing, exclusion-zone constraints, constraints on the available torque, and so on. Note that m is the number of inequality constraints considered. In the NMPC law, the control input u_k to (4.1) is set to the first element of the control sequence $\{u_{j|k}^*\}_{j=0}^{N-1}$ solving (4.5), i.e.,

$$u_k = u_{0|k}^*. \tag{4.6}$$

As in [89], we assume that K_d and C_d are real-valued positive semi-definite cost functions with the property that $K_d^1(I_{3\times3}, 0_{3\times1}) = 0$ and $C_d^1(I_{3\times3}, 0_{3\times1}, 0_{3\times1}) = 0$, that $H_\ell^1(I_{3\times3}, 0_{3\times1}, 0_{3\times1}) < 0$, and that the functions H_ℓ^1 are sufficiently differentiable. We note that in [89], terminal conditions are imposed to guarantee recursive feasibility and stability. These constraints can, however, degrade closed-loop response and are not used in the present paper; instead the constraints are treated as soft, and we rely on simulation-based verification of stability properties.

For the dynamics (4.3)-(4.4) relating to a spacecraft with RWA, the NMPC opti-

mization problem is given by,

$$\min_{\{\tau_{j|k}\}_{j=0}^{N-1}} \mathcal{J}_d^2 = K_d^2(R_{N|k}, \Pi_{N|k}, \pi_{N|k}) + \sum_{k=0}^{N-1} C_d^2(R_{j|k}, \Pi_{j|k}, \pi_{j|k}, \tau_{j|k}), \tag{4.7a}$$

$$\text{subject to } h\Pi_{j|k}^{\times} = F_{j|k}A_{j|k} - A_{j|k}^T F_{j|k}^T, \tag{4.7b}$$

$$R_{j+1|k} = R_{j|k}F_{j|k}, \tag{4.7c}$$

$$\Pi_{j+1|k} = F_{j|k}^T \Pi_{j|k} + hM_{j|k}, \tag{4.7d}$$

$$\pi_{j+1|k} = \pi_{j|k} + h\tau_{j|k}, \tag{4.7e}$$

$$H_\ell^2(R_{j|k}, \Pi_{j|k}, \pi_{j|k}, \tau_{j|k}) \leq 0,\ \ell = 1, \ldots, m. \tag{4.7f}$$

The treatment of this optimization problem is analogous to that of (4.5), with the functions K_d^2, C_d^2, and H_ℓ^2 satisfying properties analogous to those of K_d^1, C_d^1, and H_ℓ^1, respectively.

In order to handle situations in which constraints may become infeasible, we relax (4.5e) and (4.7f) and treat them as soft. Then the numerical solution is based on the necessary conditions for optimality for augmented cost functionals of $\mathcal{J}_{d,a}^1$ and $\mathcal{J}_{d,a}^2$. The augmented cost functional corresponding to the cost functional $\mathcal{J}_{d,a}^1$ is given by,

$$\begin{aligned}\mathcal{J}_{d,a}^1 = K_d^1(R_N, \Pi_N) + \sum_{k=0}^{N-1} C_d^1(R_k, \Pi_k, u_k) + \sum_{k=0}^{N-1} \left\langle \lambda_k^1, (\log(R_k^{-1}R_{k+1}) - \log(F_k))^{-\times} \right\rangle \\ + \sum_{k=0}^{N-1} \left\langle \lambda_k^2, (\Pi_{k+1} - F_k^T\Pi_k - hM_k - hBu_k) \right\rangle + \sum_{k=0}^{N-1}\sum_{\ell=1}^{m} \mu_\ell \phi_\ell(H_\ell^1(R_k, \Pi_k, u_k)),\end{aligned} \tag{4.8}$$

where we have introduced the Lagrange multipliers λ_k^1, $\lambda_k^2 \in \mathbb{R}^3$, the exterior penalty functions ϕ_ℓ, $\ell = 1, \ldots, m$, and scalar weighting factors $\mu_\ell > 0$, $\ell = 1, \ldots, m$. The

augmented cost functional corresponding to $\mathcal{J}^2_{d,a}$ is given by,

$$\begin{aligned}\mathcal{J}^2_{d,a} &= K^2_d(R_N, \Pi_N, \pi_N) + \sum_{k=0}^{N-1} C^2_d(R_k, \Pi_k, \pi_k, \tau_k) \\ &+ \sum_{k=0}^{N-1} \left\langle \lambda^1_k, (\log(R_k^{-1}R_{k+1}) - \log(F_k))^{-\times} \right\rangle + \sum_{k=0}^{N-1} \left\langle \lambda^2_k, (\Pi_{k+1} - F_k^T \Pi_k - hM_k) \right\rangle \\ &+ \sum_{k=0}^{N-1} \left\langle \lambda^3_k, (\pi_{k+1} - \pi_k - h\tau_{k+1}) \right\rangle + \sum_{k=0}^{N-1} \sum_{\ell=0}^{m} \mu_\ell \phi_\ell(H^2_\ell(R_k, \Pi_k, \pi_k, \tau_k)), \quad (4.9)\end{aligned}$$

where $\lambda^3_k \in \mathbb{R}^3$ is a Lagrange multiplier.

4.4 Description of the Numerical Solver

The numerical solver is based on solving the necessary conditions for optimality. In deriving the necessary conditions, we follow the approach in [84] and use discrete-time variational calculus. The necessary conditions are given by,

$$h\Pi_k^\times = F_k A_k - A_k^T F_k^T, \quad (4.10a)$$

$$R_{k+1} = R_k F_k, \quad (4.10b)$$

$$\Pi_{k+1} = F_k^T \Pi_k + hM_k, \quad (4.10c)$$

$$\pi_{k+1} = \pi_k + h\tau_k, \quad (4.10d)$$

$$\begin{bmatrix} \lambda^1_k \\ \lambda^2_k \\ \lambda^3_k \end{bmatrix} = \begin{bmatrix} {\mathcal{A}_{k+1}}^T & {\mathcal{C}_{k+1}}^T & 0_{3\times n} \\ {\mathcal{B}_{k+1}}^T & {\mathcal{D}_{k+1}}^T & 0_{3\times n} \\ {\mathcal{E}_{k+1}}^T & {\mathcal{G}_{k+1}}^T & I_{n\times n} \end{bmatrix} \begin{bmatrix} \lambda^1_{k+1} \\ \lambda^2_{k+1} \\ \lambda^3_{k+1} \end{bmatrix} - \begin{bmatrix} \mathcal{H}_{k+1} \\ \mathcal{L}_{k+1} \\ \mathcal{P}_{k+1} \end{bmatrix}, \quad (4.10e)$$

$$h\lambda^3_k = D_{\tau_k} C_d + \sum_{\ell=1}^{m} \mu_\ell D_{\tau_k} \left(\phi_\ell \circ H_\ell\right), \quad (4.10f)$$

where,

$$
\begin{aligned}
\mathcal{A}_k &= {F_k}^T, \\
\mathcal{B}_k &= h \left\{ \begin{array}{c} \left\{ tr\left[F_k A_k\right] I_{3\times 3} - F_k A_k \right\} F_k - \\ \frac{1}{4}\left\{ tr\left[F_k\right] I_{3\times 3} - {F_k}^T \right\} \mathcal{S}\left(J_w\right) \mathcal{S}^T \left\{ tr\left[F_k\right] I_{3\times 3} - {F_k}^T \right\} \end{array} \right\}^{-1}, \\
\mathcal{C}_k &= h\mathcal{M}_k, \\
\mathcal{D}_k &= {F_k}^T + \left({F_k}^T \Pi_k\right)^{\times} \mathcal{B}_k, \\
\mathcal{E}_k &= -\mathcal{B}_k \left(\frac{1}{2}\left\{ tr\left[F_k\right] I_{3\times 3} - {F_k}^T \right\} \mathcal{S} \right), \\
\mathcal{G}_k &= \left({F_k}^T \Pi_k\right)^{\times} \mathcal{E}_k, \\
\mathcal{H}_k &= \left(\left(R_k^T \left(D_{R_k} C_d^2 \right) \right)_A \right)^{-\times} + \sum_{\ell=1}^{m} \mu_\ell \left(\left(R_k^T \left(D_{R_k} \left(\phi_\ell \circ H_\ell \right) \right) \right)_A \right)^{-\times}, \\
\mathcal{L}_k &= D_{\Pi_k} C_d^2 + \sum_{\ell=1}^{m} \mu_\ell D_{\Pi_k} \left(\phi_\ell \circ H_\ell \right), \\
\mathcal{P}_k &= D_{\pi_k} C_d^2 + \sum_{\ell=1}^{m} \mu_\ell D_{\pi_k} \left(\phi_\ell \circ H_\ell \right).
\end{aligned}
$$

In the above equations, $\mathcal{S} \in \mathbb{R}^{3\times n}$, the reaction wheel configuration matrix, and $J_w \in \mathbb{R}^{n\times n}$, the rotational inertia matrix of RWA, are defined by,

$$
\mathcal{S} = \left[\begin{array}{ccc} s_1 & \cdots & s_n \end{array} \right], \tag{4.11}
$$

$$
J_w = \left[\begin{array}{ccc} J_1 & 0 & 0 \\ 0 & \ddots & 0 \\ 0 & 0 & J_n \end{array} \right]. \tag{4.12}
$$

The details of the derivation are available in the appendix.

To solve the two-point boundary value problem (4.10), the indirect single shooting method is used where the goal is to determine the initial values of the Lagrange multipliers and we follow a similar approach to [84, 85].

The sensitivity derivatives for (4.10b)-(4.10d) are given by,

$$\begin{bmatrix} \zeta_{k+1} \\ \delta\Pi_{k+1} \\ \delta\pi_{k+1} \end{bmatrix} = \begin{bmatrix} \mathcal{A}_k & \mathcal{B}_k & \mathcal{E}_k \\ \mathcal{C}_k & \mathcal{D}_k & \mathcal{E}_k \\ 0_{n\times 3} & 0_{n\times 3} & I_{n\times n} \end{bmatrix} \begin{bmatrix} \zeta_k \\ \delta\Pi_k \\ \delta\pi_k \end{bmatrix} + \begin{bmatrix} 0_{3\times n} \\ 0_{3\times n} \\ hI_{n\times n} \end{bmatrix} \delta\tau_k, \tag{4.13}$$

while the sensitivity derivatives for (4.10e) are given by,

$$\begin{bmatrix} \delta\lambda^1_{k+1} \\ \delta\lambda^2_{k+1} \\ \delta\lambda^3_{k+1} \end{bmatrix} = S_k \begin{bmatrix} \zeta_{k+1} \\ \delta\Pi_{k+1} \\ \delta\pi_{k+1} \\ \delta\tau_k \\ \delta\lambda^1_k \\ \delta\lambda^2_k \\ \delta\lambda^3_k \end{bmatrix}, \tag{4.14}$$

where S_k is a $(6+n)\times(12+3n)$ matrix. Expressing $\delta\tau_k$ in terms of τ_k and $\delta\lambda^3_k$, from (4.13)-(4.14), we obtain,

$$\begin{bmatrix} \zeta_{k+1} \\ \delta\Pi_{k+1} \\ \delta\pi_{k+1} \\ \delta\lambda^1_{k+1} \\ \delta\lambda^2_{k+1} \\ \delta\lambda^3_{k+1} \end{bmatrix} = T_k \begin{bmatrix} \zeta_k \\ \delta\Pi_k \\ \delta\pi_k \\ \delta\lambda^1_k \\ \delta\lambda^2_k \\ \delta\lambda^3_k \end{bmatrix}, \tag{4.15}$$

where T_k is an $(12+2n)\times(12+2n)$ matrix. Therefore, from (4.15) we obtain,

$$\begin{bmatrix} \zeta_N \\ \delta\Pi_N \\ \delta\pi_N \\ \delta\lambda_N^1 \\ \delta\lambda_N^2 \\ \delta\lambda_N^3 \end{bmatrix} = \left(\prod_{k=0}^{N-1} T_k\right) \begin{bmatrix} \zeta_0 \\ \delta\Pi_0 \\ \delta\pi_0 \\ \delta\lambda_0^1 \\ \delta\lambda_0^2 \\ \delta\lambda_0^3 \end{bmatrix}. \tag{4.16}$$

To determine the initial values of the Lagrange multipliers, we employ the indirect single shooting method, the iterations of which have the following form,

$$\lambda_0^{(p+1)} = \lambda_0^{(p)} - \gamma \left[\frac{\delta E^{(p)}}{\delta \lambda_0^{(p)}}\right]^{-1} E^{(p)}, \tag{4.17}$$

where the superscripts represent the iteration number, the step size γ is a scalar satisfying $0 < \gamma \leq 1$, and $E^{(p)}$ and $\delta E^{(p)}$ are given below,

$$E^{(p)} = \begin{bmatrix} \lambda_{N-1}^{1(p)} + ((R_N^T(D_{R_N}K_d^1))_A)^{-\times(p)} \\ \lambda_{N-1}^{2(p)} + D_{\Pi_N}K_d^{1(p)} \\ \lambda_{N-1}^{3(p)} + D_{\pi_N}K_d^{1(p)} \end{bmatrix},$$

$$\delta E^{(p)} = \begin{bmatrix} \delta\lambda_{N-1}^{1(p)} + ((\delta R_N^T(D_{R_N}K_d^2) + R_N^T(\delta D_{R_N}K_d^2))_A)^{-\times(p)} \\ \delta\lambda_{N-1}^{2(p)} + \delta D_{\Pi_N}K_d^{2(p)} \\ \delta\lambda_{N-1}^{3(p)} + \delta D_{\pi_N}K_d^{2(p)} \end{bmatrix}.$$

The numerical solver is summarized in Fig. 4.2. During each sampling period, the solver determines the Lagrange multipliers so that the terminal boundary conditions are satisfied. During the initialization step (① in Fig. 4.2), the initial value of (4.17) is set to the solution from the previous sampling time. The numerical solver then updates the values of the Lagrange multipliers using the necessary conditions for

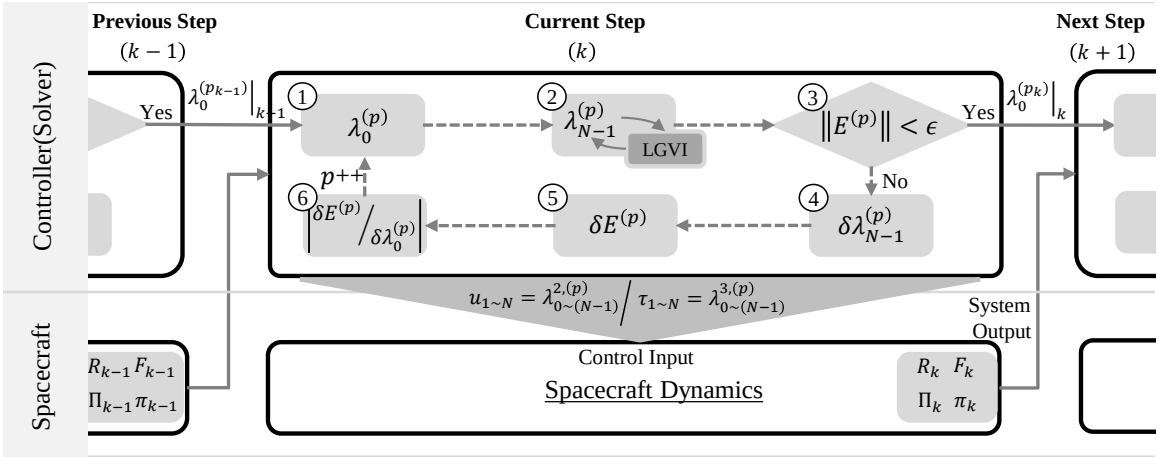

Figure 4.2: The logic diagram of the developed computational solver.

optimality in ②. The shooting method proceeds through the steps in ④, ⑤, and ⑥, until the termination criterion is satisfied in ③ for $\epsilon = 10^{-5}$. Note that the parameter γ is initially set at 1; if after 50 iterations, i.e., $p = 50$, (4.17) has not converged, then the algorithm sets $\gamma = 0.1$.

Remark 1. Our solution to the NMPC problem is based on the exterior penalty function approach and the indirect single shooting method which is straightforward in terms of computational implementation when the equations of motion are formulated based on LGVI. Other techniques, such as multiple shooting, interior point or sequential quadratic programming, may also be of interest for future applications.

4.5 Simulations and Discussion

In this section, we report simulation results for three cases. The first case corresponds to a spacecraft with external control moments with equations of motion given in (4.1) and the other two cases correspond to spacecraft with the two different reaction wheel configurations that were presented in Fig. 4.1(b).

Table 4.1: Summary of cost functions and inequality constraints

Spacecraft with external control moments	Spacecraft with RWA
$K_d^1 = \frac{1}{2}\|P_1^{\frac{1}{2}}(R_N - I_{3\times 3})\|_F^2 + \frac{1}{2}\Pi_N^T P_2 \Pi_N,$	$K_d^2 = \frac{1}{2}\|P_1^{\frac{1}{2}}(R_N - I_{3\times 3})\|_F^2 + \frac{1}{2}(\Pi_N - \mathcal{S}\pi_N)^T P_2(\Pi_N - \mathcal{S}\pi_N),$
$C_d^1 = \frac{h}{2}\|Q_1^{\frac{1}{2}}(R_k - I_{3\times 3})\|_F^2 + \frac{h}{2}\Pi_N^T Q_2 \Pi_N + \frac{h}{2}u_k^T Q_3 u_k,$	$C_d^2 = \frac{h}{2}\|Q_1^{\frac{1}{2}}(R_k - I_{3\times 3})\|_F^2 + \frac{h}{2}(\Pi_k - \mathcal{S}\pi_k)^T Q_2(\Pi_k - \mathcal{S}\pi_k) + \frac{h}{2}\tau_k^T Q_3 \tau_k,$
$H_1^1 = \|u_k\|_\infty - \alpha,$	$H_1^2 = \|\tau_k\|_\infty - \alpha,$
$H_2^1 = \beta - v^T R_k^T w.$	$H_2^2 = \beta - v^T R_k^T w,$
	$H_3^2 = \|\pi_k\|_\infty - \chi.$

4.5.1 Cost Functions and Inequality Constraints

The cost functions $K_d^{1,2}$ and $C_d^{1,2}$ and constraint functions $H_\ell^{1,2}$ corresponding to the three simulations are presented in Table 4.1. The matrices P_1, P_2, Q_1, Q_2, and Q_3 are symmetric positive-definite cost matrices. The constraints prescribed by $H_1^{1,2}$ correspond to the maximum available control torque u_k or τ_k, where $u_k = [u_{1,k}\ u_{2,k}\ u_{3,k}]^T$ and $\tau_k = [\tau_{1,k}\ \cdots\ \tau_{n,k}]^T$. The constraint $H_2^{1,2}$ corresponds to an inclusion/exclusion-zone constraint, where the cosine of the angle between the unit vectors $R_k v$ and w must be greater than β. The final constraint that we consider is H_3^2, which is the maximum limit on the allowable rotation wheel angular momenta π_k, where $\pi_k = [\pi_{1,k}\ \cdots\ \pi_{n,k}]^T$; the limit is denoted by χ.

The penalty functions ϕ_ℓ are differentiable and defined through,

$$\phi_\ell \circ H_\ell^{1,2} = h \max\{0, H_\ell^{1,2}\}^2, \ell = 1, 2, 3. \tag{4.18}$$

4.5.2 Simulation Results

We consider a spacecraft with a moment of inertia matrix $J = \text{diag}(1.0, 1.0, 0.8)$ kg-m^2. We set the integration time step to $h = 0.4$s, and we set the prediction horizon for the MPC algorithm to $N = 5$. The weighting matrices are chosen as,

$$P_1 = P_2 = Q_1 = Q_2 = 0.01 I_{3\times 3}. \tag{4.19}$$

In some of the subsequent figures, the attitude maneuver is plotted on the 2-sphere S^2, where the vectors corresponding to the first, second and third column of R_0 are plotted in dashed-red, dashed-green and dashed-blue, respectively. Similarly, the paths that are traced by the ends of the vectors corresponding to the first, second and third column of R_k are plotted in red, green and blue, respectively.

In the following, simulation results are reported for the cases of spacecraft with 3 and 4 reaction wheels.

4.5.2.1 Spacecraft with RWA of 3 wheels

We begin by considering a spacecraft with RWA corresponding to the 3-wheel configuration,

$$\mathcal{S} = \begin{bmatrix} s_1 & s_2 & s_3 \end{bmatrix} = \begin{bmatrix} 1 & 0 & 0 \\ 0 & 1 & 0 \\ 0 & 0 & 1 \end{bmatrix}.$$

Simulations of spacecraft attitude maneuvering are performed with and without constraints on the reaction wheel torque H_1, the exclusion/inclusion zone H_2, and the reaction wheel maximum angular momentum H_3. The constraint parameters are given by $\alpha = 0.01$, $\beta_1 = \cos(170^\circ)$, $v = [1\ 0\ 0]^T$, $w = -[0.8851\ 0.3888\ 0.2558]^T$, and $\chi = 0.05$. The penalty weights are chosen so that they are small enough to allow for

the solver to quickly converge, but large enough to ensure that the constraints are reasonably enforced. Their values are given by $\mu_1 = 10^7$, $\mu_2 = 10^3$, and $\mu_3 = 10^4$, which have been determined by running multiple simulations.

The initial conditions have been chosen judiciously in order to ensure that the constraints become active during the simulation. The initial conditions for the attitude, the angular momentum of the spacecraft body, and the angular momentum of each reaction wheel are given by,

$$R_0 = \exp(\zeta^{\times}),\ \Pi_0 = 0,\ \pi_0 = \begin{bmatrix} 0.008 & 0.000 & -0.015 \end{bmatrix}^T, \tag{4.20}$$

where $\zeta = \begin{bmatrix} 0.5 & 0.5 & 0.5 \end{bmatrix}^T$. The inertia values of the reaction wheels are $J_1 = J_2 = J_3 = 0.01$ and $Q_3 = I_{3\times 3}$. Both the constraint-free and constrained simulations are presented in Fig. 4.3.

Referring to the subplots of Fig. 4.3, we can see that the constraint-free simulation is stabilizing but violates the exclusion zone constraint in ①, the torque constraints in ③ and ④, and the angular momentum constraints in ⑤ and ⑥. In the constrained simulation, all of these constraints are tightly enforced.

4.5.2.2 Spacecraft with RWA of 4 wheels

In the next case, we consider the 4-reaction wheel configuration corresponding to,

$$\mathcal{S} = \begin{bmatrix} s_1 & s_2 & s_3 & s_4 \end{bmatrix} = \begin{bmatrix} 1 & 0 & 0 & 0.5774 \\ 0 & 1 & 0 & 0.5774 \\ 0 & 0 & 1 & 0.5774 \end{bmatrix}.$$

The constraint parameters have been changed to $\alpha = 0.02$, $\beta = \cos(170^\circ)$, $v = [1\ 0\ 0]^T$, $w = -[0.9624\ \ -0.2017\ 0.1818]^T$, and $\chi = 0.04$. In this case, the torque constraint from the previous case was found to be too stringent as the solver was unable to

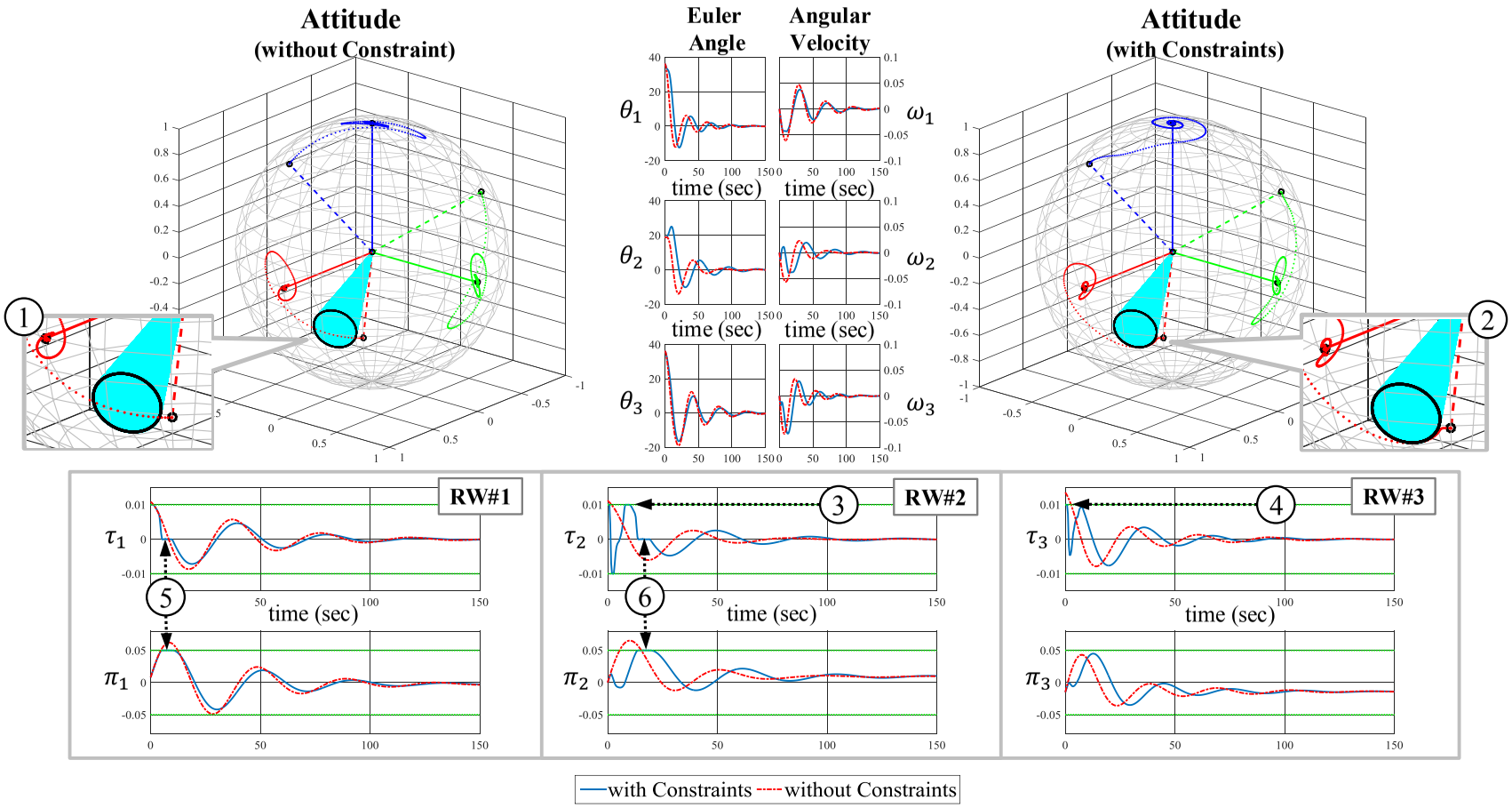

Figure 4.3: Model Predictive Control of 3-RWA Spacecraft with (blue) and without (red) Constraints.

simultaneously satisfy all constraints, so a larger value of α had to be considered. The other constraints were changed in order to modify the simulation scenario. The initial conditions are the same as in the previous case, except that the angular momentum of each reaction wheel has been modified in order to ensure the activation of the angular momentum constraint. The new initial conditions are given as follows,

$$\pi_0 = \begin{bmatrix} 0.010 & 0.000 & 0.005 & -0.020 \end{bmatrix}^T.$$

The inertia values of the reaction wheels are given by $J_1 = J_2 = J_3 = J_4 = 0.01$. The $Q_3 = I_{4\times 4}$ is used. The constraint-free and constrained simulation results are presented in Fig. 4.4.

Referring to the subplots of Fig. 4.4, we can see that, while the exclusion zone constraint is violated in ①, it is enforced by the NMPC control law in ②. Furthermore, we can see that the torque constraints are activated by control jumps in ③ and ④. These control torque jumps occur in order to prevent the violation of the zone constraint and we note that, if the jump is deemed to be too large, its magnitude can be reduced by increasing the length of the prediction horizon N. In the next example, we consider the use of a longer prediction horizon.

4.5.2.3 Spacecraft with external control moments

A simulation of the spacecraft with external moments is performed with and without constraints only on the external moments and the exclusion/inclusion zone. As in the previous cases, we set the same integration time step at $h = 0.4$ sec, but the prediction horizon for the NMPC algorithm is now increased to $N = 10$, allowing us to investigate the effect of a longer prediction horizon. The torque constraint constrain parameter is chosen to be $\alpha = 0.05$, and the penalty weights are chosen to be $\mu_1 = 10^4$ and $\mu_2 = 5$. In the longer prediction horizon case, even with a weight

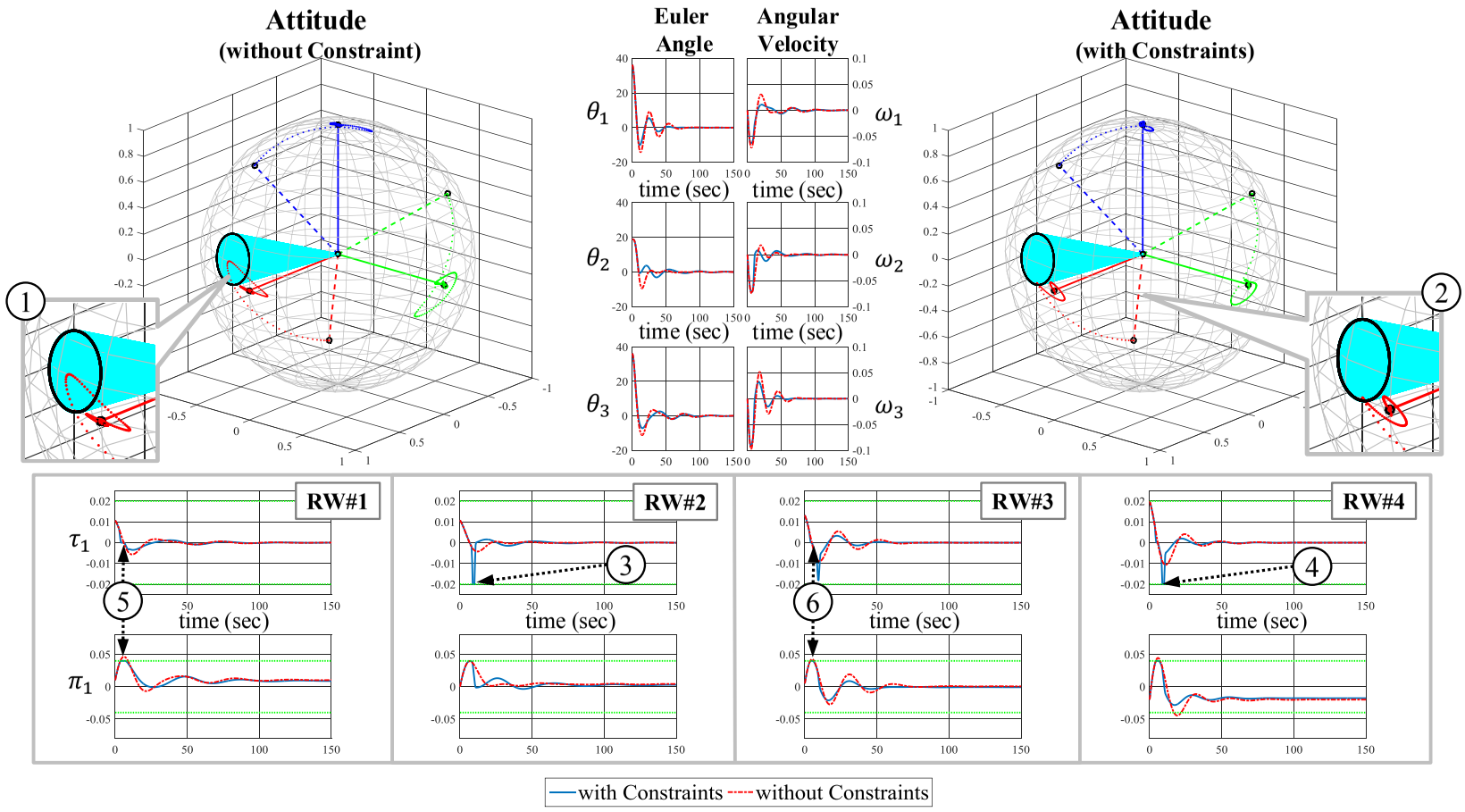

Figure 4.4: Model Predictive Control of 4-RWA Spacecraft with and without Constraints.

lower than in the shorter horizon case, the controller can find a solution which satisfies the constraints. The initial conditions of the attitude, the body angular velocity, and the zone constraint are the same as those for the first simulation, corresponding to the 3-wheel case of the spacecraft with RWA.

The simulations results are presented in Fig. 4.5.

The subplots ① and ② in Fig. 4.5 show that the zone constraint can be satisfied by using the NMPC law, while ③, ④, and ⑤ show the satisfaction of the external moment constraint.

With the longer prediction horizon, the stabilization time and the overshoot in the attitude responses are shorter than in the previous simulations. This observation corresponds to simulations performed on the the 3- and 4-wheel RWA configurations with longer prediction horizons. In general, a longer prediction horizon N corresponds to a shorter stabilization time and smaller overshoot, but the NMPC computation takes longer to converge, especially in the complex case where there are many constraints. Two examples of the spacecraft with RWA have a shorter prediction horizon (5 steps) than the example of the spacecraft with external moments (10 steps). This is because we want to show that the suggested algorithm is capable of handling 3 different constraint categories simultaneously. When the spacecraft with RWA has a zone constraint only, the longer prediction horizon works well and also yields results similar to those of the example of the spacecraft with external moments. The longer prediction horizon reduces the overshoot and stabilization time, but if there exists different constraint categories in the problem, a shorter horizon can effectively prevent the simultaneous violation of multiple constraints.

4.5.3 Domain of Attraction

We now investigate the closed-loop domain of attraction of our NMPC algorithm by simulating 13,357 rest-to-rest orientation maneuvers for the spacecraft with RWA

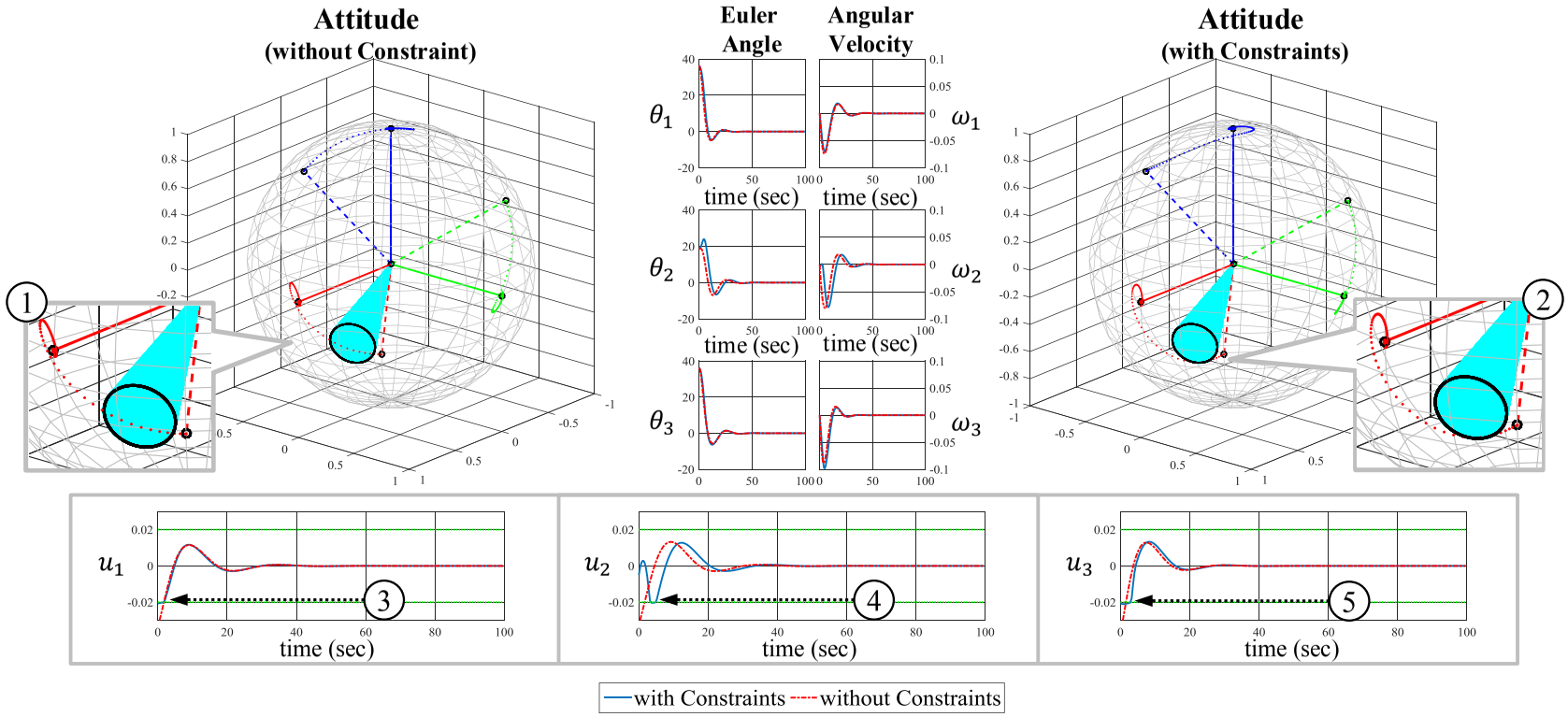

Figure 4.5: Model predictive control of spacecraft with and without the constraints.

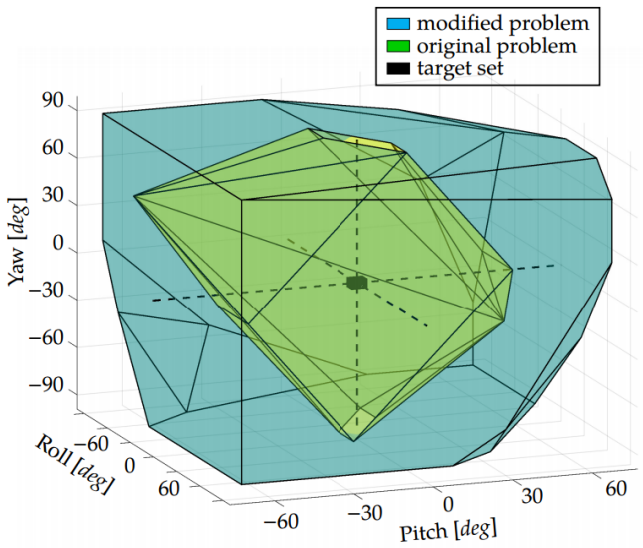

Figure 4.6: The domain of attractions of the linearization based MPC controllers [5].

subject to maximum wheel torque constraints, but with state constraints turned off, i.e., $H_2^{1,2} = H_3^{1,2} \equiv 0$.

Below, we list all combinations of 3-2-1 Euler angle parametrizations corresponding to the at-rest initial conditions that the algorithm is able to stabilize to the desired equilibrium $R_k = I_{3\times 3}$. All other state initial conditions are set to 0.

- Roll : $-90°,\ -80°,\ -70°, \cdots,\ 80°,\ 90°$ (19 cases)
- Pitch : $-90°,\ -80°,\ -70°, \cdots,\ 80°,\ 90°$ (19 cases)
- Yaw : $0°,\ 10°,\ 20°,\ \cdots,\ 350°,\ 360°$ (37 cases)

Guiggiani also proposed this domain of attraction analysis in [5]. He has selected the domain of initial conditions for which the controller is able to drive the state trajectories to a target set (0° roll, pitch, and yaw angle) within radius 0.05 rad. A standard MPC tracking problem and a modified one based on the linearization are compared and Fig. 4.6 shows his results. The proposed NMPC controller's domain of attraction is wider than the one of the linearized controller's, while is computationally expensive.

4.5.4 Computation time

In Fig. 4.7, we report the computation times corresponding to 8 different simulations of 3-RWA example. Fig. 4.7(a) is the calculation results only with the actuator maximum torque constraints (H_1^2) and Fig. 4.7(b) is the calculation results with the zone constraints (H_2^2) which used in the first 3-RWA example. When there is a con-

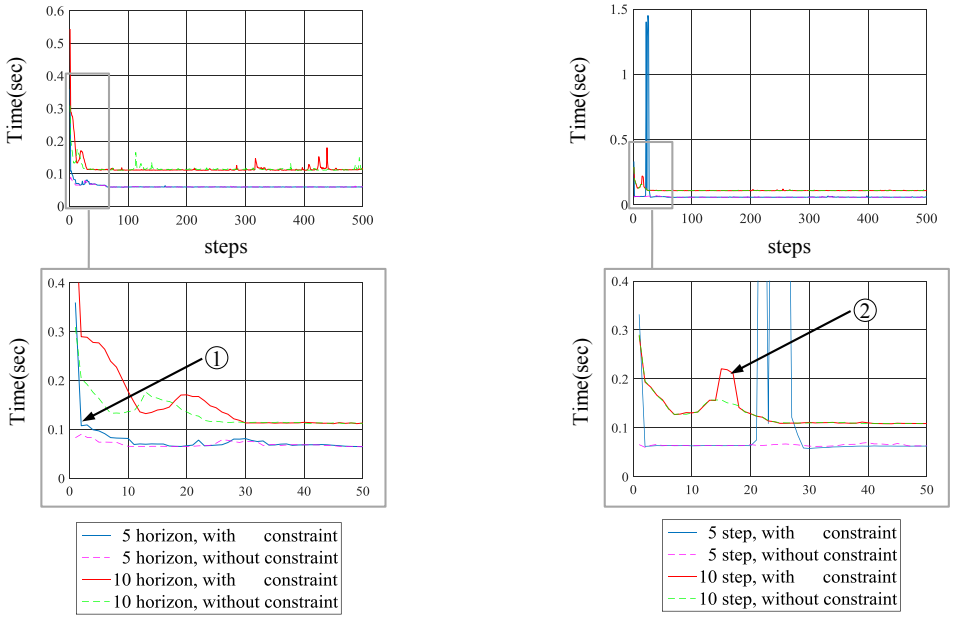

(a) With control constraint

(b) With attitude constraint

Figure 4.7: The calculation time comparison of 4-RWA spacecraft on the Intel Xenon 3.5GHz, 32GB RAM machine, with MATLAB.

trol constraint, the 5 horizon case (indicated by ①) satisfies this computation time requirement but, when there is an attitude constraint, the 10 horizon case (indicated by ②) satisfies the requirement.

4.6 Conclusions

In this chapter, we presented an NMPC approach to the constrained attitude control of spacecraft. The work extends the solver of [84] to the case of spacecraft with

RWA. The work is distinguished by exploiting discrete-time LGVI models which respect the underlying Lie group structure of SO(3) and is consistent with the geometric mechanics and control formalism. The numerical solution to the NMPC optimization problem was obtained using necessary conditions for optimality, and a single shooting method to solve the resulting two point boundary value problem. The sensitivity derivatives were derived to be used in the solution process. Our simulation results showed that this approach is able to achieve well-behaved closed-loop responses with large domain of attraction while satisfying a variety of constraints. Thus, we have developed a constrained-based controller that is capable of implementing the opimtization operational scenarios of the MDO effort in the prior the chapter.

CHAPTER V

Conclusions and Future Work

To maximize the performance of a complex space system, this dissertation proposes a multidisciplinary optimization (MDO) approach that unifies design and operation. Applying MDO to space system design and operation is a challenging task that requires the underlying disciplines to be developed and analyzed first. Thus, the Single Discipline Optimization (SDO) of the photovoltaic power system is performed and its discipline is modeled because of its influence on many other disciplines such as attitude control and communication.

From the photovoltaic power SDO, we developed two key benefits useful for the MDO problem of a complex-shaped space system. The first is the ability to quickly assess self-induced shadowing using a CAD model and OpenGL. The second is the ability to calculate the Suns angles in a body-fixed spherical frame with the help of orbital and attitude dynamics simulators. These two advantages enable the fast calculation of power generation of the complex-shaped satellite, which is essential for MDO.

This baseline model enables the application of the MDO approach to the design and operation of a constrained space system. However, moving from SDO to MDO poses a significant challenge. The unified optimization of the system design and operation increases the number of design variables drastically, which creates a difficult

problem to solve. To solve the problem, the large-scale multidisciplinary design optimization framework developed by Hwang et al. is implemented in the developed approach. Our MDO problem includes six extendable disciplines and more than thousands of operation variables. Despite this complexity, the optimization results show that both the geometry and operation optimization each increase the output of the objective function (total amount of the downloaded data) as much as 40%.

This dissertation also proposes ways to apply the ground optimization results to the on-orbit attitude operation of a satellite. To accomplish this, a Nonlinear Model Predictive Control (NMPC) approach to the constrained attitude control of spacecraft is developed. The NMPC controller exploits a discrete-time LGVI model which respects the underlying Lie group structure of SO(3). The necessary conditions for optimality are derived and a single shooting method is implemented to solve the resulting two-point boundary value problem.

The design methodology introduced in this dissertation can be applied to any satellite design and the process is summarized as follows. First, the satellite shadow analysis of the attitude sphere using both OpenGL and a CAD model is required as described in Chapter II. Next, the attitude requirements of the mission need to be defined with actuator hardware specifications. The embedding of the attitude operation must be organized, as discussed in Chapter III. Third, satellite engineers can develop the required disciplines or, alternately, adopt the disciplines of this dissertation to include the interested discipline to the MDO. After developing the disciplines, the MDO of the satellite can be performed using Modular Analysis and Unified Derivatives (MAUD), as in Chapter III. The satellite geometry can be finalized by the optimization results, but the attitude operation optimization can only be finalized with the development of the attitude controller. There are two ways to develop the attitude operation controller. One is to set the optimization results as the desired value of a controller, and the other is to change the results as the form of constraints.

If attitude operation optimization results can be converted to the desired attitude, any attitude control algorithm can be implemented for the ADCS development. However, the operation results require being changed to the constraints form, and the NMPC attitude controller suggested in Chapter IV needs to be adopted as a main control algorithm. By finishing the above steps, it is possible to design a highly constrained space system with maximum performance.

The complexity and the long computation time of the proposed MDO problem requires expensive computational price. In addition, the approximated operation in orbit and the gap with the ground design results also degrade the effectiveness of the MDO. However, the proposed methodology guarantees the improved performance of the objective function and evaluates the satisfaction of the mission requirement.

This methodology has been applied to the design of a small satellite called CADRE as a example, which is funded by the NSF to study space weather and is scheduled to deploy in 2016.

The methodology of this dissertation is applicable to small satellite technology of which future is unlimited and promising. Small satellite technology is currently applied in science, surveillance, remote site communications, scanning of unattended sensors, high-resolution Earth observations, and environmental monitoring [90]. By applying this multidisciplinary approach, the small satellite will extend its application area and achieve better performance as defined by the objective function. Many research opportunities and interesting applications exist to further explore the MDO approach developed in this dissertation. Some of these are described here.

- **Constrained spacecraft attitude control with NMPC**

  The NMPC approach for the constrained attitude control of spacecraft with a Reaction Wheel Assembly (RWA) can be extended to different dynamic system applications such as a spacecraft with a Control Moment Gyroscope (CMG). It is because both devices, RWA and CMG, use their own angular momentum to

control a spacecraft. NMPC can be also extended to different implementations of optimization solvers as a replacement for the single shooting method widely used in current research.

- **Constrained power regulator control of a spacecraft EPS with NMPC**

  Since MPC approaches show good performance on the constrained control [91], it can be effectively applied to the photovoltaic-battery power system control of the spacecraft. For the photovoltaic array and the battery stack, the power generation model and the simulator suggested in this dissertation can provide a good developing environment.

- **Developing and extending applications of the multidisciplinary design and operation optimization**

  The design of satellites and their operation is a complex task that involves a large number of variables and multiple engineering disciplines. Given the encouraging results of this dissertation, the application of this MDO methodology can be extended to various system designs, such as electrified vehicles or unmanned air vehicles.

- **High-altitude wireless network based on the balloon or the small satellite fleet**

  Recent reports indicate that Google and Facebook are also considering and researching high-altitude balloons and small satellites as a part of their future networking infrastructure. High-altitude balloons and small satellite fleets will be interesting targets of MPC and MDO approaches. For instance, both applications require power control with photovoltaic arrays and a battery stack. They also require attitude control for pointing, to which MPC control can be effectively applied. In addition, fleet design and construction with minimal resources could be other useful applications of MDO technology.

APPENDICES

APPENDIX A

Derivation of the necessary conditions of optimality and terminal condition for RWA Spacecraft

The variations of R_k, F_k, Π_k, and π_k are given as follows,

$$R_{k,\varepsilon} = R_k \exp\left(\varepsilon \zeta_k^{\times}\right),$$
$$F_{k,\varepsilon} = F_k \exp\left(\varepsilon \xi_k^{\times}\right),$$
$$\Pi_{k,\varepsilon} = \Pi_k + \varepsilon \delta \Pi_k,$$
$$\pi_{k,\varepsilon} = \pi_k + \varepsilon \delta \pi_k,$$

where $\zeta_k, \xi_k \in \mathbb{R}^3$.

Note that $\zeta_0 = \xi_0 = \delta\Pi_0 = \delta\pi_0 = 0$. The infinitesimal variations of R_k, F_k, Π_k,

and π_k are given by,

$$\delta R_k = \left.\frac{d}{d\varepsilon}\right|_{\varepsilon=0} R_{k,\varepsilon} = R_k \zeta_k^{\times},$$
$$\delta F_k = \left.\frac{d}{d\varepsilon}\right|_{\varepsilon=0} F_{k,\varepsilon} = F_k \xi_k^{\times},$$
$$\delta \Pi_k = \left.\frac{d}{d\varepsilon}\right|_{\varepsilon=0} \Pi_{k,\varepsilon} = \delta \Pi_k,$$
$$\delta \pi_k = \left.\frac{d}{d\varepsilon}\right|_{\varepsilon=0} \pi_{k,\varepsilon} = \delta \pi_k.$$

A few facts are required to proceed further.

Fact 1 ([85]). ζ_k, ζ_{k+1}, and ξ_k satisfy,

$$\zeta_{k+1} = F_k^T \zeta_k + \xi_k.$$

Proposition 1. ξ_k, $\delta\Pi_k$, and $\delta\pi_k$ satisfy,

$$\xi_k = \mathcal{B}_k \delta \Pi_k + \mathcal{E}_k \delta \pi_k,$$

where,

$$\mathcal{B}_k = h \begin{Bmatrix} \{tr\left[F_k A_k\right] I_{3\times 3} - F_k A_k\} F_k \\ -\frac{1}{4}\left\{tr\left[F_k\right] I_{3\times 3} - {F_k}^T\right\} \mathcal{S}\left(J_w\right) \mathcal{S}^T \left\{tr\left[F_k\right] I_{3\times 3} - {F_k}^T\right\} \end{Bmatrix}^{-1},$$
$$\mathcal{E}_k = -\mathcal{B}_k \left(\frac{1}{2}\left\{tr\left[F_k\right] I_{3\times 3} - {F_k}^T\right\} \mathcal{S}\right).$$

Proof. We begin with the following,

$$\begin{aligned}
h\delta\pi_{i_k} &= J_i\left(\delta\Delta\theta_{i_k} - \frac{1}{2}tr\left[\delta F_k {s_i}^{\times}\right]\right) \\
&= J_i\left(\delta\Delta\theta_{i_k} - \frac{1}{2}tr\left[F_k\xi_k^{\times}{s_i}^{\times}\right]\right) \\
&= J_i\left(\delta\Delta\theta_{i_k} - \frac{1}{2}tr\left[\xi_k^{\times}{s_i}^{\times}F_k\right]\right) \\
&= J_i\left(\delta\Delta\theta_{i_k} - \frac{1}{2}tr\left[\xi_k^{\times}\left((M_{i_k})_S + (M_{i_k})_A\right)\right]\right) \\
&= J_i\left(\delta\Delta\theta_{i_k} - \frac{1}{2}tr\left[\xi_k^{\times}(M_{i_k})_A\right]\right) \\
&= J_i\left(\delta\Delta\theta_{i_k} - \frac{1}{2}tr\left[\xi_k^{\times}{\gamma_{i_k}}^{\times}\right]\right) \\
&= J_i\left(\delta\Delta\theta_{i_k} + {\xi_k}^T\gamma_{i_k}\right),
\end{aligned}$$

where,

$$\begin{aligned}
M_{i_k} &= {s_i}^{\times}F_k = (M_{i_k})_S + (M_{i_k})_A, \\
(M_{i_k})_A &= \frac{{s_i}^{\times}F_k - ({s_i}^{\times}F_k)^T}{2} = \frac{{s_i}^{\times}F_k + {F_k}^T({s_i}^{\times})}{2} = \gamma_{i_k}^{\times}, \\
\gamma_{i_k} &= \frac{1}{2}\left\{tr\left[F_k\right]I_{3\times 3} - F_k\right\}s_i.
\end{aligned}$$

By using the matrices $\mathcal{S}$ and J_w, we obtain,

$$h\delta\pi_k = J_w\left(\delta\Delta\theta_k + \frac{1}{2}\mathcal{S}^T\left\{tr\left[F_k\right]I_{3\times 3} - F_k\right\}^T\xi_k\right),$$

which leads to,

$$\delta\Delta\theta_k = h\left(J_w\right)^{-1}\delta\pi_k - \frac{1}{2}\mathcal{S}^T\left\{tr\left[F_k\right]I_{3\times 3} - F_k\right\}^T\xi_k.$$

Since,

$$h(\delta\Pi_k)^{\times} = \delta F_k A_k - {A_k}^T\delta{F_k}^T + F_k\delta A_k - \delta{A_k}^T{F_k}^T, \tag{A.1}$$

using the following properties,

$$\begin{aligned}
\delta A_k &= \frac{1}{2}\sum_{i=1}^{n} {s_i}^{\times}(J_i \delta\Delta\theta_{i_k}), \\
F_k\delta A_k - \delta A_k{}^T F_k{}^T &= \left(\frac{1}{2}\sum_{i=1}^{n} {s_i}^{\times}(J_i \delta\Delta\theta_{i_k})\right) F_k^T + F_k\left(\frac{1}{2}\sum_{i=1}^{n} {s_i}^{\times}(J_i \delta\Delta\theta_{i_k})\right) \\
&= \left(\left\{tr\left[F_k^T\right] I_{3\times 3} - F_k^T\right\}\left(\frac{1}{2}\sum_{i=1}^{n} s_i(J_i \delta\Delta\theta_{i_k})\right)\right)^{\times} \\
&= \left(\frac{1}{2}\left\{tr\left[F_k^T\right] I_{3\times 3} - F_k^T\right\}\mathcal{S}J_w\delta\Delta\theta_k\right)^{\times},
\end{aligned}$$

we can re-write (A.1) as follows,

$$\begin{aligned}
h(\delta\Pi_k)^{\times} &= F_k{\xi^{\times}}_k A_k - A_k^T{\xi^{\times}}_k{}^T F_k^T + F_k\delta A_k - \delta A_k^T F_k^T \\
&= F_k{\xi^{\times}}_k A_k + A_k^T{\xi^{\times}}_k F_k^T + \left(\frac{1}{2}\left\{tr\left[{F_k}^T\right] I_{3\times 3} - {F_k}^T\right\}\mathcal{S}J_w\delta\Delta\theta_k\right)^{\times} \\
&= (F_k\xi_k)^{\times}F_kA_k + A_k^TF_k^T(F_k\xi_k)^{\times} + \left(\frac{1}{2}\left\{tr\left[{F_k}^T\right] I_{3\times 3} - {F_k}^T\right\}\mathcal{S}J_w\delta\Delta\theta_k\right)^{\times} \\
&= \left(\left\{tr\left[F_kA_k\right] I_{3\times 3} - F_kA_k\right\}F_k\xi_k + \frac{1}{2}\left\{tr\left[{F_k}^T\right] I_{3\times 3} - {F_k}^T\right\}\mathcal{S}J_w\delta\Delta\theta_k\right)^{\times}.
\end{aligned}$$

Applying the inverse of the cross map to both sides of the above equation, we obtain,

$$\begin{aligned}
\delta\Pi_k =& \frac{1}{h}\left\{tr\left[F_kA_k\right] I_{3\times 3} - F_kA_k\right\}F_k\xi_k + \frac{1}{2h}\left\{tr\left[{F_k}^T\right] I_{3\times 3} - {F_k}^T\right\}\mathcal{S}J_w\delta\Delta\theta_k \\
=& \frac{1}{h}\left\{tr\left[F_kA_k\right] I_{3\times 3} - F_kA_k\right\}F_k\xi_k \\
&+ \frac{1}{2h}\left\{tr\left[{F_k}^T\right] I_{3\times 3} - {F_k}^T\right\}\mathcal{S}\left(h\delta\pi_k - \frac{1}{2}J_w\mathcal{S}^T\{tr\left[F_k\right] I_{3\times 3} - F_k\}^T\xi_k\right) \\
=& \frac{1}{h}\left\{\begin{array}{l}\left\{tr\left[F_kA_k\right] I_{3\times 3} - F_kA_k\right\}F_k \\ -\frac{1}{4}\left\{tr\left[F_k\right] I_{3\times 3} - {F_k}^T\right\}\mathcal{S}\left(J_w\right)\mathcal{S}^T\left\{tr\left[F_k\right] I_{3\times 3} - {F_k}^T\right\}\end{array}\right\}\xi_k \\
&+ \frac{1}{2}\left\{tr\left[F_k\right] I_{3\times 3} - {F_k}^T\right\}\mathcal{S}\delta\pi_k.
\end{aligned}$$

The result follows from the expressions for $\delta\Pi_k$ and $\delta\pi_k$. □

Fact 2 ([85]). $\delta M_k = \mathcal{M}_k \zeta_k$, where $\mathcal{M}_k \in \mathbb{R}^{3\times 3}$.

Fact 3 ([92]). $\langle\langle D_{R_k}\mathcal{F}, R_k\eta_k^{\times}\rangle\rangle = \langle((R_k^T(D_{R_k}\mathcal{F}))_A)^{-\times}, \eta_k\rangle$.

With the above facts, the variation of the augmented cost functional can be written as follows,

$$
\begin{aligned}
\delta\mathcal{J}_{d,a}^2 = &\left\langle \left(\left(R_N^T\left(D_{R_N}K_d^2\right)\right)_A\right)^{-\times}, \zeta_N \right\rangle + \left\langle D_{\Pi_N}K_d^2, \delta\Pi_N\right\rangle + \left\langle D_{\pi_N}K_d^2, \delta\pi_N\right\rangle \\
&+ \sum_{k=1}^{N-1}\left\langle \left(\left(R_k^T\left(D_{R_k}C_d^2\right)\right)_A\right)^{-\times}, \zeta_k \right\rangle + \sum_{k=1}^{N-1}\left\langle D_{\Pi_k}C_d^2, \delta\Pi_k\right\rangle \\
&+ \sum_{k=1}^{N-1}\left\langle D_{\pi_k}C_d^2, \delta\pi_k\right\rangle + \sum_{k=1}^{N-1}\left\langle D_{\tau_k}C_d^2, \delta\tau_k\right\rangle \\
&+ \sum_{k=0}^{N-1}\left\langle \lambda_k^1, \left(\zeta_{k+1} - F_k^T\zeta_k - \xi_k\right)\right\rangle \\
&+ \sum_{k=0}^{N-1}\left\langle \lambda_k^2, \left(\delta\Pi_{k+1} - \left(F_k\xi_k^{\times}\right)^T\Pi_k - {F_k}^T\delta\Pi_k - h\mathcal{M}_k\zeta_k\right)\right\rangle \\
&+ \sum_{k=0}^{N-1}\left\langle \lambda_k^3, \left(\delta\pi_{k+1} - \delta\pi_k - h\delta\tau_k\right)\right\rangle \\
&+ \sum_{k=0}^{N-1}\left\langle \sum_{\ell=1}^{m}\mu_\ell\left(\left(R_k^T\left(D_{R_k}\left(\phi_\ell\circ H_\ell^2\right)\right)\right)_A\right)^{-\times}, \zeta_k \right\rangle \\
&+ \sum_{k=0}^{N-1}\left\langle \sum_{\ell=1}^{m}\mu_\ell D_{\Pi_k}\left(\phi_\ell\circ H_\ell^2\right), \delta\Pi_k \right\rangle \\
&+ \sum_{k=0}^{N-1}\left\langle \sum_{\ell=1}^{m}\mu_\ell D_{\pi_k}\left(\phi_\ell\circ H_\ell^2\right), \delta\pi_k \right\rangle \\
&+ \sum_{k=0}^{N-1}\left\langle \sum_{\ell=1}^{m}\mu_\ell D_{\tau_k}\left(\phi_\ell\circ H_\ell^2\right), \delta\tau_k \right\rangle.
\end{aligned}
$$

It can be summarized as following equation.

$$
\begin{aligned}
\delta \mathcal{J}_{d,a}^2 = & \left\langle \left(\left(R_N^T \left(D_{R_N} K_d^2 \right) \right)_A \right)^{-\times}, \zeta_N \right\rangle + \left\langle D_{\Pi_N} K_d^2, \delta \Pi_N \right\rangle + \left\langle D_{\pi_N} K_d^2, \delta \pi_N \right\rangle \\
& + \sum_{k=1}^{N-1} \left\langle \left(\left(R_k^T \left(D_{R_k} C_d^2 \right) \right)_A \right)^{-\times}, \zeta_k \right\rangle + \sum_{k=1}^{N-1} \left\langle D_{\Pi_k} C_d^2, \delta \Pi_k \right\rangle \\
& + \sum_{k=1}^{N-1} \left\langle D_{\pi_k} C_d^2, \delta \pi_k \right\rangle + \sum_{k=1}^{N-1} \left\langle D_{\tau_k} C_d^2, \delta \tau_k \right\rangle \\
& + \sum_{k=0}^{N-1} \left\langle \lambda_k^1, \zeta_{k+1} - F_k^T \zeta_k - \left(\mathcal{B}_k \delta \Pi_k + \mathcal{E}_k \delta \pi_k \right) \right\rangle \\
& + \sum_{k=0}^{N-1} \left\langle \lambda_k^2, \left(\delta \Pi_{k+1} - \left(F_k^T \Pi_k \right)^{\times} \left(\mathcal{B}_k \delta \Pi_k + \mathcal{E}_k \delta \pi_k \right) - {F_k}^T \delta \Pi_k - h \mathcal{M}_k \zeta_k \right) \right\rangle \\
& + \sum_{k=0}^{N-1} \left\langle \lambda_k^3, \delta \pi_{k+1} - \delta \pi_k - h \delta \tau_{k+1} \right\rangle \\
& + \sum_{k=0}^{N-1} \left\langle \sum_{\ell=1}^{m} \mu_\ell \left(\left(R_k^T \left(D_{R_k} \left(\phi_\ell \circ H_\ell^2 \right) \right) \right)_A \right)^{-\times}, \zeta_k \right\rangle \\
& + \sum_{k=0}^{N-1} \left\langle \sum_{\ell=1}^{m} \mu_\ell D_{\Pi_k} \left(\phi_\ell \circ H_\ell^2 \right), \delta \Pi_k \right\rangle \\
& + \sum_{k=0}^{N-1} \left\langle \sum_{\ell=1}^{m} \mu_\ell D_{\pi_k} \left(\phi_\ell \circ H_\ell^2 \right), \delta \pi_k \right\rangle \\
& + \sum_{k=0}^{N-1} \left\langle \sum_{\ell=1}^{m} \mu_\ell D_{\tau_k} \left(\phi_\ell \circ H_\ell^2 \right), \delta \tau_k \right\rangle .
\end{aligned}
$$

Then,

$$
\begin{aligned}
\delta \mathcal{J}_{d,a}^2 = & \left\langle \left(\left(R_N^T \left(D_{R_N} K_d^2 \right) \right)_A \right)^{-\times} + \lambda_{N-1}^1, \zeta_N \right\rangle \\
& + \left\langle D_{\Pi_N} K_d^2 + \lambda_{N-1}^2, \delta \Pi_N \right\rangle + \left\langle D_{\pi_N} K_d^2 + \lambda_{N-1}^3, \delta \pi_N \right\rangle \\
& + \sum_{k=1}^{N-1} \left\langle \begin{pmatrix} \lambda_{k-1}^1 - F_k \lambda_k^1 - h \mathcal{M}_k{}^T \lambda_k^2 + \left(\left(R_k^T \left(D_{R_k} C_d^2 \right) \right)_A \right)^{-\times} \\ + \sum_{\ell=1}^{m} \mu_\ell \left(\left(R_k^T \left(D_{R_k} \left(\phi_\ell \circ H_\ell^2 \right) \right) \right)_A \right)^{-\times} \end{pmatrix}, \zeta_k \right\rangle \\
& + \sum_{k=1}^{N-1} \left\langle \begin{pmatrix} \lambda_{k-1}^2 - \mathcal{B}_k{}^T \lambda_k^1 - \left(F_k - \mathcal{B}_k{}^T \left(F_k{}^T \Pi_k \right)^\times \right) \lambda_k^2 \\ + D_{\Pi_k} C_d^2 + \sum_{\ell=1}^{m} \mu_\ell D_{\Pi_k} \left(\phi_\ell \circ H_\ell^2 \right) \end{pmatrix}, \delta \Pi_k \right\rangle \\
& + \sum_{k=1}^{N-1} \left\langle \begin{pmatrix} \lambda_{k-1}^3 - \mathcal{E}_k{}^T \lambda_k^1 + \mathcal{E}_k{}^T \left(F_k{}^T \Pi_k \right)^\times \lambda_k^2 \\ -\lambda_k^3 + D_{\pi_k} C_d^2 + \sum_{\ell=1}^{m} \mu_\ell D_{\pi_k} \left(\phi_\ell \circ H_\ell^2 \right) \end{pmatrix}, \delta \pi_k \right\rangle \\
& + \sum_{k=1}^{N-1} \left\langle \left(-h \lambda_{k-1}^3 + D_{\tau_k} C_d^2 + \sum_{\ell=1}^{m} \mu_\ell D_{\tau_k} \left(\phi_\ell \circ H_\ell^2 \right) \right), \delta \tau_k \right\rangle,
\end{aligned}
$$

where the analogue of integration by parts in the discrete-time setting is used along with the facts that the variations ζ_k, $\delta\Pi_k$ and $\delta\pi_k$ vanish at $k = 0$. Since $\delta \mathcal{J}_{d,a}^2 = 0$ should vanish for variations of ζ_k, $\delta\Pi_k$, $\delta\pi_k$, and $\delta\tau_k$, we have completed the derivation of the necessary conditions given in (4.10).

APPENDIX B

Publications

Journal Article

[1] Dae Young Lee, Rohit Gupta, Uroš V. Kalabić, Stefano Di Cairano, Anthony M. Bloch, James W. Cutler, and Iliya V. Kolmanovsky, Computational Nonlinear Model Predictive Control on SO(3) for Spacecraft with Reaction Wheel Assembly, *Journal of Guidance Control and Dynamics*, Under Review, 2016.

[2] Dae Young Lee, James W. Cutler, Joe Mancewicz, and Aaron J. Ridley, Maximizing Photovoltaic Power Generation of a Space-dart Configured Satellite, *Acta Astronautica*, Vol. 111, pp.283-299, 2015.

[3] John T. Hwang, Dae Young Lee, James W. Cutler, and Joaquim R. R. A. Martins, Large-Scale Multidisciplinary Optimization of a Small Satellites Design and Operation, *Journal of Spacecraft and Rockets*, Vol. 51, No. 5, pp.1648-1663, 2014.

Conference Article

[1] Dae Young Lee, Rohit Gupta, Uroš V. Kalabić, Stefano Di Cairano, Anthony M. Bloch, James W. Cutler, and Ilya V. Kolmanovsky, Constrained Attitude Maneuvering of a Spacecraft with Reaction Wheel Assembly by Nonlinear Model Predictive Control, *2016 American Control Conference*, Boston, MA, Accepted, 2016.

[2] Dae Young Lee, Hyeongjun Park, and James W. Cutler, Development of CubeSat Attitude Determination and Control System with Hybrid Control Strategy and its Simulator on SO(3), *26th AASAIAA Space Flight Mechanics Meeting*, Napa, CA, February, 2016.

[3] John T. Hwang, Dae Young Lee, James W. Cutler, and Joaquim R. R. A. Martins, Large-Scale MDO of a Small Satellite using a Novel Framework for the Solution of Coupled Systems and their Derivatives, *54th AIAA/ASME/ASCE/AHS/ASC Structures, Structural Dynamics, and Materials Conference*, Boston, MA, April, 2014.

[4] Dae Young Lee, John C. Springmann, Sara C. Spangelo, and James W. Cutler, Satellite Dynamics Simulator Development Using Lie Group Variational Integrator, *AIAA Modeling and Simulation Technologies Conference*, Portland, Oregon, Aug. 8-11, 2011.

BIBLIOGRAPHY

BIBLIOGRAPHY

[1] Michael Swartwout. The first one hundred CubeSats: A statistical look. *Journal of Small Satellites*, 2(2):213–233, 2014.

[2] John T Hwang, Dae Young Lee, James W. Cutler, and Joaquim R. R. A. Martins. Large-scale MDO of a small satellite using a novel framework for the solution of coupled systems and their derivatives. In *Proceedings of the 54th AIAA/ASME/ASCE/AHS/ASC Structures, Structural Dynamics, and Materials Conference*, Boston, MA, April 2013.

[3] Kristian Svartveitk. Attitude determination of the NCUBE satellite. Master's thesis, Norwegian University of Science and Technology, Trondheim, Norway, January 2003.

[4] John T. Hwang, Dae Young Lee, James W. Cutler, and Joaquim R. R. A. Martins. Large-scale multidisciplinary optimization of a small satellites design and operation. *Journal of Spacecraft and Rockets*, pages 1–16, 2014.

[5] Alberto Guiggiani. *Embedded model predictive control: finite precision arithmetic and aerospace applications*. PhD thesis, Lucca, Italy. IMT Institute for Advanced Studies, 2015.

[6] Dae Young Lee, James W Cutler, Joe Mancewicz, and Aaron J. Ridley. Maximizing photovoltaic power generation of a space-dart configured satellite. *Acta Astronautica*, 111:283–299, 2015.

[7] Jaroslaw Sobieszczanski-Sobieski. *Multidisciplinary design optimization: an emerging new engineering discipline*. Springer, 1995.

[8] A. Boudjemai, M.H. Bouanane, L. Merad, and A.M. Si Mohammed. Small satellite structural optimisation using genetic algorithm approach. In *Recent Advances in Space Technologies, 2007. RAST '07. 3rd International Conference on*, pages 398–406, June 2007.

[9] Issamu Muraoka, Roberto L Galski, Fabiano L De Sousa, and Fernando M Ramos. Stochastic spacecraft thermal design optimization with low computational cost. *Journal of Spacecraft and Rockets*, 43(6):1248–1257, 2006.

[10] Roberto L. Galski, Fabiano L. De Sousa, Fernando M. Ramos, and Issamu Muraoka. Spacecraft thermal design with the generalized extremal optimization algorithm. *Inverse Problems in Science and Engineering*, 15(1):61–75, 2007.

[11] Patrick V Hull, Michael Tinker, Michael SanSoucie, and Ken Kittredge. Thermal analysis and shape optimization of an in-space radiator using genetic algorithms. In *Space Technology and Applications International Forum- Staif 2006*, volume 813, pages 81–90, 2006.

[12] Hui-Kyung Kim, Yeongmin Jo, and Seongim Choi. Multi-objective optimization of node-based spacecraft radiator design. *Journal of Spacecraft and Rockets*, 51(5):1695–1708, 2014.

[13] Saurabh Jain and Dan Simon. Genetic algorithm based charge optimization of lithium-ion batteries in small satellites. In *Proceedings of the 19th AIAA/USU Conference on Small Satellites, Utah State University, Logan, UT*, pages Paper SSC05–XI–2, 2005.

[14] S. Khoddam and M.A. Adrakani. Passive control and layout optimization of Mesbah small satellite. *Acta Astronautica*, 52(912):757 – 763, 2003. Selected Proceedings of the 3rd IAA International Symposium on Small Satellites for Earth Observation.

[15] David J Richie, Vaios J Lappas, and Phil L Palmer. Sizing/optimization of a small satellite energy storage and attitude control system. *Journal of Spacecraft and Rockets*, 44(4):940–952, 2007.

[16] Bao Zhang, Hong-Fei Teng, and Yan-Jun Shi. Layout optimization of satellite module using soft computing techniques. *Applied Soft Computing*, 8(1):507–521, 2008.

[17] Brett Malone and WH Mason. Multidisciplinary optimization in aircraft design using analytic technology models. *Journal of Aircraft*, 32(2):431–438, 1995.

[18] J Olds and G Walberg. Multidisciplinary design of a rocket-based combined-cycle SSTO launch vehicle using Taguchi methods. In *Proceedings of AIAA/AHS/ASEE Aerospace Design Conference, Irvine, CA*, pages Paper AIAA 93–1096, 1993.

[19] RD Braun, RW Powell, RA Lepsch, DO Stanley, and IM Kroo. Comparison of two multidisciplinary optimization strategies for launch-vehicle design. *Journal of Spacecraft and Rockets*, 32(3):404–410, 1995.

[20] Lawrence F Rowell, RD Braun, JR Olds, and R Unal. Recent experiences in multidisciplinary conceptual design optimization for launch vehicles. In *AIAA, NASA, and ISSMO, Symposium on Multidisciplinary Analysis and Optimization, 6 th, Bellevue, WA*, pages 642–654, 1996.

[21] Robert A Hickman. Integrated modeling for launch system architecture optimization. In *INCOSE International Symposium*, volume 7, pages 394–402. Wiley Online Library, 1997.

[22] Michael Kesselmann. Optimization and evaluation of single-staged transportation systems example for the solution of highly complex technical problems. In *INCOSE International Symposium*, volume 7, pages 465–472. Wiley Online Library, 1997.

[23] V Engler, D Coors, and D Jacob. Optimization of a space transportation system including design sensitivities. *Journal of Spacecraft and Rockets*, 35(6):785–791, 1998.

[24] Masoud Ebrahimi, Mohammad Reza Farmani, and Jafar Roshanian. Multidisciplinary design of a small satellite launch vehicle using particle swarm optimization. *Structural and Multidisciplinary Optimization*, 44(6):773–784, 2011.

[25] M.A. Zafrane, A. Boudjemai, and N. Boughanmi. Multidisciplinary design optimization of the acoustic interaction between the satellite and launch vehicle. In *Recent Advances in Space Technologies (RAST), 2013 6th International Conference on*, pages 577–582, June 2013.

[26] Mark G Matossian. Earth observing system mission design- constrained optimization of the eos constellation configuration design. In *IAF, International Astronautical Congress, 46 th, Oslo, Norway*, 1995.

[27] Todd Mosher. Applicability of selected multidisciplinary design optimization methods to conceptual spacecraft design. In *Proceedings of the 6th AIAA/NASA/ISSMO, Symposium on Multidisciplinary Analysis and Optimization*, pages 664–671, 1996.

[28] Ellen Riddle. Use of optimization methods in small satellite systems analysis. In *Proceedings of the 12th AIAA/USU Conference on Small Satellites, Utah State University, Logan, UT*, pages Paper SSC98–X–1, 1998.

[29] D. A. Bearden. *A methodology for spacecraft technology insertion analysis balancing benefit, cost, and risk*. PhD thesis, University of Southern California, 1999.

[30] Julia George, John Peterson, and Samuel Southard. Multidisciplinary integrated design assistant for spacecraft (midas). *Proceedings of American Institute of Aeronautics and Astronautics (AIAA)*, 1995.

[31] Alex S Fukunaga, Steve Chien, Darren Mutz, Robert L Sherwood, and Andre D Stechert. Automating the process of optimization in spacecraft design. In *Aerospace Conference, 1997. Proceedings., IEEE*, volume 4, pages 411–427. IEEE, 1997.

[32] Todd Mosher. Spacecraft design using a genetic algorithm optimization approach. In *Aerospace Conference, 1998 IEEE*, volume 3, pages 123–134. IEEE, 1998.

[33] Todd Mosher. Conceptual spacecraft design using a genetic algorithm trade selection process. *Journal of Aircraft*, 36(1):200–208, 1999.

[34] Gary M Stump, Mike Yukish, Timothy W Simpson, and John J O'Hara. Trade space exploration of satellite datasets using a design by shopping paradigm. In *Aerospace Conference, 2004. Proceedings. 2004 IEEE*, volume 6, pages 3885–3895. IEEE, 2004.

[35] Ali Ravanbakhsh, Mahdi Mortazavi, and Jafar Roshanian. Multidisciplinary design optimization approach to conceptual design of a LEO Earth observation microsatellite. In *Proceeding of AIAA SpaceOps 2008 Conference*, 2008.

[36] Ali Ravanbakhsh and Sebastin Franchini. Multiobjective optimization applied to structural sizing of low cost university-class microsatellite projects. *Acta Astronautica*, 79:212 – 220, 2012.

[37] D Barnhart, Tatiana Kichkaylo, and Lucy Hoag. SPIDR: Integrated systems engineering design-to-simulation software for satellite build. In *Conference on Systems Engineering Research*, 2009.

[38] E.R. Taylor. Evaluation of multidisciplinary design optimization techniques as applied to spacecraft design. In *Aerospace Conference Proceedings, 2000 IEEE*, volume 1, pages 371–384 vol.1, 2000.

[39] Cyrus D Jilla and David W Miller. Multi-objective, multidisciplinary design optimization methodology for distributed satellite systems. *Journal of Spacecraft and Rockets*, 41(1):39–50, 2004.

[40] A Jafarsalehi, P Mohammad Zadeh, and M Mirshams. Collaborative optimization of remote sensing small satellite mission using genetic algorithms. *Iranian Journal of Science and Technology, Transactions of Mechanical Engineering*, 36:117–128, 2012.

[41] S. Spangelo and J. Cutler. Integrated approach to optimizing small spacecraft vehicles and operations. In *Proceedings of the 62nd International Astronautical Congress, Cape Town, South Africa*, 2011.

[42] Sara Spangelo, James Cutler, Kyle Gilson, and Amy Cohn. Optimization-based scheduling for the single-satellite, multi-ground station communication problem. *Computers & Operations Research*, 57:1–16, 2015.

[43] Xiaoling Xiong, Chi K Tse, and Xinbo Ruan. Bifurcation analysis of standalone photovoltaic-battery hybrid power system. *Circuits and Systems I: Regular Papers, IEEE Transactions on*, 60(5):1354–1365, 2013.

[44] Hyeongjun Park, Jing Sun, Steven Pekarek, Philip Stone, Daniel Opila, Richard Meyer, Ilya Kolmanovsky, and Raymond DeCarlo. Real-time model predictive control for shipboard power management using the ipa-sqp approach. *Control Systems Technology, IEEE Transactions on*, 23(6):2129–2143, 2015.

[45] J. Armstrong, Craig Casey, Glen Creamer, and Gilbert Dutchover. Pointing control for low altitude triple CubeSat space darts. In *Proceedings of the 23nd AIAA/USU Conference on Small Satellites, Utah State University, Logan, UT*, pages Paper SSC09–X–4, 2009.

[46] WJ Ubbels, AR Bonnema, ED van Breukelen, JH Doorn, R van den Eikhoff, E Van der Linden, GT Aalbers, J Rotteveel, RJ Hamann, and CJM Verhoeven. Delfi-C3: a student nanosatellite as a test-bed for thin film solar cells and wireless onboard communication. In *Recent Advances in Space Technologies, 2005. RAST 2005. Proceedings of 2nd International Conference on*, pages 167–172. IEEE, 2005.

[47] J Bouwmeester, GF Brouwer, EKA Gill, GLE Monna, and J Rotteveel. Design status of the Delfi-Next nanosatellite project. In *Proceedings of the 61th international astronautical congress, Prague*, 2010.

[48] James Cutler, Aaron Ridley, and Andrew Nicholas. CubeSat investigating atmospheric density response to extreme driving (CADRE). In *Proceedings of the 25th AIAA/USU Conference on Small Satellites, Utah State University, Logan, UT*, pages Paper SSC11–IV–7, 2011.

[49] Pablo A Anigstein and Ricardo S Sanchez Pena. Analysis of solar panel orientation in low altitude satellites. *Aerospace and Electronic Systems, IEEE Transactions on*, 34(2):569–578, 1998.

[50] E. M. Gaddy. Computing the projected area of a spacecraft solar array with matrices. *In Proceedings of the 18th Intersociety Energy Conversion Engineering Conference, 1983*.

[51] J.C. Springmann and Cutler J.W. Optimization of directional sensor orientation with application to photodiodes for spacecraft attitude determination. *Proceedings of the 23rd AAS/AIAA Spaceflight Mechanics Meeting, Kauai, Hawaii, February 2013*.

[52] Dave Shreiner and Bill The Group. *OpenGL Programming Guide*. Addison-Wesley Professional, August 2009.

[53] Muhammad Iqbal. *An introduction to solar radiation*. Elsevier, 1983.

[54] David M. Gates. Spectral distribution of solar radiation at the earth's surface. *Science*, 151(3710):523–529, 1966.

[55] WW Hough and BD Elrod. Solar array performance as a function of orbital parameters and spacecraft attitude. *Journal of Manufacturing Science and Engineering*, 91(1):13–20, 1969.

[56] David W. Zingg, Marian Nemec, and Thomas H. Pulliam. A comparative evaluation of genetic and gradient-based algorithms applied to aerodynamic optimization. *European Journal of Computational Mechanics*, 17(1-2):103–126, 2008.

[57] Joaquim RRA Martins and Andrew B Lambe. Multidisciplinary design optimization: a survey of architectures. *AIAA journal*, 51(9):2049–2075, 2013.

[58] Andrew Klesh and James Cutler. Exploiting the link: Improving satellite communication through higher elevation links. In *AIAA/AAS Astrodynamics Specialist Conference*, 2010.

[59] Jens Gießelmann. Development of an active magnetic attitude determination and control system for picosatellites on highly inclined circular low earth orbits. 2006.

[60] Hajime Kawamura, Kazuhito Naka, Norihiro Yonekura, Sanshiro Yamanaka, Hideaki Kawamura, Hideyuki Ohno, and Katsuhiko Naito. Simulation of i–v characteristics of a pv module with shaded pv cells. *Solar Energy Materials and Solar Cells*, 75(3):613–621, 2003.

[61] Ruben E Perez, Peter W Jansen, and Joaquim RRA Martins. pyopt: a python-based object-oriented framework for nonlinear constrained optimization. *Structural and Multidisciplinary Optimization*, 45(1):101–118, 2012.

[62] Philip E Gill, Walter Murray, and Michael A Saunders. Snopt: An sqp algorithm for large-scale constrained optimization. *SIAM review*, 47(1):99–131, 2005.

[63] G Kreisselmeier. Systematic control design by optimizing a vector performance index. In *IFAC Symp. Computer Aided Design of Control Systems, Zurich, Switzerland, 1979*, 1979.

[64] Nicholas MK Poon and Joaquim RRA Martins. An adaptive approach to constraint aggregation using adjoint sensitivity analysis. *Structural and Multidisciplinary Optimization*, 34(1):61–73, 2007.

[65] Gaetan KW Kenway and Joaquim RRA Martins. Multipoint high-fidelity aerostructural optimization of a transport aircraft configuration. *Journal of Aircraft*, 51(1):144–160, 2014.

[66] Graeme J Kennedy and JRRA Martins. A comparison of metallic and composite aircraft wings using aerostructural design optimization. In *14th AIAA/ISSMO multidisciplinary analysis and optimization conference, Indianapolis, IN*, 2012.

[67] D.Q. Mayne, J.B. Rawlings, C.V. Rao, and P.O.M. Scokaert. Constrained model predictive control: Stability and optimality. *Automatica*, 36(6):789 – 814, 2000.

[68] Øyvind Hegrenæs, Jan Tommy Gravdahl, and Petter Tøndel. Spacecraft attitude control using explicit model predictive control. *Automatica*, 41(12):2107–2114, 2005.

[69] Enrico Silani and Marco Lovera. Magnetic spacecraft attitude control: a survey and some new results. *Control Engineering Practice*, 13(3):357–371, 2005.

[70] Jeroen Vandersteen, Moritz Diehl, Conny Aerts, and Jan Swevers. Spacecraft attitude estimation and sensor calibration using moving horizon estimation. *Journal of Guidance, Control, and Dynamics*, 36(3):734–742, 2013.

[71] A. Guiggiani, I. Kolmanovsky, P. Patrinos, and A. Bemporad. Fixed-point constrained model predictive control of spacecraft attitude. In *Proceedings of 2015 American Control Conference*, pages 2317–2322, Chicago, IL, July 2015.

[72] A. Guiggiani, Ilya V. Kolmanovsky, P. Patrinos, and A. Bemporad. Constrained model predictive control of spacecraft attitude with reaction wheels desaturation. In *Proceedings of 2015 European Control Conference*, pages 1376–1381, Linz, Austria, 2015.

[73] Bong Wie and Jianbo Lu. Feedback control logic for spacecraft eigenaxis rotations under slew rate and control constraints. *Journal of Guidance, Control, and Dynamics*, 18(6):1372–1379, 1995.

[74] Hyochoong Bang, Min-Jea Tahk, and Hyung-Don Choi. Large angle attitude control of spacecraft with actuator saturation. *Control Engineering Practice*, 11(9):989 – 997, 2003.

[75] Imran Ali, Gianmarco Radice, and Jongrae Kim. Backstepping control design with actuator torque bound for spacecraft attitude maneuver. *Journal of guidance, control, and dynamics*, 33(1):254–259, 2010.

[76] Dov Verbin and Vaios J. Lappas. Rapid rotational maneuvering of rigid satellites with reaction wheels. *Journal of Guidance, Control, and Dynamics*, 36(5):1538–1544, 2013.

[77] Colin R McInnes. Large angle slew maneuvers with autonomous sun vector avoidance. *Journal of guidance, control, and dynamics*, 17(4):875–877, 1994.

[78] Hari B Hablani. Attitude commands avoiding bright objects and maintaining communication with ground station. *Journal of Guidance, Control, and Dynamics*, 22(6):759–767, 1999.

[79] Yoonsoo Kim and M. Mesbahi. Quadratically constrained attitude control via semidefinite programming. *Automatic Control, IEEE Transactions on*, 49(5):731–735, May 2004.

[80] J.D. Koenig. A novel attitude guidance algorithm for exclusion zone avoidance. In *Aerospace conference, 2009 IEEE*, pages 1–10, March 2009.

[81] Cui Hutao, Cheng Xiaojun, Xu Rui, and Cui Pingyuan. RHC-based attitude control of spacecraft under geometric constraints. *Aircraft Engineering and Aerospace Technology*, 83(5):296–305, 2011.

[82] Henri C. Kjellberg and E Glenn Lightsey. Discretized constrained attitude pathfinding and control for satellites. *Journal of Guidance, Control, and Dynamics*, 36(5):1301–1309, 2013.

[83] Uros Kalabic, Rajesh Gupta, Stefano Di Cairano, Anthony Bloch, and Ilya Kolmanovsky. Constrained spacecraft attitude control on SO(3) using reference governors and nonlinear model predictive control. In *Proceedings of 2014 American Control Conference*, pages 5586–5593, Portland, OR, June 2014.

[84] Rohit Gupta, U. V. Kalabić, S. Di Cairano, A. M. Bloch, and I. V. Kolmanovsky. Constrained spacecraft attitude control on SO(3) using fast nonlinear model predictive control. In *Proceedings of 2015 American Control Conference*, pages 2980–2986, Chicago, IL, July 2015.

[85] Taeyoung Lee, Melvin Leok, and N Harris McClamroch. Optimal attitude control of a rigid body using geometrically exact computations on SO(3). *Journal of Dynamical and Control Systems*, 14(4):465–487, 2008.

[86] Dae Young Lee, Rohit Gupta, Uros V. Kalabić, Stefano Di Cairano, Anthony M. Bloch, James W. Cutler, and Ilya V. Kolmanovsky. Constrained attitude maneuvering of a spacecraft with reaction wheel assembly by nonlinear model predictive control. In *submitted to 2016 American Control Conference*.

[87] Taeyoung Lee. *Computational geometric mechanics and control of rigid bodies*. PhD thesis, University of Michigan, 2008.

[88] Taeyoung Lee and Frederick Leve. Lagrangian mechanics and lie group variational integrators for spacecraft with imbalanced reaction wheels. In *Proceedings of 2014 American Control Conference*, pages 3122–3127, Portland, OR, June 2014.

[89] Uroš Kalabić, Rohit Gupta, Stefano Di Cairano, Anthony Bloch, and Ilya Kolmanovsky. MPC on manifolds with applications to the control of systems on matrix lie groups. *arXiv preprint arXiv:1509.08567*, 2015.

[90] Jeff Foust, David Vaccaro, Chad Frappier, and Dustin Kaiser. If you build it, who will come? identifying markets for low-cost small satellites. In *Proceedings of the 22nd AIAA/USU Conference on Small Satellites, Utah State University, Logan, UT*, pages Paper SSC08–I–1, 2008.

[91] Hyeongjun Park. *Real-time Predictive Control of Constrained Nonlinear Systems Using the IPA-SQP Approach*. PhD thesis, The University of Michigan, 2014.

[92] Darryl D Holm, Tanya Schmah, Cristina Stoica, and David CP Ellis. *Geometric mechanics and symmetry: from finite to infinite dimensions*. Oxford University Press London, 2009.